



SCUOLA INTERNAZIONALE SUPERIORE DI STUDI AVANZATI
INTERNATIONAL SCHOOL FOR ADVANCED STUDIES

MECHANICAL RESONATING DEVICES AND THEIR APPLICATIONS IN BIOMOLECULAR STUDIES

Thesis submitted for the degree of Doctor Philosophiae

Candidate:

Mauro Melli

Supervisors:

Prof. Giacinto Scoles

Dr. Marco Lazzarino

October 2010

a Francesca

Abstract and Synoptic of the Thesis

The field of biology experienced a new renaissance in this new millennium thanks to the innovative techniques of imaging analysis and manipulation that nanotechnology developed in the last decade. The healthcare also benefits of this recent technological revolution, and it is only the beginning of a new era in this field. One technology which played a considerable role in this sense is microfabrication which nowadays has a huge number of applications in life science. Micro/nano electromechanical systems (NEMS/MEMS) in particular found application in several fields of biology. The work presented in this thesis belongs to this thread and covers two main subjects, the development of a novel class of mechanical resonator, tapered pillars, as very sensitive mass sensor and a new approach for chemical functionalization of atomically flat cantilever surface. All the experimental activity was carried out at the TASC-IOM laboratory in Trieste.

In the first project, I was involved in all single steps of the experiment. I designed and fabricated the devices and the experimental setup. I focused on the DNA self assembled monolayer characterization. In particular, the kinetics of film formations and the hybridization efficiency was studied.

The second project has been developed in collaboration with Valeria Toffoli and Dott. Emanuela Carleschi. My contribution regarded mainly the fabrication of the devices. We demonstrated that cleaving silicon microstructures in a proper reactive ambient results in a spatially controlled functionalization with strong covalent bond, through a carbon-silicon cycloaddition process. This approach, together with a suitable design of the sacrificial silicon structures, provides the possibility to chemically functionalize the active areas of a device with unmatched precision.

Overview of the Thesis

To introduce the reader in the subjects of the thesis, Chapter 1 provides an overview on the different aspects of the mechanical sensors. After a brief introduction to NEMS/MEMS, the different approaches of mechanical sensing are provided and the main actuation and detection schemes are described. The chapter ends with an introduction to microfabrication.

Chapter 2 deals with experimental details. In first paragraph the advantages of using a pillar instead of common horizontal cantilever are illustrated. Then, the fabrication procedures and the experimental setup for resonance frequencies measurement are described. The concluding paragraph illustrates the technique, known as dip and dry, I used for coupling mechanical detection with biological problems.

In Chapter 3, DNA kinetics of adsorption and hybridization efficiency, measured by means of pillar approach, are reported.

Chapter 4 gives an overview of the preliminary results of two novel applications of pillar approach. They are the development of a protein chip technology based on pillars and the second is the combination of pillars and nanografting, an AFM based nanolithography.

Chapter 5 starts with an introduction about the twin cantilever approach and of the mechanically induced functionalization. Fabrication procedure is described in the second paragraph. Then the chemical functionalizations are described and proved. Cleaved surface analyses and the spectroscopic studies of the mechanically induced functionalization are reported.

In Appendix A there is an overview of the physical models that are used in this thesis.

Table of Contents

Abstract and Synoptic of the Thesis	3
Overview of the Thesis	4
Micromechanical Resonators	7
1.1 Introduction.....	7
1.2 BioMEMS	10
1.3 Mechanical Sensors.....	12
1.3.1 Static Mode	13
1.3.2 Dynamic Mode	14
1.3.3 Resonance Frequency PLL Mode.....	17
1.4 Detection and Actuation	19
Optical Lever.....	20
1.5 Microfabrication.....	22
1.6 References.....	26
Experimental Details and Pillar Approach	31
2.1 Introduction.....	31
2.2 Fabrication.....	33
Bosch™ process	36
2.3 Experimental Setup	38
2.3.1 Vacuum.....	38
2.3.2 Optical Setup	40
2.3.3 The Mechanical Mounting	42
2.3.4 The Photodetector and the Acquisition System	43
Why a lorentzian?.....	44
2.4 Pillar Characterization	46
2.5 Laser and Water Influence	49
2.6 The “dip and dry” Method	52
2.7 Reference	56
Quantitative Study of Nucleic Acid Monolayers by Means of Pillar-Based Mass Sensors	59

3.1 Introduction.....	59
3.2 Material and Methods.....	60
3.3 Results	62
3.4 Discussion	64
3.5 Pillars as DNA Sensors	70
3.6 References.....	71
Future Developments.....	73
4.1 Application of Pillar Oscillators to Protein Nanoarray Development	73
4.1.1 Materials.....	75
4.1.2 Results	76
4.2 Nanografting.....	76
4.3 References.....	81
Chemical Functionalization of Atomically Flat Cantilever Surface.....	83
5.1 Introduction.....	83
5.2 Fabrication Procedure and Gap Tuning.....	84
5.3 Chemical Functionalization	85
5.4 Cleaved Surface Analysis	90
5.5 Spectroscopic Studies of the Mechanical Induced Functionalization.....	93
5.6 References.....	98
Conclusions	101
Acknowledgment	103
Appendix A	105
Elasticity.....	105
The Bent Beam	107

Micromechanical Resonators

1.1 Introduction

The invention of the field effect transistor in 1947 gave birth 15 years later to the beginning of integrated circuit (IC) technology which is the fabrication of complex electronic circuits on a small piece of a semiconductor [1]. It was immediately clear to that this technology would be a revolution so a big effort has been made in order to shrink the dimensions and to increase the quality of all microstructures.

Since the fifties, physicists, chemists and engineers joined forces, because of the necessity of a broad interdisciplinary approach, and many materials, processes and tools have been invented and studied in depth. Nowadays, it is possible to realize chips with an area of around 350 mm^2 and with almost 1 million of transistors per mm^2 . This allowed shrinking computers which had dimensions of a room in devices which can be kept in one hand. Indeed, “shrink” is the keyword of the electronics industry because smaller means cheaper and faster because less material, power and space are required.

In almost forty years, the minimum printed line width (i.e., transistor gate length) was reduced from 10 microns (1971) to 32 nanometers (2010). Furthermore, the International Technology Roadmap for Semiconductors (ITRS) estimates that the 11 nanometer mark will be reached in 2022 [2]. This will represent the ultimate step of the miniaturization of silicon devices: smaller than that will be forbidden by the laws of quantum mechanics.

However, all the know-how, accumulated over the decades, was not confined only to the electronics industry but several and different applications have been proposed. In the 1970s, the concept of micro-electro-mechanical systems (MEMS) was introduced and now this technology is used in many devices, from inkjets printers to automotive, and has reached an important role in the market [3]. MEMS is the integration of mechanical elements and electronics on a common substrate through the utilization of microfabrication technology. The mechanical part, which can move, has two main functions sensing and actuating. For example, MEMS are used as

accelerometers, gyroscopes, and pressure or flow sensors and, as actuator, they are used as micromotors, mirror mounts or micro pumps.

The reasons of their success are basically three:

1. They are cheap. Due to the “batch processing” many devices are made in same time reducing the price of a single component.
2. They are extremely sensitive. In fact, as rule of thumb, in many applications, the smaller the sensor, the least is affected by external perturbations. Moreover as actuator, precision down to the nanometer scale is achievable.
3. They are small. Therefore it is possible to integrate many sensors.

Besides these commercially available applications which we use every day, MEMS has attracted the interest of some researchers in the field of fundamental research.

Due to a constant effort to shrink the devices and to improve measurement techniques, force and mass sensitivity of the order of zeptonewtons and zeptogram (zepto = 10^{-21}) have been demonstrated. In general, when devices are fabricated below the 100 nm scale they are called nano electro- mechanical systems (NEMS). Usually, however, just one of three dimensions (i.e. thickness) is less than 100 nanometers. Now, thanks to NEMS it is possible to explore some of the fundamental laws of Physics. Currently, one of the most important goals is to observe the quantum fluctuations of a mechanical system, due to zero point energy. In fig. 1 some of the most important results are shown [4-9].

This kind of measurement, requires extremely demanding condition, like MilliKelvin temperature and ultra high vacuum, so with the present technology, they are confined in few high level laboratories and can hardly be applied in any commercial application. But if we accept the compromise of reducing the sensitivity in favor of increasing the feasibility we can still use the MEMS approach for developing tools and applications for different fields of science, including Biology and Medicine.

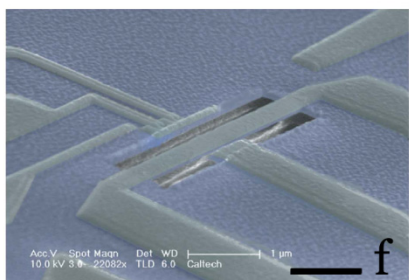
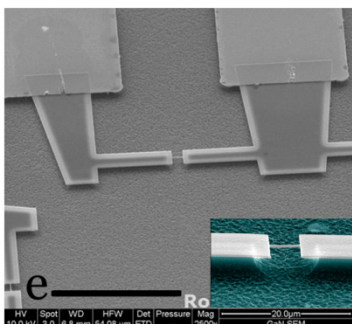
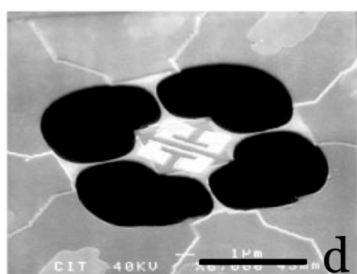
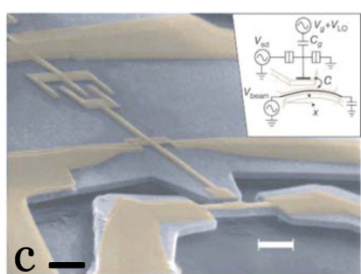
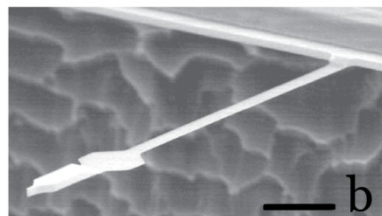
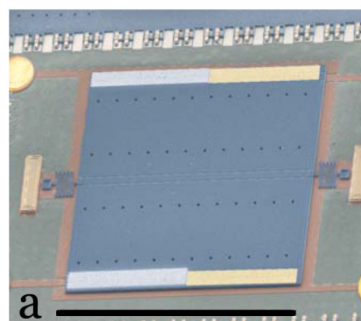


Figure 1. NEMS device.

- (a) A torsional resonator used to study Casimir forces (scale bar 500 μm [4]).
- (b) An ultrasensitive magnetic force detector that has been used to detect a single electron spin (scale bar 10 μm [5]).
- (c) A 116-Mhz resonator coupled to a single-electron transistor (scale bar 1 μm [6]).
- (d) Suspended mesoscopic device used for measuring the quantum of thermal conductance (scale bar 5 μm [7]).
- (e) Zeptogram-Scale Nanomechanical Mass sensor (scale bar 20 μm [8]).
- (f) Nanomechanical resonator coupled to qubits (scale bar 1 μm [9]).

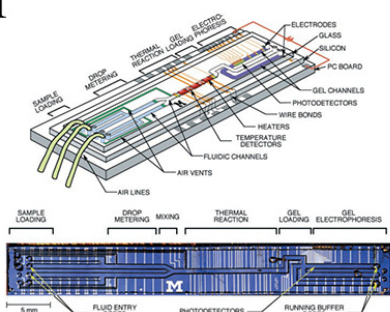
1.2 BioMEMS

The term BioMEMS was introduced to specify a class of MEMS used for biological application but nowadays it has a more broad and general meaning. R. Bashir in his review about BioMEMS [10] gives the definition *“devices or systems, constructed using techniques inspired from micro/nano-scale fabrication, that are used for processing, delivery, manipulation, analysis, or construction of biological and chemical entities”*. According to this classification, for example, also force microscopy based on atomic force microscopy or microfluidics devices can be categorized as “BioMEMS”. Surely, this definition can appear strange, because it includes devices which do not possess any mechanical component or do not integrate directly an electrical part but after all it is just a semantic question. In Figure 2 some examples of microfluidic and non-mechanical BioMEMS are shown [11-16].

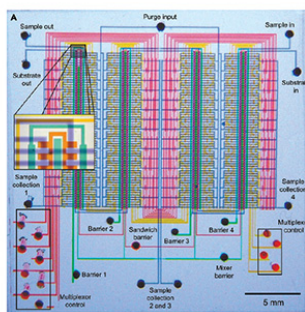
Figure 2. BioMEMS.

- (1) An Integrated Nanoliter DNA Analysis Device which has fluidic channels, heaters, temperature sensors, and fluorescence detectors to analyze nanoliter-size DNA samples. [11]
- (2) Optical micrograph of a high-density microfluidic chip that contains plumbing networks with thousands of micromechanical valves and hundreds of individually addressable chambers. The various inputs have been loaded with food dyes to visualize the channels and subelements of the fluidic logic. [12]
- (3) Zero-Mode Waveguides for Single-Molecule Analysis. (A) The coverslip, with overlying gasket to isolate arrays for individual experiments. Successive increases in scale are shown in (B) to (D). A scanning electron microscope image of an individual waveguide is shown in (D). (F) An apparatus for single-molecule enzymology using zeromode waveguides. [13]
- (4) The microtoroid resonator biological sensor. The interaction of the whispering-gallery mode with the environment, specifically molecules bound on the surface of the toroid, enables the ultrasensitive detection. [14]
- (5) Microelectrode arrays (MEAs) are arrangements of usually 60 electrodes that are used for multisite extracellular recordings from electrogenic cells. The high-density CMOS-based microelectrode array features 11,011 metal electrodes and 126 channels, each of which comprises recording and stimulation electronics, for extracellular bidirectional communication with electrogenic cells. [15]
- (6) Images of microneedles used for transdermal drug delivery [16].

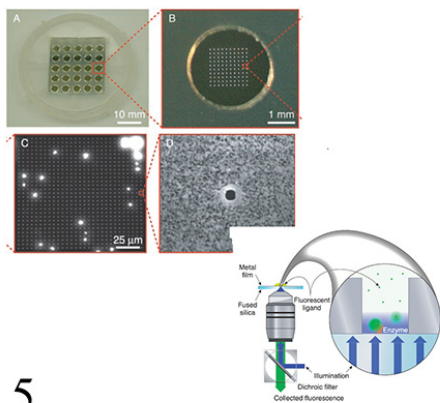
1



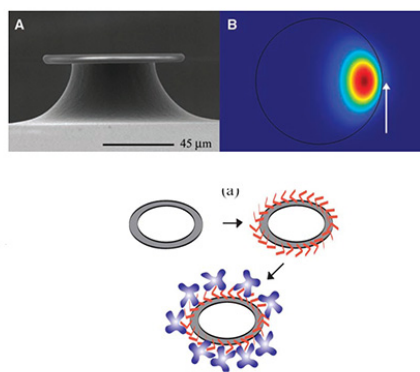
2



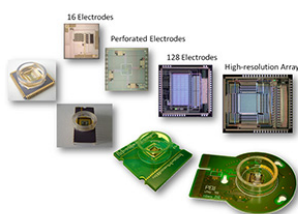
3



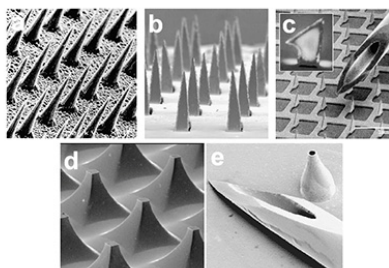
4



5



6



However in this introduction and in the rest of the thesis we will focus on device based on mechanical detection of chemical interactions like adsorption or chemical reactivity.

The main advances due to the use of MEMS are:

High sensitivity. In general, biological materials (DNA, protein) are present in a very low amount inside a single cell or even in the entire body. Standard biotechnological approach uses amplification of the material of interest using protocols like polymerase chain reaction (PCR). The

main drawback is that an exponential amplification may propagate errors. The alternative approach consists in avoiding duplication by means of highly sensitive MEMS.

Label Free. Most of the commonly used techniques to detect molecules are based on optical detection. This means that target molecules have to be functionalized with an optical active group (fluorescence). By using alternative detection scheme offered by MEMS is possible to avoid this step reducing the probability of artifacts and errors.

Parallelization. Biological systems are complex. For example, each single process is governed by many proteins or an illness can be due to mutation of several genes. Therefore in order to have a complete picture it is necessary always to measure many so called biomarkers. One of the characteristics of MEMS is the possibility to integrate many sensors on the same device. Each sensor can be assigned to a specific molecule. In this way, due to high parallelization, it is possible to perform simultaneously a complex analysis, reducing significantly the time required to analyze the entire process.

Integration. The idea of a lab-on-a-chip (LOC) is completely based on MEMS. LOC is a device that integrates many laboratory functions on a single chip of only millimeters to a few square centimeters in size. Sometimes the term "Micro Total Analysis Systems" (μ TAS) is used as well.

Real time. The direct integration with electronics and microfluidic systems allows designing sensors which provide the results in a real time or in a very short time. From a clinical point of view, for instance, the speed, together with accuracy, is an essential characteristic for any good diagnostic tool.

1.3 Mechanical Sensors

The Atomic Force Microscope (AFM) was invented in 1986 as tool for imagining surfaces [17]. It is a complex instrument but the sensing element is simple and completely mechanical. In fact, it is just a cantilever which bends because of interactions with the substrate. In the last few years non-imaging applications were developed and the AFM was used for studying the inter- and intra-molecular interactions down to the single molecule level [18]. This became possible because force

spectroscopy based on these new experimental tools allows measuring force in the piconewton range on the ms time scale. The AFM force spectroscopy (i.e. a cantilever with a tip) is still a growing field but researchers have also begun to develop cantilever-only mechanical sensors. A cantilever is only one of the possible geometries of a mechanical molecular sensor, an oscillating bridge being another, but, because of the many applications, in this chapter the former will be considered as a benchmark model.

The adsorption of molecules on a cantilever sensor has two main effects: increasing the mass and changing the surface stress. There are three approaches to measuring which divide the MEMS mechanical sensors in as many categories:

1. Static mode: the static deflection due to the differential surface stress between the upper and lower sides of the cantilever is measured.
2. Dynamic mode: the response to an external periodical force in a frequency range around the resonance frequency is measured. It gives information about the resonance frequency and the shape of the resonance curve.
3. Resonance Frequency Phase Lock Loop (PLL) mode: the cantilever is kept at its resonant frequency by means of a Phase Lock Loop. The measured output in this case is the shift in frequency.

1.3.1 Static Mode

A generic beam which experiences a different surface stress on two opposite sides bends itself and the deflection δ is proportional to the differential stress $\Delta\sigma$ according to the Stoney's equation [19], [20]:

$$\delta = \frac{3(1 - \nu)}{E} \left(\frac{L}{t}\right)^2 \Delta\sigma$$

where ν is Poisson's ratio, E is Young's modulus, L is the beam length and t is the cantilever thickness. This model is valid also for micro cantilevers and by means of selective functionalization

of one side of the cantilever it possible to transduce molecular adsorption into mechanical bending. The selective functionalization is often obtained by exploiting the gold-thiol interaction. Probe molecules are functionalized with a thiol group and one side of the cantilever is coated with gold.

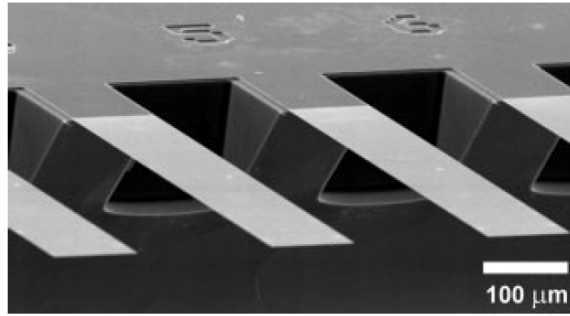
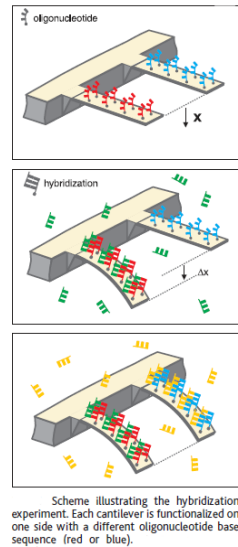


Fig.3. Scanning electron micrograph of a section of a microfabricated silicon cantilever array (eight cantilevers, each $1\ \mu\text{m}$ thick, $500\ \mu\text{m}$ long, and $100\ \mu\text{m}$ wide, with a pitch of $250\ \mu\text{m}$, spring constant $0.02\ \text{N m}^{-1}$; Micro- and Nanomechanics Group, IBM Zurich Research Laboratory, Switzerland). (From [21])



Thiolated molecules covalently bind with the gold substrate. Subsequently the target molecules bind to the probe molecules. Each step in this sequence induces a certain amount of bending.

Arrays of cantilevers allow performing differential measurements to recognize different molecules. In 2000, Gerber and his collaborators published a milestone paper about the application of this technique for biomolecular recognition (see Fig. 3 [21]). They reported that a single base mismatch between two 12-mer oligonucleotides was clearly detectable. Detection of proteins and cancer markers such prostate specific antigens, which were detected at $0.2\ \text{ng/ml}$ in a human serum background of was also reported. The static mode has the big advantage to be completely compatible with a liquid environment but in order to achieve a measurable deflection an almost complete functionalization of one of the two surfaces is required. As consequence, the main drawbacks are the low sensitivity and slow response.

1.3.2 Dynamic Mode

A mechanical physical system responds to an external oscillating force with different amplitudes as a function of the frequency. The spectral distribution is characterized by peaks which are known as resonant frequencies which correspond to oscillating modes. A small driving force at resonance can induce a large oscillation. In appendix A, where more details of the mathematical description will be given, it is shown that a load at the end of a cantilever induces a deflection which is linearly

proportional to the force applied. Therefore, it is natural to introduce a lumped element model to

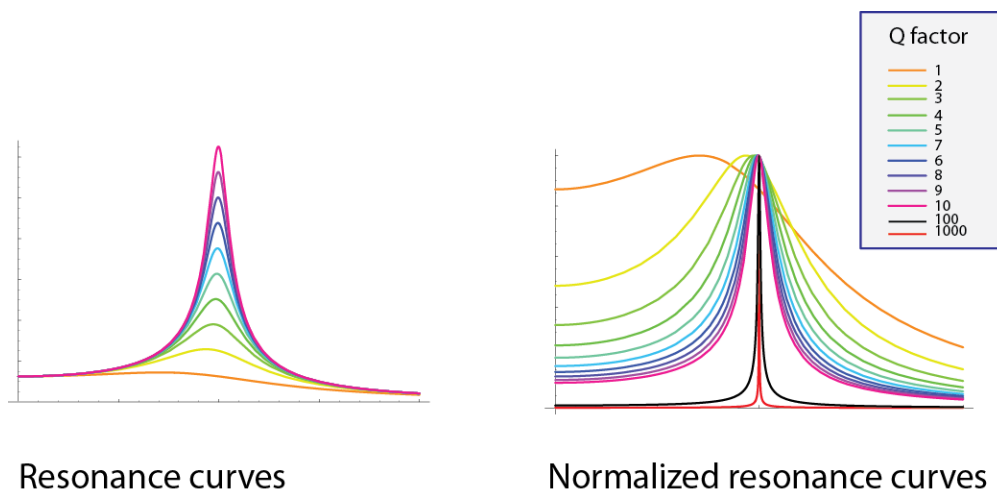


Figure 4. Influence of the Q factor on the shape of resonance curves.

describe the dynamics of a cantilever. The cantilever is approximated a mass linked to a spring (characterized by the spring constant k) which moves in a viscous medium. In order to describe all the geometrical effect due to a tridimensional structure, the actual values of the mass is substituted by a reduced mass value. Each mode has different geometrical factors. A resonance curve is characterized by two parameters: the position of the peak (resonance frequency) and the width of the peak which is generally calculated at the half maximum and indicated with FWHM (Full Width at Half Maximum). More often, a dimensionless parameter, the quality factor or Q factor is used. It is defined as the ratio between the resonance frequency and the FWHM. Typical ranges are shown in Table 1. The Q factor has also a physical interpretation being proportional to the ratio between the energy stored to the energy being lost in one cycle.

Q factor Range	
Vacuum	5000 - 100000
Air	10 - 500
Liquid	< 5

There are many sources of energy loss but the most critical is the damping by the medium where the resonator oscillates. In Figure 4, some curves of resonance with different Q factor are shown.

In appendix A, we will show that if the damping is negligible, the peak position of the lowest mode corresponds to the natural frequency and is given by:

$$f_0 = \frac{1}{2\pi} \sqrt{\frac{k}{m^*}} = \frac{1}{2\pi} \sqrt{\frac{E}{\rho} \frac{t}{L^2}}$$

where ρ is the density. If the damping is not negligible the peak it is not at the natural frequency but is reduced by the factor $\sqrt{1 - \frac{1}{2Q^2}}$ (For Q factor of 10 the reduction is 0.25%, for Q factor of 1000 is 0.25 ppm).

The adsorption of molecules changes the shape of the resonance curves. The main effect is to shift the resonance frequency. As first approximation, the mass of the resonator increases by the quantity Δm which corresponds to the mass of adsorbed molecules. According to the harmonic oscillator equation the resonance changes to the value:

$$f_{\Delta m} = \frac{1}{2\pi} \sqrt{\frac{k}{m^* + \Delta m}}$$

Assuming the elastic constant does not change. If the added mass is much smaller than the mass of the resonator it is possible obtain a linear relation between the shift in frequency and the variation of mass:

$$\frac{\Delta f}{f_0} = -\frac{1}{2} \frac{\Delta m}{m^0}$$

In the Chapter 2 the limits of this model will be shown. Alternatively, it is possible to focus on the change of other parameters like the change of the device compliance or the Q factor. This technique is extremely sensitive in vacuum (attogram resolution) but has the big disadvantage that in a liquid environment loses its power. Due to viscous effect the width the resonance increases and the amplitude decreases dramatically. The main consequence is that minimum detectable frequency shift becomes very large and this approach becomes useless. For biological application this is a huge limitation but one possible solution is to separate the functionalization and adsorption phase from the measuring phase. This approach is commonly known as “dip and dry” [22], [23]. All the chemical reactions are performed in solution then the device is dried and placed in a vacuum chamber where the resonance frequency is measured. With this procedure, it is possible to preserve high sensitivity but becomes necessary to renounce to real time detection. In 2001, Ilic et al reported the detection of a single *Escherichia coli* cell (665 fg) by means of a silicon nitride cantilever with a sensitivity of 7.1 Hz/fg [24]. After three years, the adsorption of a single *vaccinia* virus (9.5 fg) was measured by Gupta et al. [25]. They used a silicon cantilever with

a sensitivity of 6.3 Hz/ag. In 2005, Ilic et al, was able to enumerate single dsDNA molecules (999 KDa = 1.6 ag) bound to a nanomechanical oscillator with a sensitivity of (194 Hz/ag) [26].

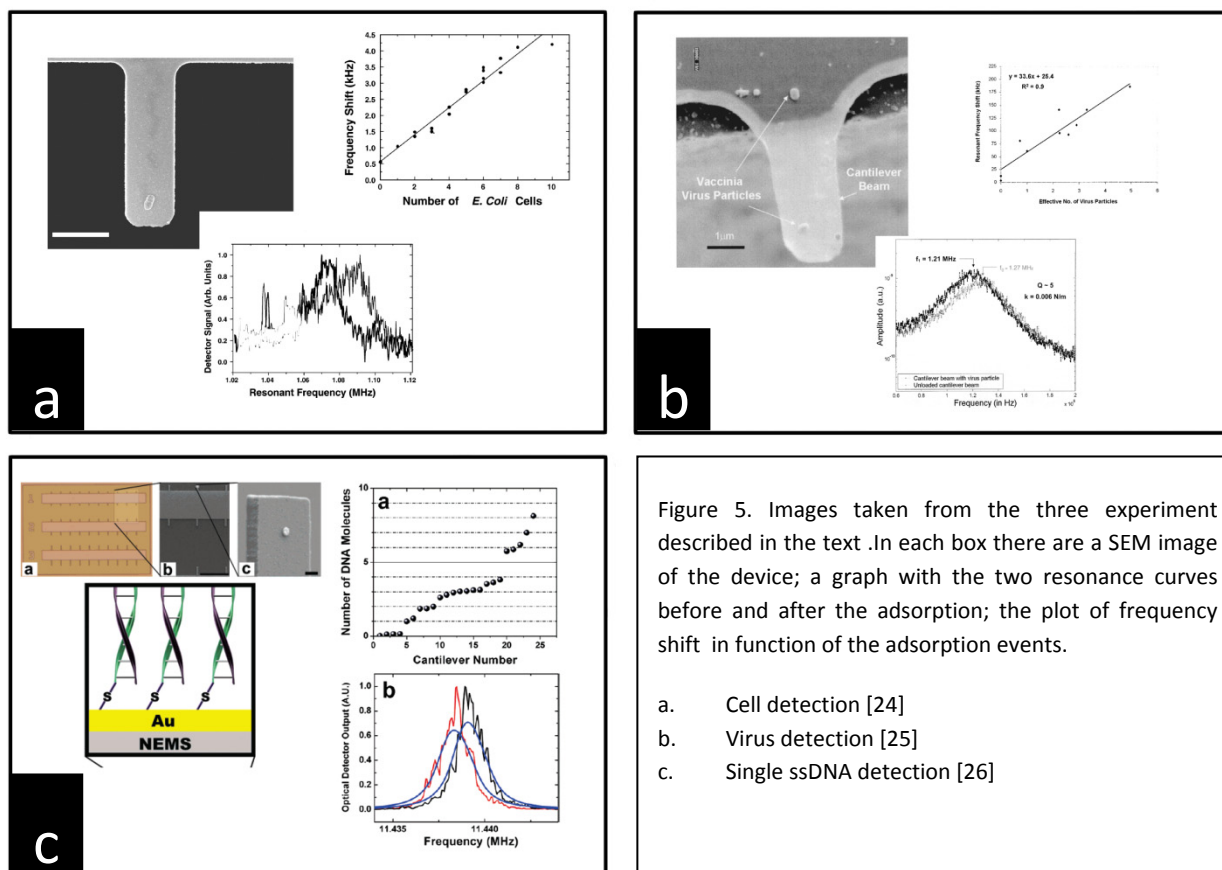


Figure 5. Images taken from the three experiment described in the text .In each box there are a SEM image of the device; a graph with the two resonance curves before and after the adsorption; the plot of frequency shift in function of the adsorption events.

- Cell detection [24]
- Virus detection [25]
- Single ssDNA detection [26]

1.3.3 Resonance Frequency PLL Mode

This mode is usually included in the dynamic mode because the cantilever is kept in oscillation but the difference is that this approach does not provide information about the spectral response but only about the shifts of the resonance peak. If an oscillator is actuated there is a phase difference φ between the actuation and the amplitude oscillation and it is function of the actuation frequency f :

$$\varphi = \tan^{-1} \frac{-f_0 f}{Q(f_0^2 - f^2)}$$

At the resonance, the phase difference φ is $-\pi/2$. As the name suggest, this detection mode is based on phase lock loop circuit [27]. The cantilever is actuated by an electronic signal at frequency f . The actuating signal is -90 degree shifted and continuously compared to the signal of the cantilever deflection. If f is set to be equal to f_0 the phase difference of the two signal is null. If the resonance frequency changes for any reason the phase difference (error signal) will be different of zero. The error

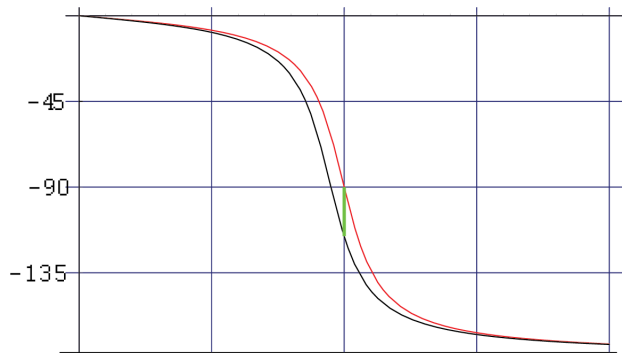


Figure 6. Two curves of phase shift in function of frequency with different resonance frequency.

signal controls the actuating signal and changes it in order to null itself like in a negative feedback system. This method, like any PLL control, can be implemented either with an analog circuit or with a digital (software) control. It is possible to track the variation of resonance frequency continuously and very quickly. This method has the big advantage to permit the performance of

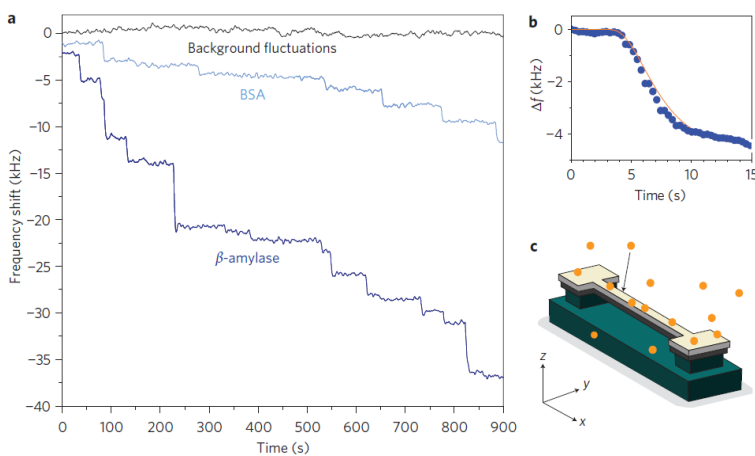


Figure 7. Real-time records of single-molecule adsorption events on a NEMS mass sensor. From [28].

nanoelectromechanical resonator [28].

real time and very fast measurements but has the drawback that it gives no information about the change of the device compliance or the Q factor. An example of this technique, applied not to a cantilever but to a bridge resonator, is given by the recent work of Naik et al. They recorded in real time the adsorption of individual protein onto a phase-locked, ultrahigh-frequency

1.4 Detection and Actuation

The potential of mechanical resonator sensors is strictly connected to the effectiveness of the actuation and the detection of the movements because the translation from a mechanical response to measurable signal will be, in this way, more accurate. Therefore a large effort has been made in order to explore and develop new detection schemes. They can be optical or electrical. The most widely used is the optical lever method [29]. Almost all commercial AFM are based on this technique. The working principle is based on deflection of a laser spot deflected at the focus on a cantilever. The angular deflection of the laser beam is twice that of the cantilever. The reflected laser beam strikes a position-sensitive photodetector consisting of two side-by-side photodiodes. The difference between the two photodiode signals indicates the position of the laser spot on the detector and thus the angular deflection of the cantilever. Because the cantilever-to-detector distance generally measures thousands of times the length of the cantilever, the optical lever greatly magnifies (~2000-fold) the motion of the tip. Photodiodes divided into two or four independent areas transduce the light into electrical signals that are amplified and elaborated to get the deflection of the beam. Optical lever detection is currently one of the most sensitive method for measuring deflection; vertical deflections as small as a few angstroms can be reliably measured with this technique. On the other hand the set up needs a laser source, some optics element (lens, mirrors), and a photodiode so it is somewhat delicate. The reduction of the cantilever size, which is required to obtain higher sensitivity, is limited by optical diffraction. Moreover it has low degree of parallelization, in fact, by means of multiple sources and detectors it is possible to monitor different cantilevers but due to cost and complexity issues the number of detectors has not been so far higher than ten.

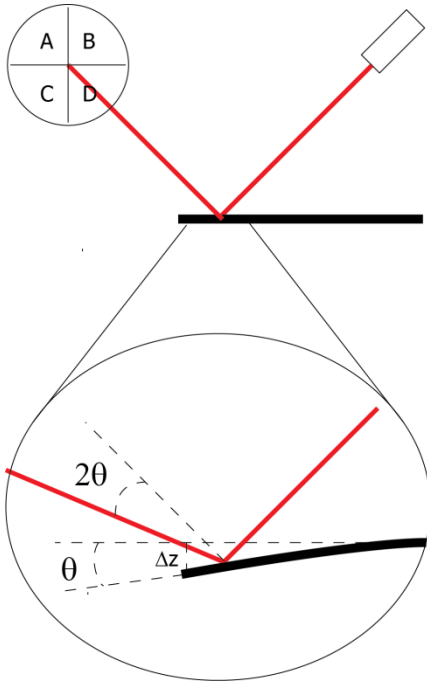


Figure 8. Scheme of the optical lever method.

Optical Lever

The standard elasticity theory gives the relation between the deflection of cantilever at the end Δz and the angle respect to null deflection:

$$\theta = \frac{3 \Delta z}{2 l}$$

The change of the normal of the reflecting surface of the cantilever will move the spot on the photodiode placed at distance S of a quantity (see Figure 8)

$$\Delta y = 2 \cdot \theta \cdot S = 3 \frac{S}{l} \Delta z \text{ (assuming } \theta \text{ small)}$$

At null deflection the photodiode is aligned in order to set the photocurrent in all quadrants of the photodiode the same. Deflecting the cantilever moves the position of the spot resulting in one photodiode collecting more light than the other one, producing an output signal (the difference between the photodiode signals normalized by their sum) which is proportional to the movement of the spot and to the deflection of the cantilever.

A second optical detection is based on interference. The cantilever is used as a moving mirror in a Michelson interferometer (see Figure 9) [30]. The movement of the cantilever causes a change in the optical path of one arm of the interferometer resulting in a change of intensity of the light at photodiode due to constructive or destructively interference. This method is extremely sensitive (deflection of the order 0.01 angstrom can be measured) and does not need an external height calibration. However it has the same practical limitation of the optical lever method. Also detection schemes based on Fabry-Perot scheme have been developed [31], [32].

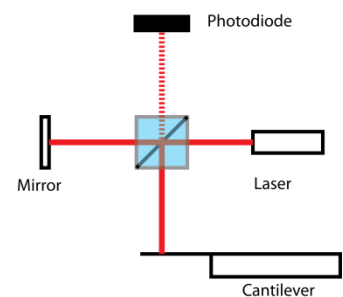


Figure 9. Schematic draw of the detection based on a Michelson interferometer scheme.

G. Nordin recently proposed an alternative optical detection (see Figure 10 [33]). He developed a photonic microcantilever with in plane photonic transduction of deflection. In his approach the microcantilever is etched to form a single mode rib waveguide. Light propagates down the microcantilever and crosses a small gap at the free end of the microcantilever, some of which is captured by an asymmetrical multimode waveguide that

terminates in a Y branch. The Y-branch outputs are used to form a differential signal that is monotonically dependent on microcantilever deflection.

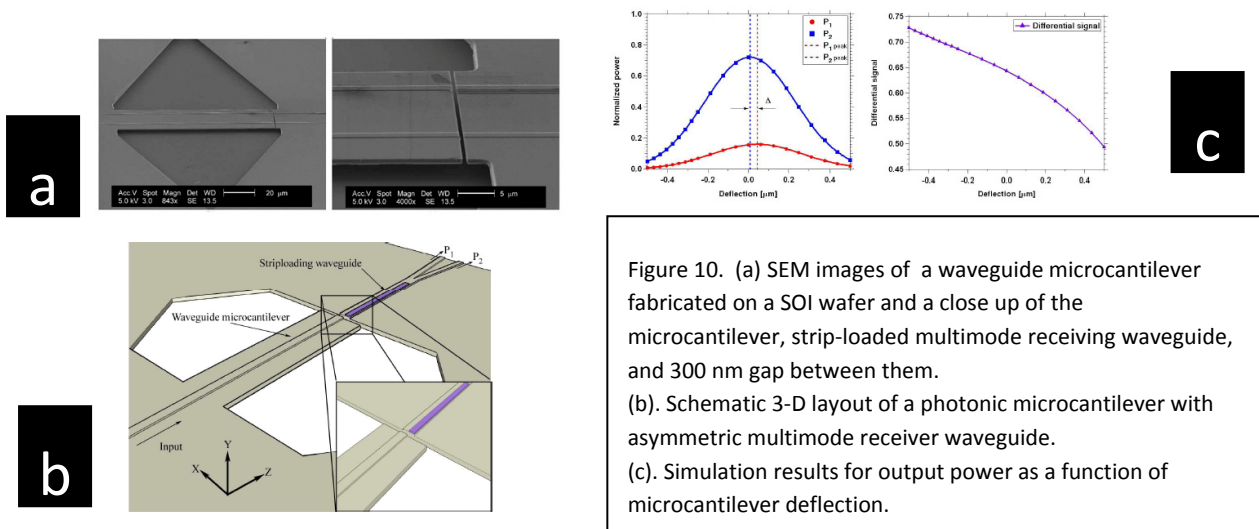


Figure 10. (a) SEM images of a waveguide microcantilever fabricated on a SOI wafer and a close up of the microcantilever, strip-loaded multimode receiving waveguide, and 300 nm gap between them. (b). Schematic 3-D layout of a photonic microcantilever with asymmetric multimode receiver waveguide. (c). Simulation results for output power as a function of microcantilever deflection.

Resonant sensors can also be placed inside an electrical circuit and acts as variable resistor or capacitor. The strain can change the electrical resistance of metals or semiconductors. In the case of metal the effect is totally geometric and it is described by Ohm's law. By contrast, in semiconductors the change of resistance is principally given by the change of the resistivity [34]. This effect is called piezoresistivity and it is due to the dependence of the bandgap on the inter-atomic spacing. By integrating a piezoresistive element onto a resonator or design a resonator in order to be a piezoresistive sensor it is possible to detect the bending by measuring the change of resistance [35]. This method is less sensitive than the optical ones and it is more affected by thermal fluctuations however it offers many advantages. There are no limitations to the size of the resonator, it possible to integrate with the read-out electronic on the same silicon chip and parallelization is only limited by wiring issue.

Even if there are many limitations a capacitive detection method is also used [36]. A cantilever and the substrate form a parallel plate capacitor if they are separated by insulating layer (Fig). The capacity is proportional to the surface of the cantilever and inversely proportional to the distance between the cantilever and the substrate. This implies some limitations on the geometry. The gap between the cantilever and the substrate must be the smallest possible in order to enhance the

sensitivity involving technical efforts from a fabrication point of view. Also the miniaturization is limited by sensitivity because the cantilever surface must be large enough to allow

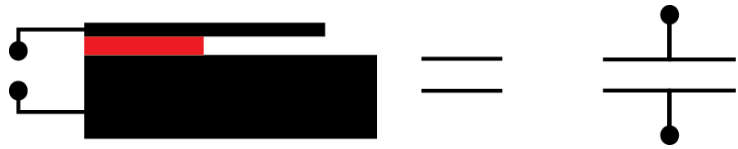


Figure 11. Cantilever as parallel plate capacitor.

a measurable variation of capacity. However the most crucial limitation is that this device is intrinsically a low pass filter (RC circuit) with frequency cut off inversely proportional to capacity. This makes this scheme not particularly suited for high frequency dynamic measures.

In all dynamical modes the resonators need to be actuated. In many applications, the thermal energy kT is enough to cause a measurable mechanical response but for highest sensitivity applications an external actuation is required to increase the signal to noise ratio. The most widely used technique, especially combined with optical detection, is to mount the chip with the resonator directly onto a piezoelectric crystal. In this method there is not any direct force acting on the cantilever but rather a mechanical coupling between the movement of the piezo and the modes of the cantilever. This technique is very simple to implement but is able to actuate at frequencies lower than few MHz due to intrinsic frequency cut off the piezo. The capacity detection method can be adapted to be an actuator [37]. In fact, by applying a bias V between the cantilever and the substrate an electrostatic force $F = \frac{\epsilon_0 V^2}{2d^2} S$ is generated. There are also other electrical methods based on electric displacement [38] or magnetomotive force [39]. They have less bandwidth limitation and allow accessing the GHz range [6]. The last actuation mechanism that is worth to mention is based on an optical-thermal mechanism [40]. A modulated laser illuminates one side and induces a local heating of the cantilever. The resulting temperature gradient induced an inhomogeneous thermal expansion causing a bending of the cantilever.

1.5 Microfabrication

Microfabrication is at the basis of the MEMS technology and is constituted by all the techniques which permit to fabricate structures with dimensions from microns to nanometers [41], [42]. Microfabrication takes place in a particular environment called “clean room” where particle

density, temperature and humidity are controlled. In fact, if dust particles, which have dimension comparable with microstructure, land on a micro fabricated device, they will ruin it. Moreover, in order to obtain robust and repeatable processes, temperature and humidity must have always the same value with very low fluctuations. The most studied and used material for fabrication is single crystalline silicon. Another common substrate in MEMS technology is silicon on insulator (SOI). It consists in a thick wafer of silicon covered by a thin thermal silicon oxide and of a thin crystalline layer of silicon which has the same crystallographic orientation of the substrate. It is widely used in MEMS because by removing the insulator layer (called in this context sacrificial layer) it is possible to make suspended structures. There are three fundamental processes: lithography, etching and film deposition. Figure 12 shows a typical process for the fabrication of a cantilever.

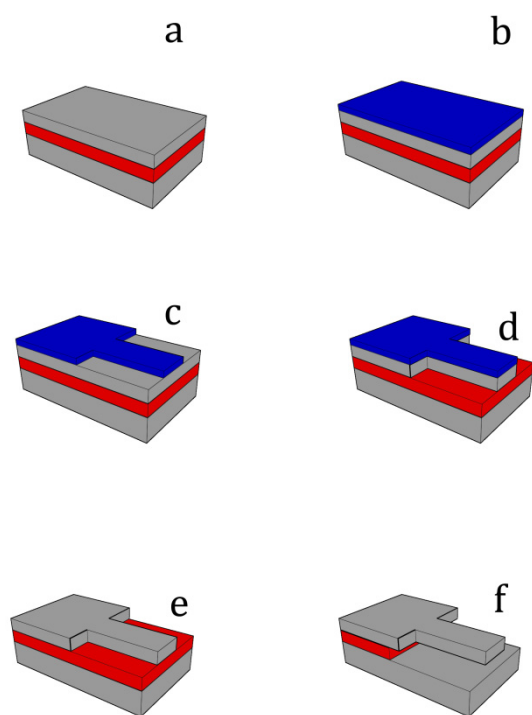


Figure 12. Steps for fabrication of a cantilever starting from a SOI wafer:

- a) SOI wafer
- b) Resist spin coating
- c) Lithography
- d) Etching
- e) Removing of resist
- f) Etching of the sacrificial layer

Optical Lithography is the process used to transfer a pattern from a mask to a substrate. First, the substrate must be coated with a thin layer of polymer (known as a resist) that is sensitive to ultraviolet radiation. Similarly to photography, an image is projected on the resist by making light to pass through a mask. The mask is a glass plate with transparent and opaque zones which draws the desired pattern. According to kind of resist, positive or negative, the illumination makes the polymer soluble or insoluble to a solution called developer. After the development the substrate is

coated with a patterned resist which protects locally the surface. Lithography requires the following steps:

1. cleaning of the substrate
2. resist deposition by spin coating
3. prebake for evaporating the resist solvent
4. illumination in a mask aligner. The mask aligner permits to align the mask with previous features or with crystallographic orientation of the substrate
5. postbake
6. development

The resolution of this patterning process is limited by the light diffraction at the mask edges and, as a rule of thumb, is given by the half the wavelength of the radiation used for the exposure. The main lines for mercury vapor lamp are 365.4 404.7 and 435.8 nm and maximum resolution is around 150 nm. Using X-rays it is possible to increase the resolution to 20 nm range but it is commonly used only in a synchrotron facility.

Alternatively, there is another kind of lithography based not on electromagnetic radiation but on electron beams. A scanning electron microscope allows focusing electrons on spots of the order of 2 nm on a substrate. The process is similar to photolithography but a different resist which is sensitive to electrons is used. Moreover there is no need of a mask because the pattern is created by moving the beam under control of computer using a pattern generator. The final resolution is limited by the properties of the resist and resolution down to 20 nm can be achieved but it is possible to push the resolution down to 10 nm. E-beam lithography offers higher resolution and greater flexibility respect to standard optical lithography but it is very slow and output is extremely low.

Etching is the second fundamental process and is the removing of material from the substrate. The patterned resist permits to control spatially the etching. There are two classes, wet etching and dry or plasma etching. The wet etching is a process where a wafer is put in solution where an active component removes material by making it soluble. For example two very important reactions are:

- $\text{SiO}_2 (\text{s}) + 6\text{HF} \rightarrow \text{H}_2\text{SiOF}_6 (\text{aq}) + 2\text{H}_2\text{O}$
- $\text{Si} (\text{s}) + 2\text{OH}^- + 2\text{H}_2\text{O} \rightarrow \text{Si}(\text{OH})_2(\text{O}^-)_2 (\text{aq}) + 2\text{H}_2 (\text{g})$

In plasma etching a wafer is placed in a vacuum chamber where plasma of a particular gas is created. In this case, the reaction with plasma makes the material volatile, for example:

- $\text{SiO}_2 (\text{s}) + \text{CF}_4 (\text{g}) \rightarrow \text{SiF}_4 (\text{g}) + \text{CO}_2 (\text{g})$

The plasma of a heavy gas, like Argon, can also be used to physically remove material by ion bombardment. This process, known as ion milling, is used specially with materials which are quite inert and so cannot be removed by chemical etching.

The etching is characterized by a parameter: etching rate; the speed of which a material is removed. It ranges from 1 nm/min to 1 micron/sec. It is not a constant but depends on many factors which characterize each process:

1. **Selectivity:** it is the ratio between the etching speeds of different material. For example, hydrofluoric acid removes silicon oxide one hundred times faster than silicon.
2. **Isotropy:** An etching can attack differently each crystallographic plane of a crystalline material. If the material is instead amorphous, the etching will be uniform causing a spherical profile. On the contrary, anisotropic etchings are characterized to be ineffective on some crystallographic planes causing profile with tilted flat walls. For example potassium hydroxide etches fast the silicon (100) plane but extremely slowly the (111) planes.
3. **Aspect ratio:** it is the ratio between the lowest dimension of the pattern and the height of the etching. This parameter is important especially in the anisotropic etchings where the target is to make vertical wall. In fact, a perfect anisotropy is impossible to achieve and there is always some undercut or overcut which limits the aspect ratio.

Film deposition. The opposite of etching is the deposition of material. There are several techniques: chemical vapor deposition (CVD with many variants), sputtering, thermal evaporation and electron beam evaporation. In CVD a heated wafer substrate reacts with a gaseous reactant in a vacuum chamber causing the growth of a thin layer of a desired material. CVD is usually used to grow silicon oxide or silicon nitride. Sputtering is a process where a solid target material is bombarded by energetic and heavy particles causing the sputtering of atoms of the target. The

bombarding particles are often supplied by argon plasma. Thermal and e-beam deposition are similar process where a target material is heated up to the evaporation temperature. The difference is in the heating. In thermal evaporation the target are warmed by standard heat source. In e-beam deposition an energetic and intense electronic beam is focused on a target.

Strictly connected with film deposition is the lift-off process which is the metallization after lithography and the removal of the resist. All metal evaporated on the resist is removed but the metal evaporated on the substrate stays and follows the pattern of the lithography as in sketched in Figure 13. However it is not a trivial process and much care must be take to avoid retention and re-deposition of the unwanted metal sheet.



Figure 13. Lift-off process.

1.6 References

- [1] B. Lojek, *History of Semiconductor Engineering*, 1° ed. Springer, 2006.
- [2] "www.itrs.net." [Online].
- [3] V. Kaajakari, *Practical MEMS: Design of microsystems, accelerometers, gyroscopes, RF MEMS, optical MEMS, and microfluidic systems*. Small Gear Publishing, 2009.
- [4] R. S. Decca, D. López, E. Fischbach, e D. E. Krause, "Measurement of the Casimir Force between Dissimilar Metals," *Physical Review Letters*, vol. 91, n°. 5, pag. 050402, Lug. 2003.
- [5] D. Rugar, R. Budakian, H. J. Mamin, e B. W. Chui, "Single spin detection by magnetic resonance force microscopy," *Nature*, vol. 430, n°. 6997, pagg. 329-332, Lug. 2004.
- [6] R. G. Knobel e A. N. Cleland, "Nanometre-scale displacement sensing using a single electron transistor," *Nature*, vol. 424, n°. 6946, pagg. 291-293, Lug. 2003.

- [7] K. Schwab, E. A. Henriksen, J. M. Worlock, e M. L. Roukes, "Measurement of the quantum of thermal conductance," *Nature*, vol. 404, n°. 6781, pagg. 974-977, Apr. 2000.
- [8] Y. T. Yang, C. Callegari, X. L. Feng, K. L. Ekinci, e M. L. Roukes, "Zeptogram-Scale Nanomechanical Mass Sensing," *Nano Letters*, vol. 6, n°. 4, pagg. 583-586, Apr. 2006.
- [9] M. D. LaHaye, J. Suh, P. M. Echternach, K. C. Schwab, e M. L. Roukes, "Nanomechanical measurements of a superconducting qubit," *Nature*, vol. 459, n°. 7249, pagg. 960-964, Giu. 2009.
- [10] R. Bashir, "BioMEMS: State-of-the-art in detection, opportunities and prospects," *Advanced Drug Delivery Reviews*, vol. 56, n°. 11, pagg. 1565-1586, 2004.
- [11] M. A. Burns et al., "An Integrated Nanoliter DNA Analysis Device," *Science*, vol. 282, n°. 5388, pagg. 484-487, Ott. 1998.
- [12] T. Thorsen, S. J. Maerkl, e S. R. Quake, "Microfluidic Large-Scale Integration," *Science*, vol. 298, n°. 5593, pagg. 580-584, Ott. 2002.
- [13] M. J. Levene, J. Korlach, S. W. Turner, M. Foquet, H. G. Craighead, e W. W. Webb, "Zero-Mode Waveguides for Single-Molecule Analysis at High Concentrations," *Science*, vol. 299, n°. 5607, pagg. 682-686, Gen. 2003.
- [14] A. M. Armani, R. P. Kulkarni, S. E. Fraser, R. C. Flagan, e K. J. Vahala, "Label-Free, Single-Molecule Detection with Optical Microcavities," *Science*, vol. 317, n°. 5839, pagg. 783-787, Ago. 2007.
- [15] "ETH - BEL - CMOS-based MEAs
<http://www.bsse.ethz.ch/bel/research/BioElectronics/MEAs>." [Online].
- [16] M. R. Prausnitz, "Microneedles for transdermal drug delivery," *Advanced Drug Delivery Reviews*, vol. 56, n°. 5, pagg. 581-587, Mar. 2004.
- [17] G. Binnig, C. F. Quate, e C. Gerber, "Atomic Force Microscope," *Physical Review Letters*, vol. 56, n°. 9, pag. 930, Mar. 1986.
- [18] M. Rief, M. Gautel, F. Oesterhelt, J. M. Fernandez, e H. E. Gaub, "Reversible Unfolding of Individual Titin Immunoglobulin Domains by AFM," *Science*, vol. 276, n°. 5315, pagg. 1109-1112, Mag. 1997.
- [19] G. G. Stoney, "The Tension of Metallic Films Deposited by Electrolysis," *Proceedings of the Royal Society of London. Series A*, vol. 82, n°. 553, pagg. 172 -175, Mag. 1909.
- [20] H. Butt, "A Sensitive Method to Measure Changes in the Surface Stress of Solids," *Journal of Colloid and Interface Science*, vol. 180, n°. 1, pagg. 251-260, Giu. 1996.
- [21] J. Fritz et al., "Translating Biomolecular Recognition into Nanomechanics," *Science*, vol. 288, n°. 5464, pagg. 316-318, Apr. 2000.
- [22] D. L. Stokes e T. Vo-Dinh, "Development of an integrated single-fiber SERS sensor," *Sensors and Actuators B: Chemical*, vol. 69, n°. 1, pagg. 28-36, Set. 2000.
- [23] L. Nicu et al., "Resonating piezoelectric membranes for microelectromechanically based

bioassay: Detection of streptavidin-gold nanoparticles interaction with biotinylated DNA,” *Sensors and Actuators, B: Chemical*, vol. 110, n° . 1, pagg. 125-136, 2005.

- [24] B. Ilic et al., “Single cell detection with micromechanical oscillators,” *Journal of Vacuum Science & Technology B: Microelectronics and Nanometer Structures*, vol. 19, n° . 6, pag. 2825, 2001.
- [25] A. Gupta, D. Akin, e R. Bashir, “Single virus particle mass detection using microresonators with nanoscale thickness,” *Applied Physics Letters*, vol. 84, n° . 11, pag. 1976, 2004.
- [26] B. Ilic, Y. Yang, K. Aubin, R. Reichenbach, S. Krylov, e H. G. Craighead, “Enumeration of DNA Molecules Bound to a Nanomechanical Oscillator,” *Nano Letters*, vol. 5, n° . 5, pagg. 925-929, Mag. 2005.
- [27] R. Best, *Phase Locked Loops 6/e: Design, Simulation, and Applications*, 6° ed. McGraw-Hill Professional, 2007.
- [28] Naika K., Hanay M. S., Hiebert W. K., Feng X. L., e Roukes M. L., “Towards single-molecule nanomechanical mass spectrometry,” *Nat Nano*, vol. 4, n° . 7, pagg. 445-450, Lug. 2009.
- [29] C. A. J. Putman, B. G. De Grooth, N. F. Van Hulst, e J. Greve, “A detailed analysis of the optical beam deflection technique for use in atomic force microscopy,” *Journal of Applied Physics*, vol. 72, n° . 1, pag. 6, 1992.
- [30] A. J. den Boef, “Scanning force microscopy using a simple low-noise interferometer,” *Applied Physics Letters*, vol. 55, n° . 5, pag. 439, 1989.
- [31] B. W. Hoogenboom et al., “A Fabry–Perot interferometer for micrometer-sized cantilevers,” *Applied Physics Letters*, vol. 86, n° . 7, pag. 074101, 2005.
- [32] D. W. Carr, “Measurement of nanomechanical resonant structures in single-crystal silicon,” *Journal of Vacuum Science & Technology B: Microelectronics and Nanometer Structures*, vol. 16, n° . 6, pag. 3821, 1998.
- [33] J. W. Noh, R. Anderson, S. Kim, J. Cardenas, e G. P. Nordin, “In-plane photonic transduction of silicon-on-insulator microcantilevers,” *Optics Express*, vol. 16, n° . 16, pagg. 12114-12123, 2008.
- [34] C. S. Smith, “Piezoresistance Effect in Germanium and Silicon,” *Physical Review*, vol. 94, n° . 1, pag. 42, Apr. 1954.
- [35] M. Tortonese, R. C. Barrett, e C. F. Quate, “Atomic resolution with an atomic force microscope using piezoresistive detection,” *Applied Physics Letters*, vol. 62, n° . 8, pag. 834, 1993.
- [36] Z. J. Davis et al., “Monolithic integration of mass sensing nano-cantilevers with CMOS circuitry,” *Sensors and Actuators A: Physical*, vol. 105, n° . 3, pagg. 311-319, Ago. 2003.
- [37] S. Ghatnekar-Nilsson et al., “Resonators with integrated CMOS circuitry for mass sensing applications, fabricated by electron beam lithography,” *Nanotechnology*, vol. 16, n° . 1, pagg. 98-102, 2005.

- [38] Q. P. Unterreithmeier, E. M. Weig, e J. P. Kotthaus, "Universal transduction scheme for nanomechanical systems based on dielectric forces," *Nature*, vol. 458, n°. 7241, pagg. 1001-1004, Apr. 2009.
- [39] K. L. Ekinci, X. M. H. Huang, e M. L. Roukes, "Ultrasensitive nanoelectromechanical mass detection," *Applied Physics Letters*, vol. 84, n°. 22, pag. 4469, 2004.
- [40] B. Ilic, S. Krylov, K. Aubin, R. Reichenbach, e H. G. Craighead, "Optical excitation of nanoelectromechanical oscillators," *Applied Physics Letters*, vol. 86, n°. 19, pag. 193114, 2005.
- [41] M. J. Madou, *Fundamentals of Microfabrication: The Science of Miniaturization, Second Edition*, 2° ed. CRC Press, 2002.
- [42] S. Franssila, *Introduction to Microfabrication*, 1° ed. Wiley, 2004.

Experimental Details and Pillar Approach

2.1 Introduction

In the previous chapter we introduced the basic principle behind cantilever sensing; the adsorption of an analyte changes the mechanical properties of the beam. In the dynamic mode, the loaded mass causes a change of the resonance frequency like in a quartz micro balance. However, due to the small cantilever mass, it is possible to achieve sensitivity down to zeptogram (10^{-21} g) [1]. According to the spring-mass model [2] the resonance frequency is given by

$$f_0 = \frac{1}{2\pi} \sqrt{\frac{k}{m^*}}$$

where k is the elastic constant, and m^* is the reduced mass of the cantilever. If a mass, Δm , is added the frequency changes according to:

$$f_{\Delta m} = \frac{1}{2\pi} \sqrt{\frac{k}{m^* + \Delta m}}$$

However this is an approximation that does not take into account two very important physical processes. The variation depends on the position where the adsorption takes place [2] and the adsorbed molecules affect the elastic properties of the beam [3]. A more accurate equation is:

$$f_{\Delta m} = \frac{1}{2\pi} \sqrt{\frac{k[\Delta m]}{m^* + \gamma \Delta m}}$$

where now k is a function of the adsorbed mass and γ is a geometrical parameter determined by the location of absorption. So it is clear that measuring only the resonance frequency does not provide any quantitative result. There are some approaches to address this issue, for example, to define lithographically a small adsorption spot (see Figure 5c in Chapter 1 [4]) this solution has two main drawbacks. First, it cannot be easily scaled down to the nanoscale dimension: when the cantilever size is close to the resolution limits imposed by the lithography, the adsorption spot

cannot be precisely defined using the same process. Second, if an array of detectors has to be fabricated, the active area results to be only a tiny fraction of the overall detector size. In the ref [4] is only $5 \cdot 10^{-7}$. In these conditions the detection of very low concentrations of analyte becomes impossible in spite of the high sensitivity of the detection method; because the target molecules take a too long time to reach the adsorption spot because of the slowness of the diffusion process.

A second solution, which actually faces only one of the underlined issues, is to analyze statistically many adsorption events [5], [6]. In this case the whole surface of the detector is used, and the different frequency shifts linked to different landing positions is calculated under the hypothesis of discrete events. In this way is possible to extrapolate the total mass of the adsorbed species. This approach not only is a partial solution but also it may provide very slow detection efficiency due the accumulation time of the data.

An alternative configuration consists in the fabrication of vertical microstructure (pillars) that protrude out of the wafer surface [7-10]. This simple variation allows the functionalization of the face at the free end of the beam in very easy way giving several advantages. By a directional deposition system, such as thermal evaporation, it possible to coat with a metal layer the top face of the pillar. This coating is automatically self-aligned at the very end of the resonator without the use of any lithographic tool. The fabrication process can thus be pushed to its intrinsic limit without loss of alignment precision. By choosing a specific interaction, typically gold-thiol, the adsorption is localized on the metal surface which corresponds exactly to the end of the beam. The adsorbed analyte does not induce any stress on the oscillating part of the pillar that corresponds to the side walls. Moreover, all mass is localized exactly at the end of the beam and the spring model can be correctly applied in order to associate the change in frequency with adsorption.

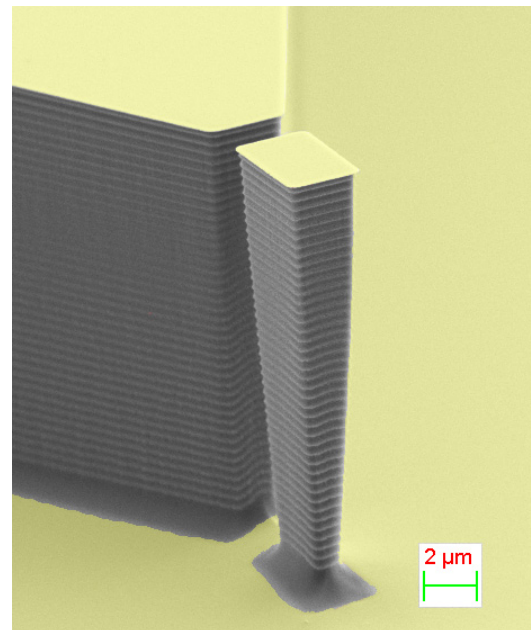


Figure 1. Scanning electron microscope image of a 15 μm -height pillar after gold deposition. The gold layer is colored to show that lateral wall and the base are not coated.

Furthermore, the fabrication process is intrinsically symmetrical, so that all the vertical walls are equally finished and no asymmetrical residual stresses are induced by fabrication as in the case of horizontal geometry. There are no stiction effects when used in liquid/dry environment.

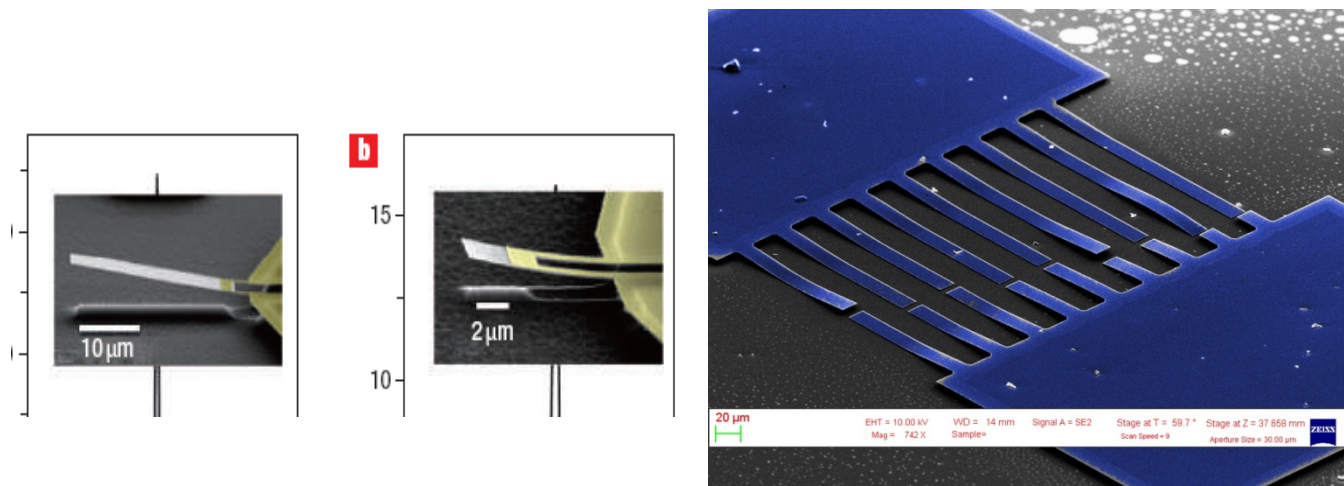


Figure 2. It shows two typical problems of standard cantilever fabrication: a) in a bilayer cantilever, different stress of the two surfaces induces an undesired bent (Figure from [11]). b) During a drying of a sample with suspended cantilevers the capillary force of the liquid causes the two surfaces to adhere permanently.

2.2 Fabrication

The fabrication consists of two main processes: the definition of the cross section by lithography and a deep anisotropic etching (Figure 3). In addition, there are also some cleaning and surface preparation steps.

The starting material is a (1 0 0) oriented, single side polished, P-type silicon wafer. After piranha (H_2O_2 (35%): H_2SO_4 = 1:3 at 90 °C) and HF cleaning a 100 nm silicon dioxide layer is grown by PECVD.

The oxide thin layer has the function of protecting from contaminations and defect produced during the fabrication process, the portion of the substrate which will be the top area of the pillar. At the end of the fabrication the chip sample is dipped in an HF solution that dissolve completely the layer removing all the residuals of the

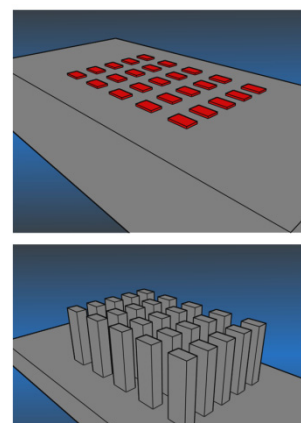


Figure 3. Scheme of pillar fabrication. Definition of the cross section and deep vertical etching.

fabrication and leaving a very clean, flat silicon surface like the starting wafer surface. Figure 3 shows two final surfaces, on the left there is one which was not protected by the oxide layer, on the right the surface after the protective layer has been removed: the difference in the surface quality is remarkable.

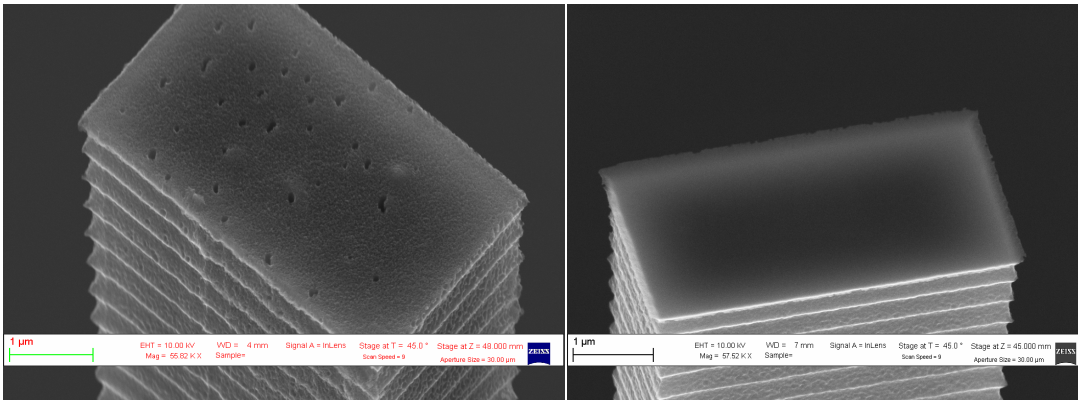


Figure 4. SEM images of the top surface of two pillars.

The sample is spin coated with 500 nm of poly-methylmethacrate (PMMA) 950 K resist (4000 rpm) and baked for 10 min at 180 °C.

The pillar in-plane geometry and the overall patterning are defined by e-beam lithography (Zeiss Leo 30 keV). We chose rectangular cross section because the spectrum of mechanical response shows one well defined peak. A previous attempt with optical lithography resulted in a rounded geometry, such as that shown in Figure 5. Unfortunately we were not able to detect any resonance in those structures. We explained this as follows. Perfectly circular resonators have infinite degenerate mode at the same eigenfrequency. However any slight imperfection results in the formation of two separated modes along the major and minor diameter directions. These modes can couple giving rise to circular polarized oscillations [12]. The amplitude of those oscillation is significantly smaller than the amplitude of a linear oscillator and therefore cannot be detectable in a standard configuration.

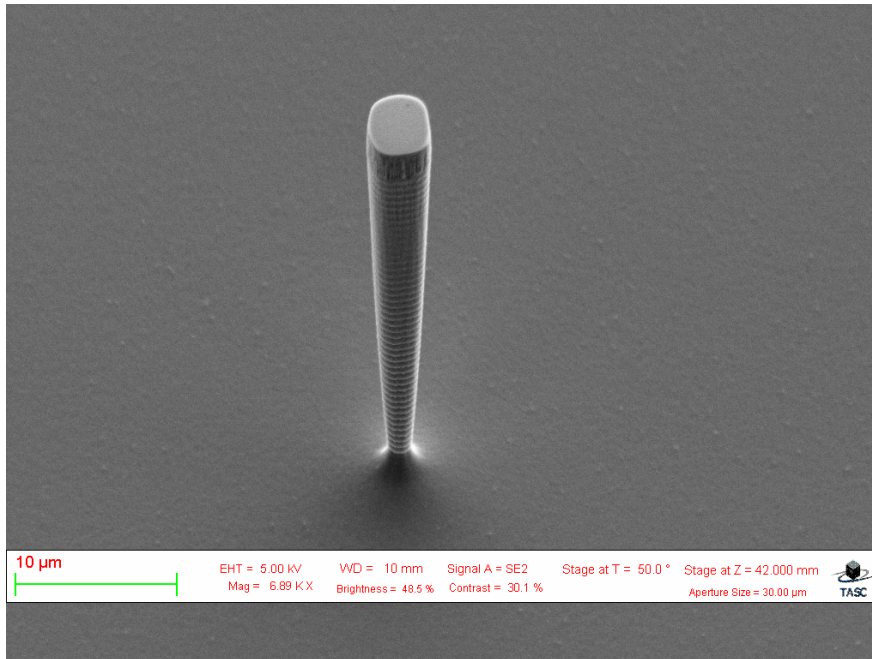


Figure 5. A conic pillar made by means of optical lithography. The height is 19 μm and the diameter is 4 μm .

After PMMA developing in a conventional 1:3 MIBK/IPA developer for one minute, a 20 nm nickel layer is evaporated by means of e-beam and the Ni mask for the subsequent dry etching is obtained through a lift off process by removing the resist in hot acetone.

Before the etching, oxygen plasma is performed in order to remove the residual resist and argon plasma is used to define better the metal mask. We have developed a Bosch™-like process to obtain a deep etching for both silicon and silicon oxide with an Inductively Coupled Plasma reactor (ICP, STS-Surface Technology). For passivation, we use plasma of mixture of C_4F_8 and Ar (100 and 20 sccm) at a pressure of 7 mTorr and with 600 W of RF power applied to the coil. For etching we use a plasma of mixture of SF_6 and Ar (110 and 20 sccm) at a pressure of 8 mTorr and with 600 W of RF power applied to the coil and 50 W to the platen. Many cycles are executed to remove silicon to create the vertical resonator. The duration of the process settles the height of the pillar. Typically, we remove almost 15 μm which correspond to 48 cycles. Differently from [7] we want avoid a strictly vertical profile. So the etching process has a small undercut ($\approx 4^\circ$, see Figure 6). Normally this is an undesired effect but in our case it results in a inverted tapered profile that has several advantages: the sensor mass is reduced (about 50%) without changing the sensitive area; the structure is insensitive to small misalignment during the top gold evaporation because of the intrinsic shadowing effect; the oscillation amplitude is increased, due to the thin pillar base; the

stress induced by the oscillation is confined on the pillar base, which is less affected by the thermal drift induced by the laser which is used for monitoring the motion of the pillar.

The metal mask and protective silicon oxide are removed providing a clean and flat silicon surface for the next functionalization process. First, the metal mask is dissolved by a 15 min dipping in piranha solution, and then the oxide is dissolved in hydrofluoric acid. The final step is to re-oxidize the devices which are put for 1 hour and half in furnace at 1100 °C in gentle flux of water vapor.

Bosch™ process

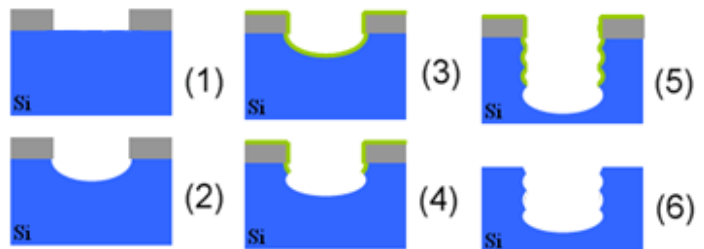
Deep vertical etching, fundamental technology of MEMS

Two step process:

- 1) Isotropic plasma etching (For silicon, this often uses sulfur hexafluoride [SF_6])
- 2) Deposition of a chemically inert passivation layer. (For instance, C_4F_8 source gas yields a substance similar to Teflon.

Each phase lasts several seconds. The passivation layer protects the entire substrate from further chemical attack and prevents further etching. However, during the etching phase, the directional ions that bombard the substrate attack the passivation layer at the bottom of the trench (but not along the sides).

These etch/deposit steps are repeated many times resulting in a large number of very small isotropic etch steps taking place only at the bottom of the etched pits causing the sidewalls to undulate with a vertical period of about 100–500 nanometer and the horizontal indentation of the order of 10nm.



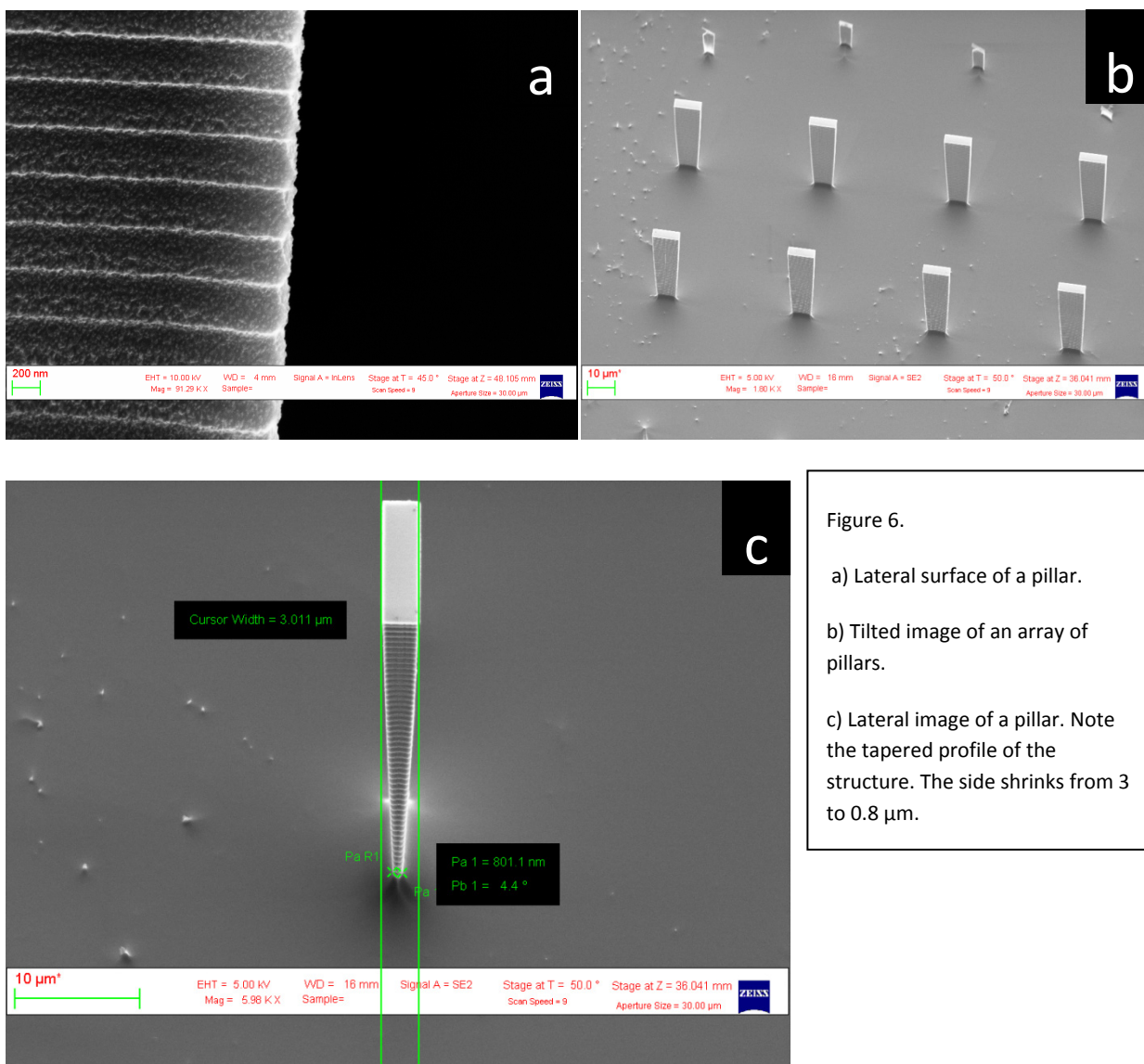


Figure 6.

- a) Lateral surface of a pillar.
- b) Tilted image of an array of pillars.
- c) Lateral image of a pillar. Note the tapered profile of the structure. The side shrinks from 3 to 0.8 μm.

We designed two kinds of devices:

1. Single pillars
2. Hexagonal lattice of pillar

The first configuration consists of isolated rectangular pillars in a 3x3 or 4x4 arrays. Each array is identified by a number; individual pillars can be identified using the symmetry defined by the number. This configuration was used for initial test and characterizations. The second configuration is thought to improve the functionalization in liquid. It was well known that the

roughness increases the hydrophobicity and recently it was demonstrated that a micro patterning of a surface results in a super hydrophobic states [13], [14]. Generally, an artificial super hydrophobic surface is produced by an array of vertical structures with a rather large aspect ratio displaced in a dense regular lattice. We fabricate devices with hexagonal lattice pattern. The lattice is made by 19 rows with 16 pillars. The distance between to neighbor pillar is $30\ \mu\text{m}$. The matrix is enclosed in a square corral that avoids water entering laterally at the bottom of the structure. The second, fundamental, fabrication step consists in the hydrophobication of the structure. Indeed, only when the material itself shows contact angle in excess of 90° for a flat surface, the microstructuring gives super hydrophobicity. On the contrary super hydrophilic surfaces area obtained [15], we made the surface of the pillars hydrophobic by depositing a layer of C_4F_8 (contact angle $\approx 120^\circ$).

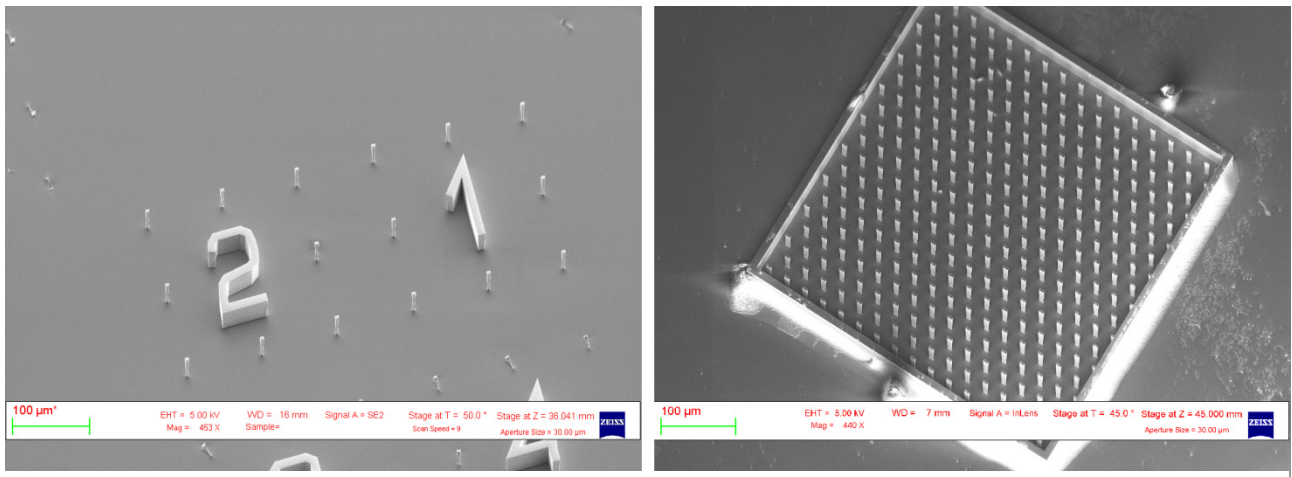


Figure 7. Electronic micrographs of the two kinds of patterning.

2.3 Experimental Setup

The displacement of the pillars at different frequency is measured by using the optical deflection method in vacuum.

2.3.1 Vacuum

The device is placed into a home build small vacuum chamber, evacuated with a turbo – rotary pump system with base pressure better than 1×10^{-6} mbar. The rotary pump is an oil-free root pump and the turbo is a 70l/s equipped with magnetic bearings which can be mounted directly on

the chamber thus improving evacuation time and base pressure. The rotary pump is mechanically decoupled from the chamber by means of a heavy attenuator. The pressure is constantly monitored with a full scale gauge, because measurements can be compared only if are taken in the same condition due to the dependence on pressure of the mechanical properties of a cantilever [16]. Figure 8 shows the pressure dependence of the quality factor and the resonance frequency. Our setup is not equipped with a feedback loop that allows maintaining the system at a fixed pressure, therefore we always worked at the base pressure which is determined by the pumping speed, chamber size and chamber components and is consistent within different experimental runs. In order to perform measurements as a function of the pressure we just turned off the pumping system and waited the pressure natural raise. The pressure rises up to the atmosphere value due to the leakage of the chamber. Till to 10^{-3} the variation is slow but after that it is very fast so we do not have data for the medium vacuum regime where the transition between the viscous and molecular regime takes place. It worth to note that atmospheric pressure pillars still have a relatively high Q-factor, around 1000.

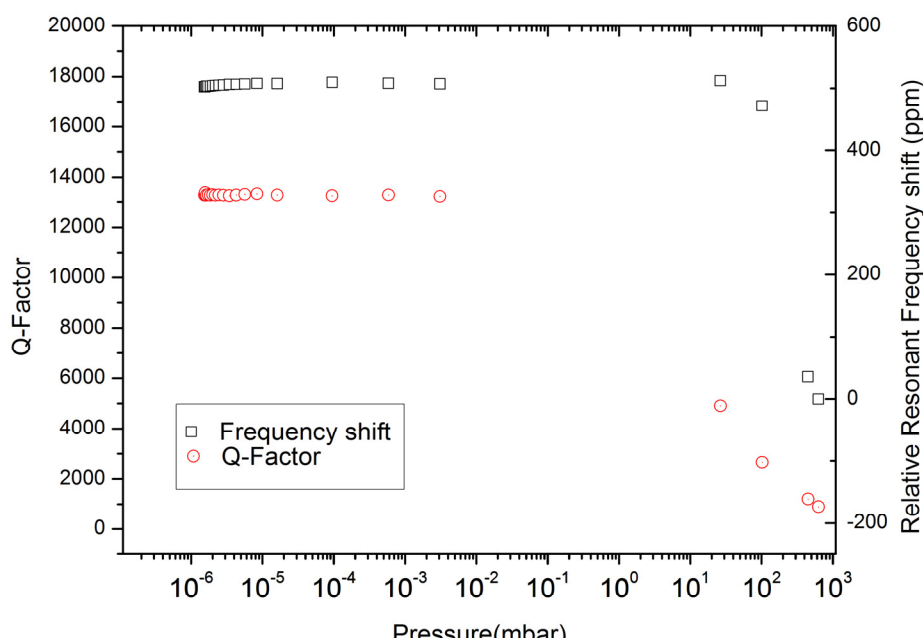


Figure 8. Trend of the resonance frequency and Q – factor in function of pressure.

2.3.2 Optical Setup

The optical setup is build using the cage system (from Thorlabs™) that consists in a rigid armature of four steel rods, where the optical components are mounted along a common optical axis. The distance between two near rods is 30 mm. The setup serves the purpose to focus a laser beam in a spot of few microns, to focus on a photodetector the light reflected from a pillar and to visualize by means of a CCD camera the laser spot and the device. The source is a DPSS green laser (532 nm) that can be modulated from 0 to 100 mW. A relatively high power is needed because of the several reflections along the optical path that reduce the actual power reflected by the pillar on the photodetector. Almost $1/10^{\text{th}}$ of the incident power reaches the pillar surface. A long working

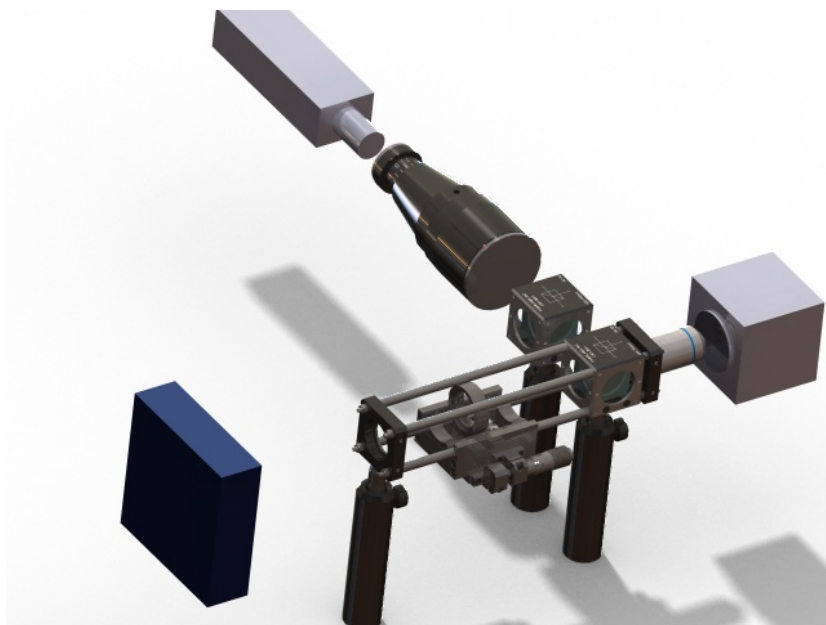


Figure 9. 3D Rendering of the optical setup

distance microscope objective (LMPLFLN 20X Olympus) with 0.4 numerical aperture and 12 mm working distance focuses the laser to a spot of few microns. The diameter of the entrance pupil of the objective is around 7 mm and the beam radius of the laser must be expended in order to illuminate all the optics of the objective. For this a 10x beam expander is mounted between the laser and the objective. A cubic beamsplitter divides the incident and the reflective light. A tube lens, (focal lens 200 mm) is used to correct the infinity focus of the objective. A second beamsplitter serves the purpose to add a white light in optical path for the illumination. The source is a common fiber optic illuminator. A mirror, after the tube lens, can direct the light either to the photodetector or to a CCD camera (GANZ™ ZCF11C4 or THEIMAGINGSOURCE™ DBK

41BU02). Alternatively, with a further beamsplitter it is possible to achieve the imaging and the detection at the same time with the drawback to halve the signal on the photodiode. Before the CCD camera a long pass filter (610nm) stops the laser light allowing only the imaging light to reach the detector otherwise the laser intensity would saturate the sensor of the camera. The portion of the incident light that pass through the beamsplitter orthogonally respect to the objective is monitored by a power meter sensor. As it will discuss in a following section, the heating induced by the laser modifies the mechanical properties of the pillars so it is important to always measure and control the laser power.

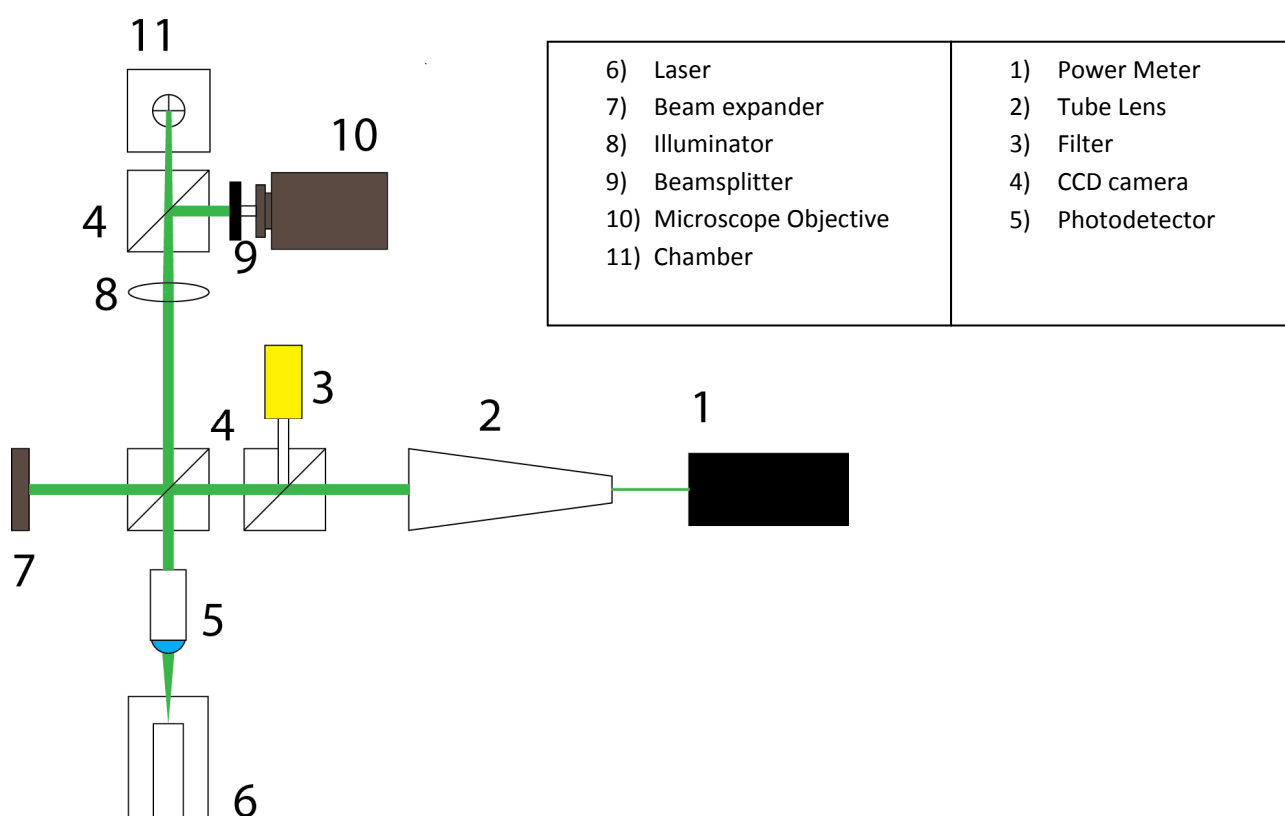


Figure 10. Scheme of the experimental set up.

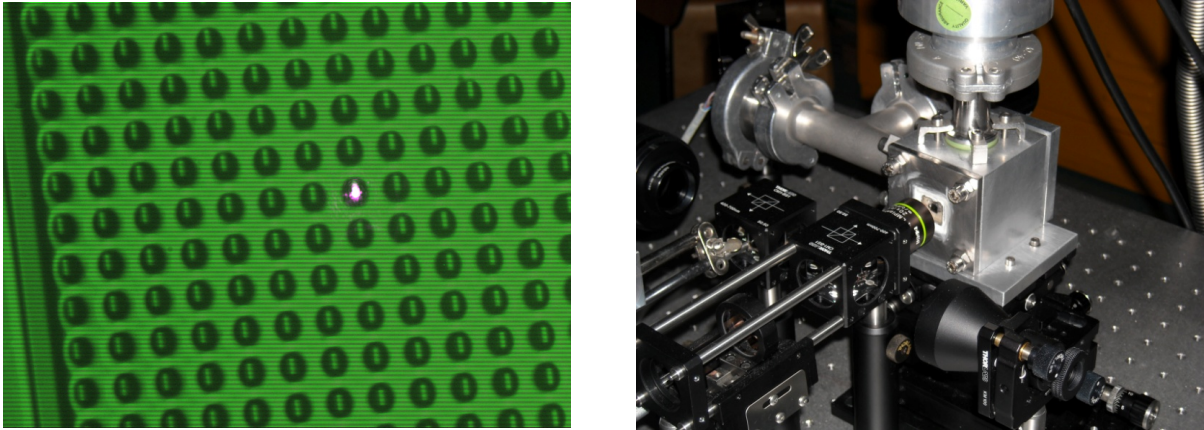


Figure 11. Left) Image taken from the CCD camera. The white spot is the spot of the laser. Right) Photo of the chamber.

2.3.3 The Mechanical Mounting

The optical system is fixed and the scanning over the sample is realized by moving the entire chamber by means of a xy micrometric translation stage and on a lab jack. A second xyz stage controls the position of the photodetector. Moreover a high precision rotation stage can turn the sensor around the optical axis of the system. The sample holder is designed to be fast placed by means of a dovetail sliding interlocking (see fig.12). The chips are mounted on a chips support made of PEEK with four chip-slots equipped with four $3 \times 5 \times 1$ mm

piezoelectric crystal (lead zirconate titane) which are used as actuators. Their capacity ranges from 0.5 to 1.2

nF. The samples are directly glued to the crystals by means of bi adhesive tape. An alternative mechanical mounting with mechanical clamps has been implemented but the resulting mechanical coupling was too weak to actuate the resonators. We used piezo with both vertical and shear polarization but we did not notice any significant difference in the amplitude of motion of the

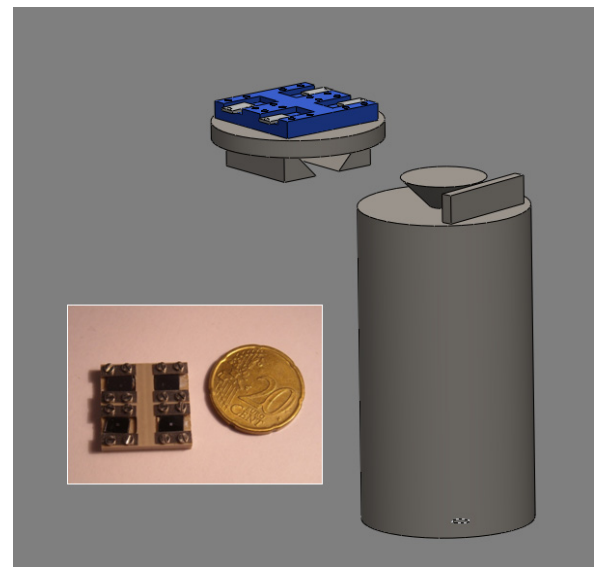


Figure 12. The sample holder.

pillars. This suggests that the direction of vibration of the piezo has a small influence on the motion of a pillar and we speculated that the actuation is given by a non-specific coupling and not by a direct force.

2.3.4 The Photodetector and the Acquisition System

The photodetector has a fast four quadrant photodiode (Hamamatsu S7379-01, cut off frequency ≈ 80 MHz) and a dedicated homemade electronics. The four signals of the four quadrants are amplified and mixed generating two outputs: the x and y positions of the spot respect to the center of the photodiode. These values are proportional to the displacement of the illuminated pillar. The electric circuit is shown in Figure 14. By monitoring the two signals with a multi-channel oscilloscope the photodiode is aligned with the laser beam.

A network analyzer (3577A Hewlett–Packard) generates a sweeping signal which excites the piezo that makes the pillars to oscillate. Depending on the orientation of the pillar, the vertical or the horizontal signal is acquired by the analyzer which filters the component of the signal at the actuation frequency and provides the amplitude and the phase difference. The instruments allow collecting 401 points and the typical frequency span is 10 KHz. The duration of the sweep is 60 second. . We do not take just one spectrum because we observed that the resonance frequency tends to increases with time till it gets to stable values. This effect is probably due to the evaporation of water that is adsorbed on the pillar either from the ambient humidity or from a direct dipping in a solution. We do a periodic collecting of the spectra for a specific duration. Typically, the rate is every 2 minutes for 20 minutes. This time is enough to obtain a stable value.

By fitting the data with a lorentzian function the center x_c and the width w give the value of the resonance frequency (x_c) and of the Q-factor (x_c/w).

We have developed a program with Labview™ software which can interface with the network analyzer. It is possible to set the instrument, to trigger the measure, to fit and to collect the data.

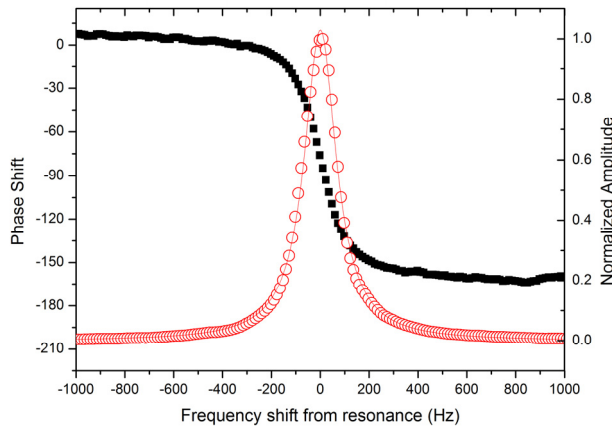


Figure 13. Resonance peak and phase shift of a pillar with one of the highest Q value we have measured (30000). The resonance frequency is 4.77 MHz.

Why a lorentzian?

If we take the square of the magnitude of the spectral response which is proportional to the energy of the oscillator

$$x(\omega) = \frac{F}{m} \frac{1}{\sqrt{(\omega_0^2 - \omega^2)^2 + (\gamma\omega)^2}}$$

We get

$$\begin{aligned} x^2(\omega) &= \left(\frac{F}{m}\right)^2 \frac{1}{(\omega_0^2 - \omega^2)^2 + \left(\frac{\omega_0}{Q}\omega\right)^2} \\ &= \left(\frac{F}{m}\right)^2 \frac{1}{((\omega_0 - \omega)(\omega_0 + \omega))^2 + \left(\frac{\omega_0}{Q}\omega\right)^2} \end{aligned}$$

The most interesting part of this curve is near the resonance and if Q is high we can do the following approximation

$$(\omega_0 + \omega)(\omega_0 - \omega) \cong 2\omega_0(\omega_0 - \omega) \text{ and } \frac{\omega_0}{Q}\omega \cong \frac{\omega_0}{Q}\omega_0$$

So the previous equation can be rewritten:

$$\begin{aligned} x^2(\omega) &= \left(\frac{F}{m}\right)^2 \frac{1}{4\omega_0^2(\omega_0 - \omega)^2 + \omega_0^2\left(\frac{\omega_0}{Q}\right)^2} \\ &= \frac{1}{\omega_0^2} \left(\frac{F}{m}\right)^2 \frac{1}{4(\omega_0 - \omega)^2 + \left(\frac{\omega_0}{Q}\right)^2} \end{aligned}$$

This equation corresponds to the lorentzian function

$$y = \left(2 * \frac{A}{\pi}\right) * \left(\frac{w}{4 * (x - x_c)^2 + w^2}\right)$$

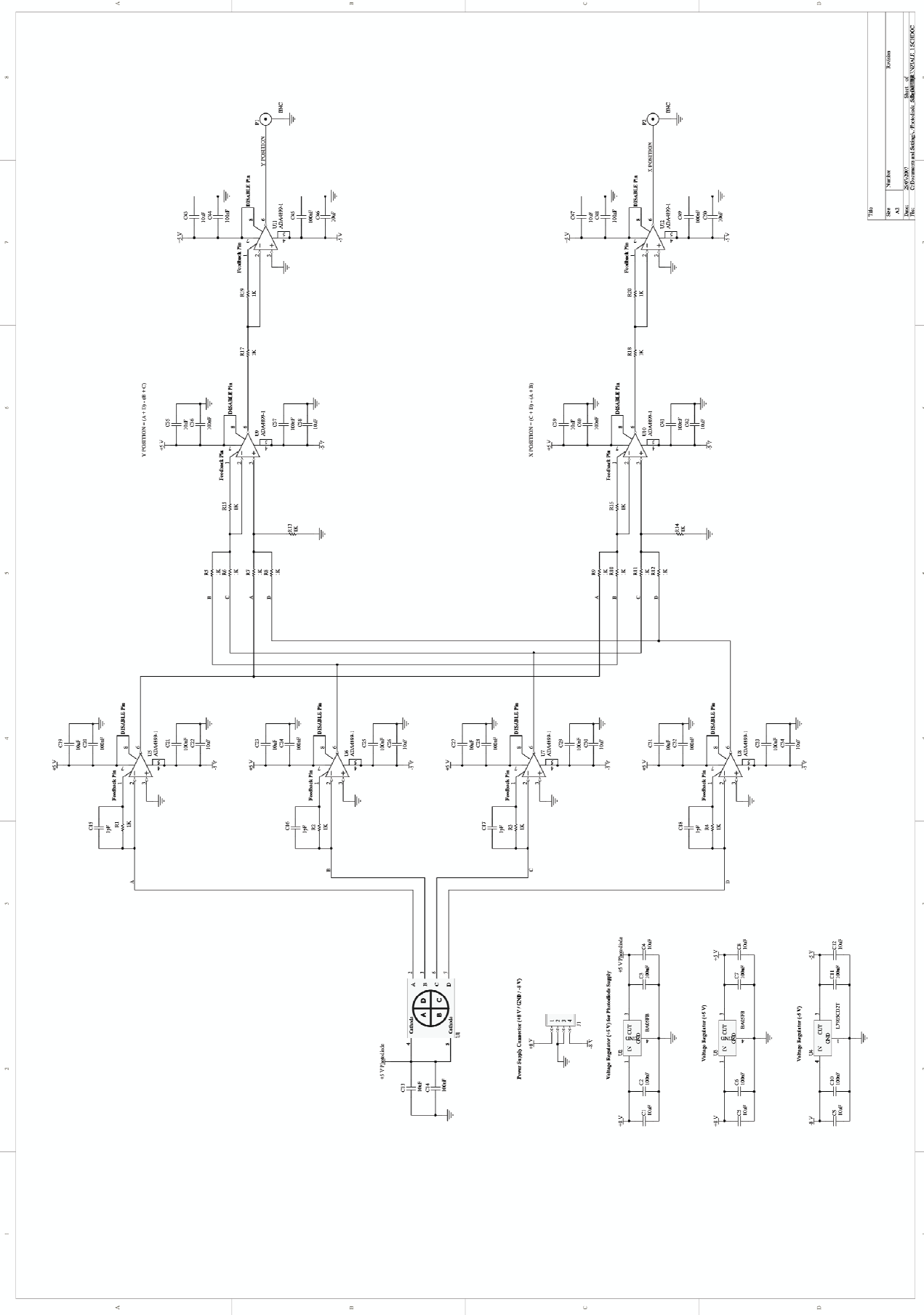


Figure 14. Electrical Scheme of the phodiode electronics.

2.4 Pillar Characterization

The etching time was chosen to achieve pillars of height 15 μm . Typical dimensions of the cross section are 3x5 μm or 3x8 μm . The lateral wall are not vertical respect to the substrate but are tilted. At the base the cross section is reduced to 0.8x2 μm or 0.8x6 μm . In the tapered geometry, the section is function of the depth. Since the undercut angle is constant we can approximate the thickness with the equation $t = t_0 \left(1 - \frac{L}{L_0}\right)$, where t_0 is the lengths of the initial cross-section and

L_0 is the etching depth at which the base of the pillars has zero dimension. The resonance frequency of a standard cantilever is proportional to t/L^2 . In the case of pillar we assume the same relation but we substitute t with the previous equation. So we the resonance frequency is proportional to: $A * t_0 \left(\frac{1}{L^2} - \frac{1}{L * L_0}\right)$. We are assuming that the behavior of a tapered beam is mainly affected by the thickness at the base where the most of the strain is concentrated.

Figure 15 shows the results of a finite element simulation and the fit of the result. The resonating frequencies are computed at different etching depths. The fit is excellent confirming that our guess could be correct but experimental evidence is missing. However, this hypothesis has the interesting consequence that pillars with small thickness at the base will act more like a pendulum than like a cantilever. This would reduce further the influence of adsorption on lateral surface because it will not change the compliancy of the pillar.

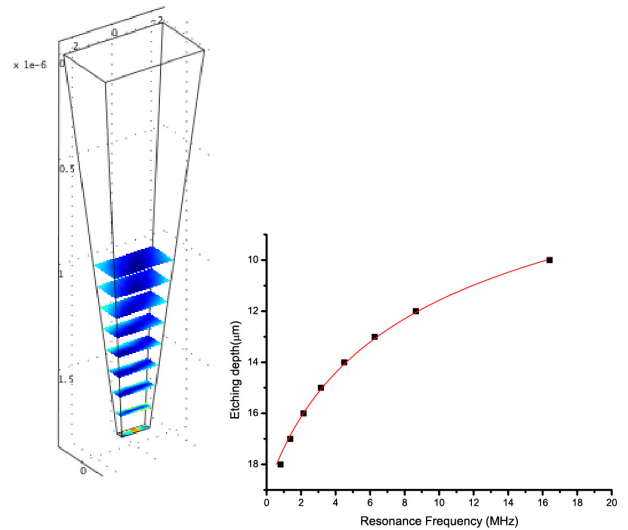


Figure 15. Simulation of the resonance frequencies at different etching depth.

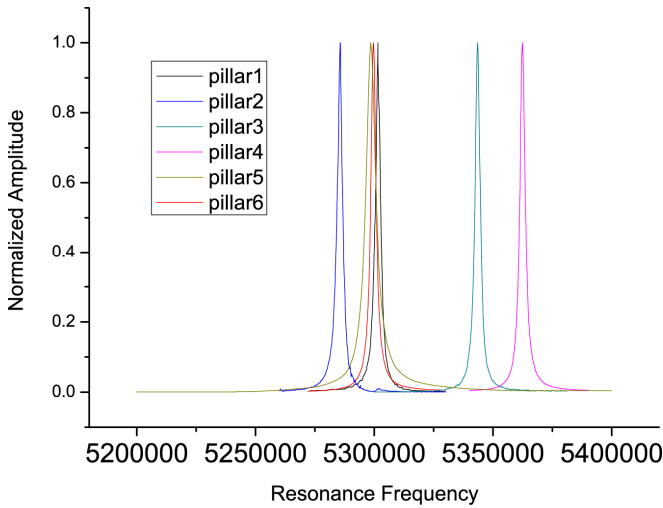


Figure 16. Resonance peaks of 6 different pillars on the same devices.

The simulation also tells that an error of the order of 0.1 μm on the depth of the etching causes an error on the frequency of the order 100 KHz. Figure 16 shows the distribution of the peaks of 6 different pillars on the same devices. The range of distribution is around 100 KHz. However, the same uniformity is not observed among different devices even if they come from the same batch. The resonance frequencies span from 4 to 10 MHz. In this case local fluctuations of the etching depth cannot explain

this large distribution because they should be too much high, 2 or 3 microns. Instead, it is likely due the lack of homogeneity of the lithography and lift-off which induced a variation on the dimensions of the cross-section.

The Q Factor ranges from 15000 to 20000 in vacuum but, recently, devices with a value of 30000 were produced (see Figure 13). This enhancement is due to the optimization of the final thermal oxidation.

The calibration of the sensor is made by coating the top with a metallic bi-layer (gold and titanium, where the latter is used ad adhesion layer). Since the metal deposition is a well controlled process by a calibrated microbalance inside the e-beam evaporators, we know the amount of the added material and we correlate it with change in frequency obtaining the sensitivity factor α

$$\alpha = \frac{\Delta m_{\text{au}}}{\Delta f_{\text{au}}} = \frac{h * S * \rho_{\text{au}}}{\Delta f_{\text{au}}}$$

where S is the pillar top surface, h is the thickness of the gold layer , ρ_{au} is the gold density and Δf_{au} the variation of resonance frequency after the deposition. We also take into account of the contribution of titanium layer even if here it is not explicitly shown.

Even the parameter α spans over a range of values from 20 to 35 Hz/fg with the resulting need of a calibration of each single pillar every time.

The graph 17a shows that the response of a pillar is linear over most of the range of the actuation energy, however it is possible to excite a pillar to the nonlinear regime and graph 17b shows the typical hysteretical resonance curves [17].

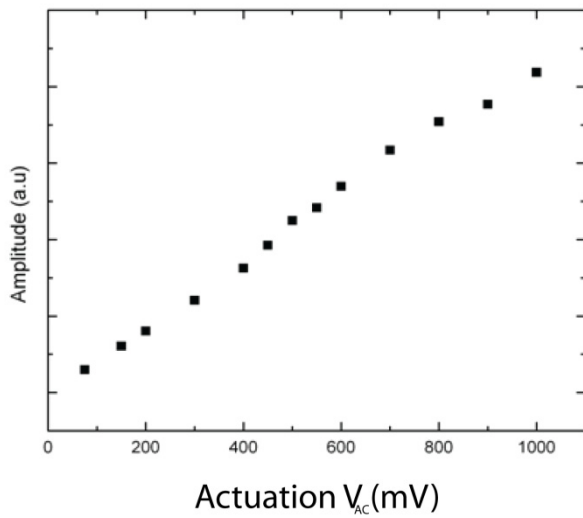


Figure 17. a) Amplitude vs. piezo actuation voltage (rms).

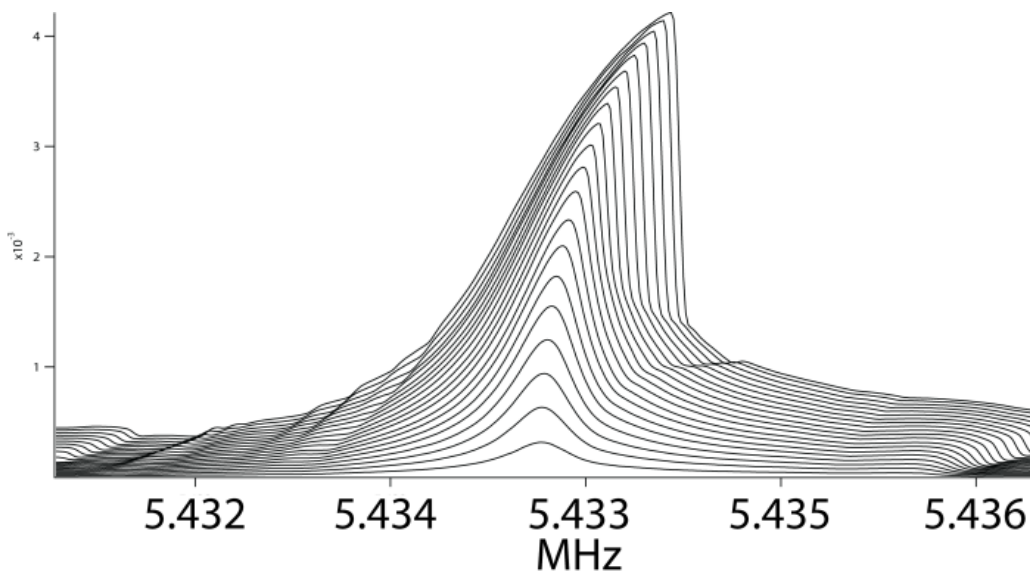


Figure 17. b) Vibration amplitude versus frequency, for various driving powers at the sample.

The dynamic range is a commonly used concept to characterize a mechanical resonator [18]. It is defined as the ratio of its maximum vibration amplitude at the onset of nonlinearity (critical amplitude) to its displacement noise floor. Figure 18 shows a representative curve of a pillar actuated at the largest drive level in the linear regime. The noise floor is given by the offset of the curve. Therefore, the ratio of amplitude of the peak to offset gives the dynamic range that is about 30 dB.

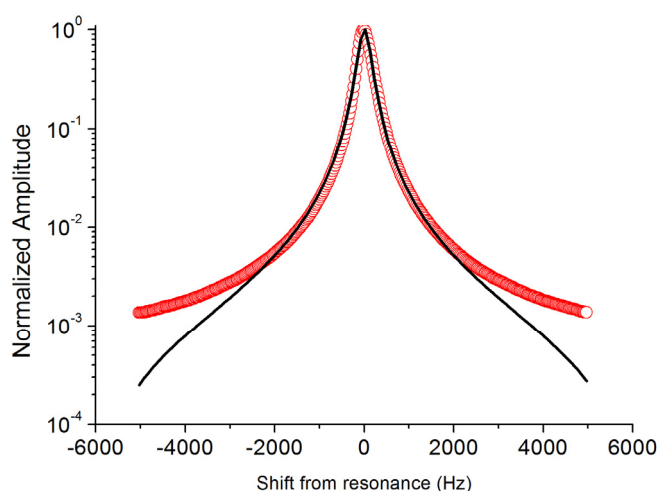


Figure 18. Vibration amplitude versus frequency shift from resonance (Log scale).

2.5 Laser and Water Influence.

We have investigated the influence of laser power on the resonance frequency due to the intrinsic heating. As previously reported [19], the resonance frequency changes in function of local temperature and the fluctuations of the measured values increase with temperature. We measured that almost the 40% of the incident light is absorbed by the pillars by measuring the power of light reflected by a silicon wafer coated with same metallization. We monitored the variation of frequencies by changing the power laser (Fig.19 left). We observed that the frequency

shift spans over a 1 KHz range by changing the power from 1 to 5 mW. We have optimized the optical setup and minimized the power absorbed on the pillar surface to less than 100 μW to reduce the heating of the laser. Finite element simulation shows that this adsorbed power produces less than 0.1 $^{\circ}\text{C}$ of temperature variation. The RMS stability of our measure is better than 2 Hz (corresponding to 0.06 fg) over 1 h of measurement (Fig. 19 right).

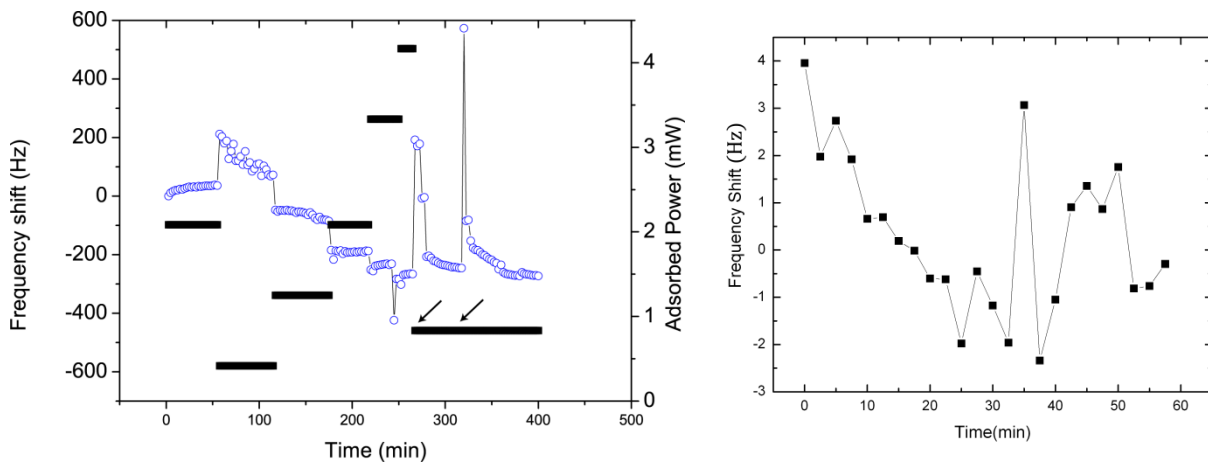


Figure 19. Left: the change of frequency due to laser heating versus time (min) of a pillar with a resonance frequency of about 5 MHz. The horizontal lines indicate the laser power; the arrows indicate two points where laser was turned off for 5 minutes. . Right: time stability of the resonance frequency when the laser power adsorbed is reduced to 100 μW ($f_0=5.1$ MHz).

We also studied the effect on the pillars of the interaction with water due to a direct dip. We observed that every time a sample is immersed in water the resonance frequencies of the pillars shift to a lower value probably due to either the water adsorption or the silicon oxidation. However, the observation that we did not reach saturation even after several consecutive dipping suggested that the silicon oxidation was the main mechanism responsible of this effect. In order to avoid it we tested two different strategies. First, we functionalized the pillars with a hydrophobic molecule, Octadecyl trichloro silane (OTS). However this did not work and we still observed steps as it shown in Figure 17. Alternatively we oxidized the by means of a thermal treatment. After the first bath the still measured a variation in resonance frequency, which is probably due to water molecules electrostatically bound to the oxidized surface but after the formation of a stable water layer the pillars frequency response is no longer affected by subsequent immersion in water. Actually, before getting to the steady value there is an evaporation phase since the water layer stability differs in vacuum and in air.

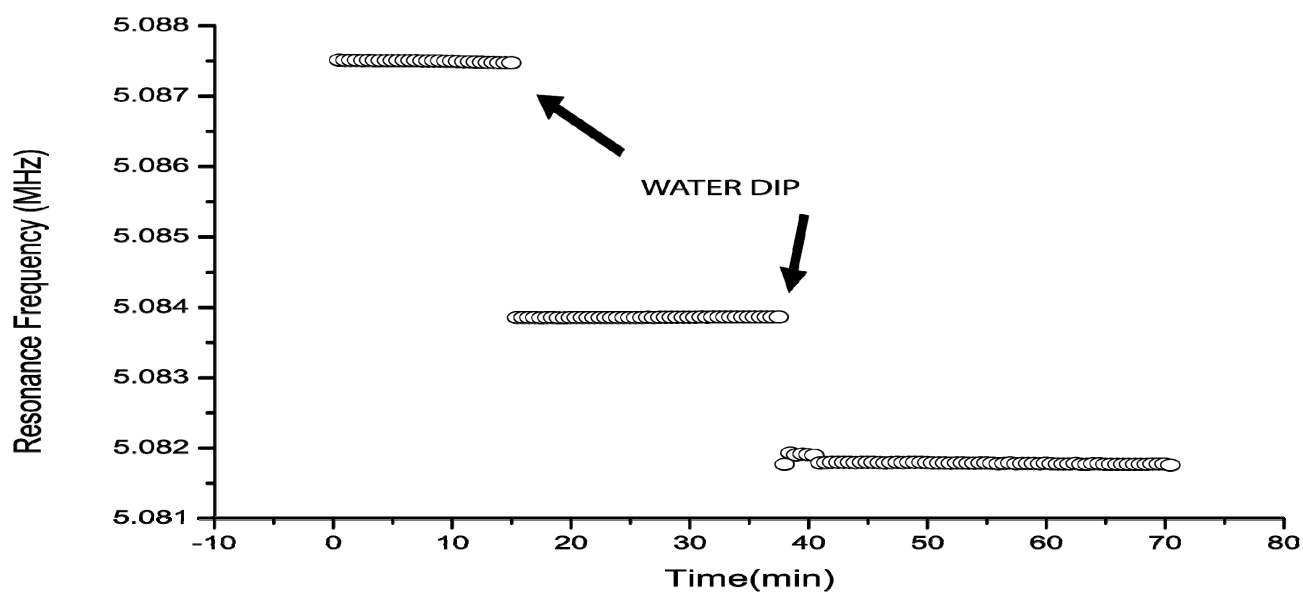


Figure 20. After having measured the resonance frequency of a silanized sample we dipped it in water and then we measured the resonance frequency. The shift was about 4 KHz. We repeated the immersion and we measured a further step of about 2 KHz.

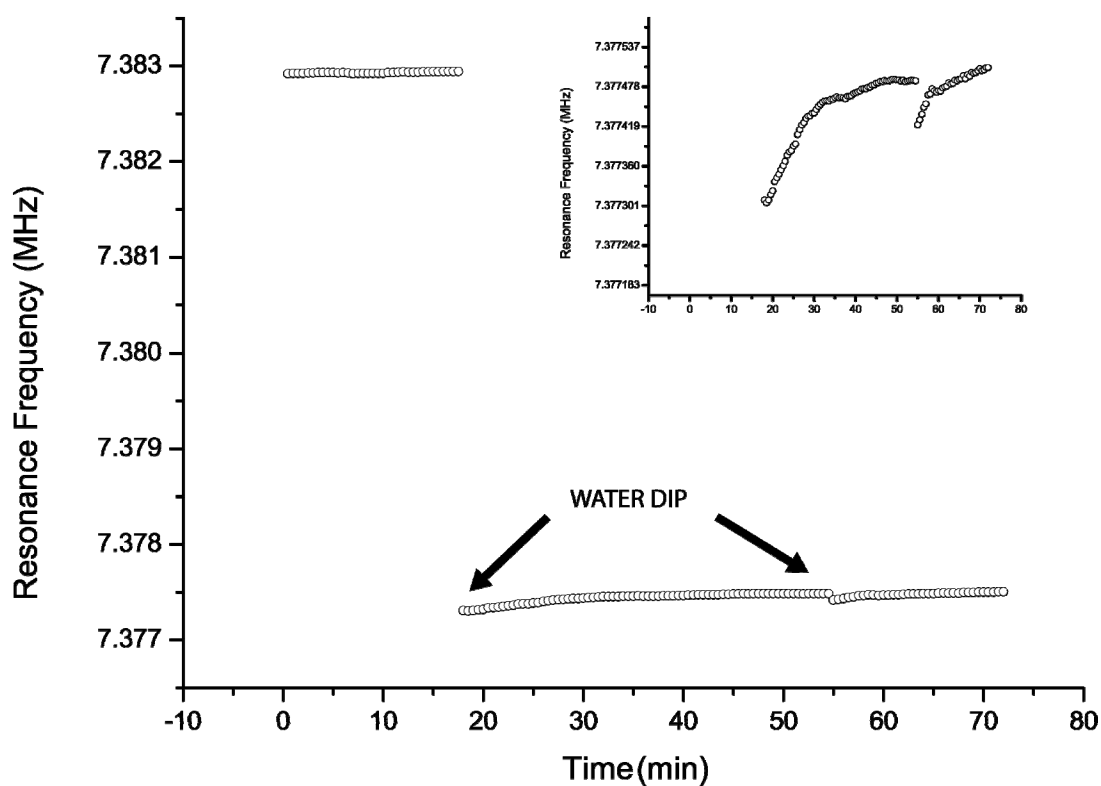


Figure 21. After having measured the resonance frequency of an oxidized sample we dipped it in water and then we measured the resonance frequency. The shift was about 6 KHz. We repeated the immersion but we did not observe a further step. The inset shows a blowup of the last part of the trend.

2.6 The “dip and dry” Method

If a pillar, like all the mechanical resonators, is operated inside a viscous medium it will lose all its advantages because the quality factor dramatically deteriorates and accordingly the sensitivity.

However in chemistry and to a larger extent in life science the liquid environment is the natural environment where experiments should be performed. To address this issue, recently it was proposed to put liquid inside the resonator by means of microchannel [20]. An alternative approach, which is called “dip and dry”, allows measuring in vacuum [21], [22]. In this scheme, the devices are put in liquid where all the chemical reactions take place than after being dried they are mounted the vacuum chamber and the resonance frequencies are measured. Successively the samples can be put in a further solution for new reactions and again dried for the measurement. In principle, the dip and dry cycle can be indefinitely repeated but due to contaminations more than four reactions can hardly achieved. However, this technique cannot always be used, for example for molecules which are not stable outside a liquid ambient. Also drying can change some properties of molecules making them useless for following cycles. Moreover, real time measurements are not possible and, so, we can investigate only the kinetics of reactions which has a relative long time scale (hours).

We tested the properties of our devices by forming on the top of calibrated pillars a SAM of HS-(CH₂)₁₁-(OCH₂CH₂)₆-OH (MW 424 Da) by dipping one freshly gold-coated device in a 100 μM ethanol solution for 12 h [10]. We measured an average shift of 2100 Hz which correspond to the mass of 64 fg. The corresponding density is about 6.1×10^{14} mol/cm² which is 10% higher than the closed-packed value of 5.5×10^{14} mol/cm² which corresponds to a $\sqrt{3} \times \sqrt{3}$ reconstruction of the (1 1 1)Au surface. We also observed that the width of resonance does not change after the functionalization step. This addressed two important points. First, the “dip and dry” approach can be correctly applied and second molecular adsorption is actually driven only on the top of the pillar. In fact adsorption on the lateral wall would deteriorate the quality factor. In order to further

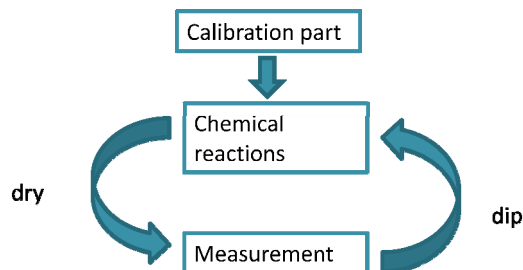


Figure 22. Scheme of the Dip and Dry method

demonstrate the latter statement we made the same experiment using standard cantilever and we observed, instead, that the Q factor is highly reduced suggesting that the molecular adsorption induced a significant dissipation as we expected Figure 23).

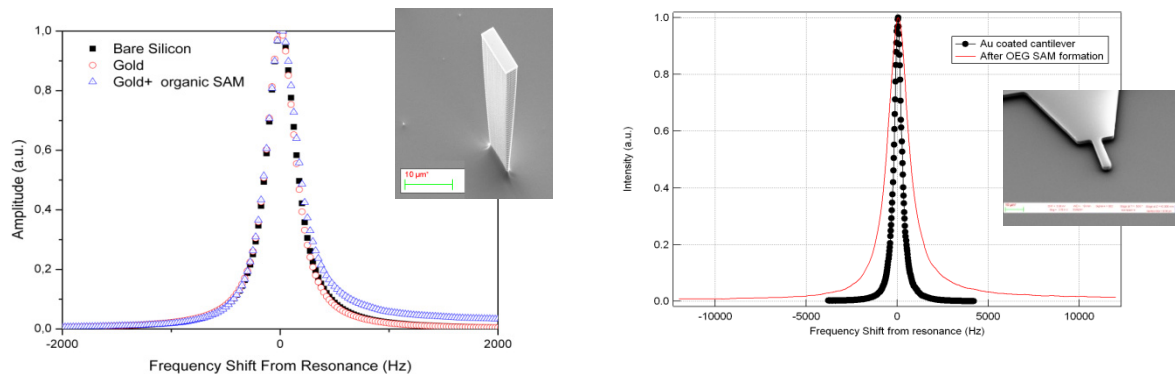


Figure 23. Vibration amplitude versus frequency shift from resonance before and after the functionalization.

However, the 10% extra added mass indicated that some point like non-specific adsorption occurs also on the lateral walls of the cantilevers, probably large impurities present in the solution. In order to avoid this we investigated the possibility of bringing in contact with the solution only the top area of the pillars rather than the entire chip.

This can be achieved exploiting a very interesting property of micro patterned hydrophobic surface [13], [14]. The contact angle of a drop of water on such flat surface is typically of the order of 100° to 120° . Wenzel model of hydrophobicity affirms that roughness, defined as the ratio of the actual over the apparent surface area, geometrically enhances hydrophobicity and the contact angle can reach values $> 150^\circ$ (super hydrophobic state). However, If the substrate is very hydrophobic or very rough the Wenzel model predicts a complete drying of the surface, with the contact angle = 180° . This result is clearly wrong because it is nonsense from a physical point of view. On the contrary the Cassie model, describes better these limit situations. The model states that air can remain trapped below the drop that stands partially on air resulting in a super hydrophobic behavior. It was demonstrated that a regular matrix of pillars may result in a super hydrophobic surface and induced a droplet to be a Cassie state. It was also observed droplets in Cassie regime even for moderate hydrophobicity or roughness of the patterned surface. We prepared devices with a local super hydrophobic zone defined by periodical array of pillars

(roughness 1.4). We expect that if we put a drop it will float without wetting the bottom but only the top of the pillars preventing the adsorption of molecules on the lateral walls.

In Figure 24 four devices with a drop on the top are shown. Actually the droplets borders lay on a flat region of the chip, since the patterned area is just 0.5mm in lateral size. Hence the visible contact angle is of the order of 100° and is the result of the C_4F_8 hydrophobic coating. We did not perform contact angle measurement on our pillar structures but similar structures in literature showed contact angles above 150° [13]. In order to prevent the evaporation of the drop, the samples are placed in a closed Petri dish pair and some water is added to saturate container with water vapor.

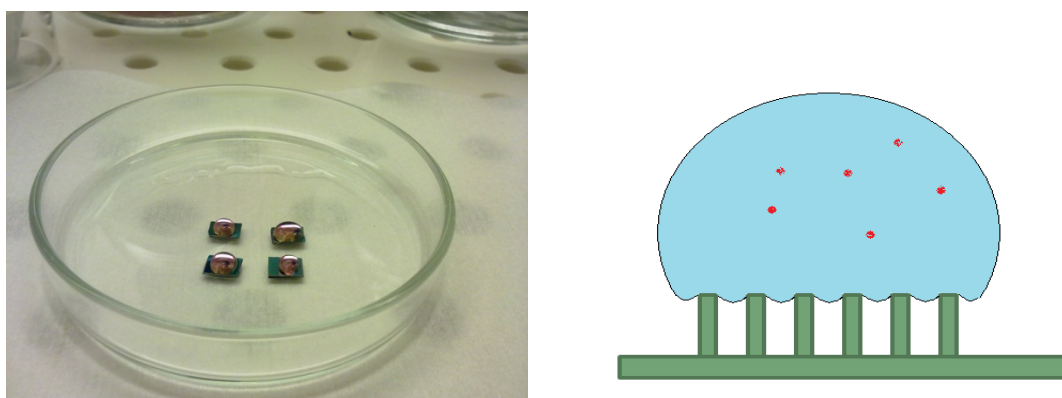


Figure 24. Four super hydrophobic devices with a drop on the top.

To verify that with this geometry only the top of the pillars are wet by the solution, we used droplets containing silicon micro beads (the diameter is $0.9 \mu\text{m}$) on a hydrophobic device and on an isolated pillars. The images below, obtained after drying the samples, show that, in the first configuration, the spheres got in touch only with the top of the pillar where they were captured via electrostatic interactions. Here we can distinguish groups with one, two or more spheres, while no spheres are found on the bottom or on the pillar sides. Outside the squared corral, the whole surface was wetted by the solution and a huge number of spheres are present. On the other samples, the spheres are on the top, on the sides of the pillar and mostly on the bottom substrate, a clear indication that the whole sample was wetted. We expect that molecules would behave in

the same way and we think that this technique would reduce further the influence of the aspecific adsorption on the pillars.

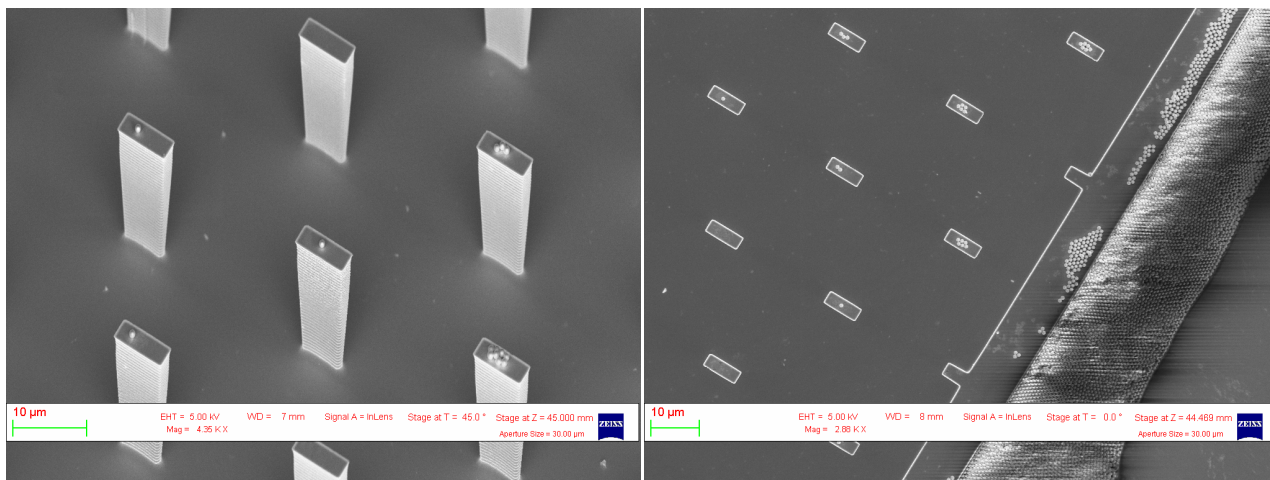


Figure 25. SEM images of a super hydrophobic devices.

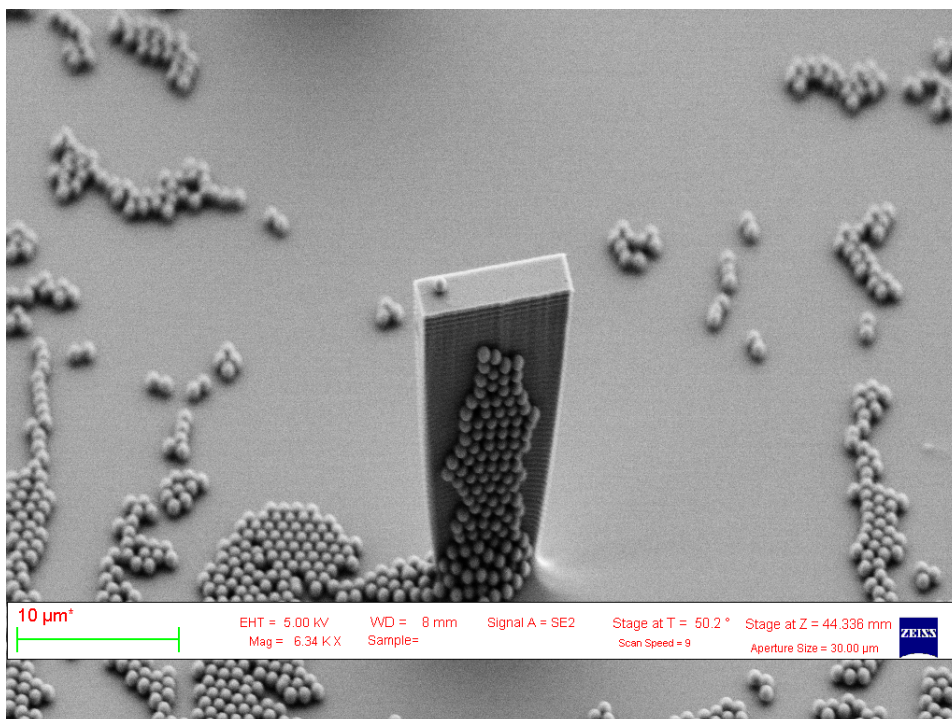


Figure 26. SEM image of a non hydrophobic device.

2.7 Reference

- [1] Y. T. Yang, C. Callegari, X. L. Feng, K. L. Ekinici, e M. L. Roukes, "Zeptogram-Scale Nanomechanical Mass Sensing," *Nano Letters*, vol. 6, n°. 4, pagg. 583-586, Apr. 2006.
- [2] N. Lobontiu, *Dynamics of Microelectromechanical Systems*, 1° ed. Springer, 2007.
- [3] M. Godin et al., "Surface Stress, Kinetics, and Structure of Alkanethiol Self-Assembled Monolayers," *Langmuir*, vol. 20, n°. 17, pagg. 7090-7096, 2004.
- [4] B. Ilic, Y. Yang, K. Aubin, R. Reichenbach, S. Krylov, e H. G. Craighead, "Enumeration of DNA Molecules Bound to a Nanomechanical Oscillator," *Nano Letters*, vol. 5, n°. 5, pagg. 925-929, Mag. 2005.
- [5] Jensen K., K. Kim, e Zettl A., "An atomic-resolution nanomechanical mass sensor," *Nat Nano*, vol. 3, n°. 9, pagg. 533-537, 2008.
- [6] Naika K., Hanay M. S., Hiebert W. K., Feng X. L., e Roukes M. L., "Towards single-molecule nanomechanical mass spectrometry," *Nat Nano*, vol. 4, n°. 7, pagg. 445-450, Lug. 2009.
- [7] J. Kehrbusch, E. A. Ilin, M. Hullin, e E. Oesterschulze, "High frequency columnar silicon microresonators for mass detection," *Applied Physics Letters*, vol. 93, n°. 2, pag. 023102, 2008.
- [8] J. Kehrbusch, E. A. Ilin, P. Bozek, B. Radzio, e E. Oesterschulze, "High-frequency micromechanical columnar resonators," *Science and Technology of Advanced Materials*, vol. 10, n°. 3, pag. 034601, 2009.
- [9] J. Kehrbusch, P. Bozek, B. Radzio, E. Ilin, e E. Oesterschulze, "Columnar shaped microresonators for mass detection and gas analysis," *Microelectronic Engineering*, vol. 87, n°. 5, pagg. 817-820, Mag. .
- [10] M. Melli, A. Pozzato, e M. Lazzarino, "Inverted tapered pillars for mass sensing," *Microelectronic Engineering*, vol. 87, n°. 5, pagg. 730-733, Mag. .
- [11] M. Li, Tang H. X., e Roukes M. L., "Ultra-sensitive NEMS-based cantilevers for sensing, scanned probe and very high-frequency applications," *Nat Nano*, vol. 2, n°. 2, pagg. 114-120, Feb. 2007.
- [12] E. Gil-Santos et al., "Nanomechanical mass sensing and stiffness spectrometry based on two-dimensional vibrations of resonant nanowires," *Nat Nano*, vol. 5, n°. 9, pagg. 641-645, 2010.
- [13] A. Lafuma e D. Quere, "Superhydrophobic states," *Nat Mater*, vol. 2, n°. 7, pagg. 457-460, Lug. 2003.
- [14] R. Blossey, "Self-cleaning surfaces [mdash] virtual realities," *Nat Mater*, vol. 2, n°. 5, pagg. 301-306, Mag. 2003.

- [15] E. Martinez, K. Seunarine, H. Morgan, N. Gadegaard, C. D. W. Wilkinson, e M. O. Riehle, "Superhydrophobicity and Superhydrophilicity of Regular Nanopatterns," *Nano Letters*, vol. 5, n°. 10, pagg. 2097-2103, Ott. 2005.
- [16] W. Zhang e K. Turner, "Pressure-dependent damping characteristics of micro silicon beam resonators for different resonant modes," in *Proceedings of IEEE Sensors*, vol. 2005, pagg. 357-360, 2005.
- [17] A. H. Nayfeh e D. T. Mook, *Nonlinear Oscillations*. Wiley-VCH, 1995.
- [18] K. L. Ekinci, "Ultimate limits to inertial mass sensing based upon nanoelectromechanical systems," *Journal of Applied Physics*, vol. 95, n°. 5, pag. 2682, 2004.
- [19] J. Lee, F. Goericke, e W. King, "Temperature-dependent thermomechanical noise spectra of doped silicon microcantilevers," *Sensors and Actuators, A: Physical*, vol. 145, n°. 1, pagg. 37-43, 2008.
- [20] T. Burg et al., "Weighing of biomolecules, single cells and single nanoparticles in fluid," *Nature*, vol. 446, n°. 7139, pagg. 1066-1069, 2007.
- [21] D. L. Stokes e T. Vo-Dinh, "Development of an integrated single-fiber SERS sensor," *Sensors and Actuators B: Chemical*, vol. 69, n°. 1, pagg. 28-36, Set. 2000.
- [22] L. Nicu et al., "Resonating piezoelectric membranes for microelectromechanically based bioassay: Detection of streptavidin-gold nanoparticles interaction with biotinylated DNA," *Sensors and Actuators, B: Chemical*, vol. 110, n°. 1, pagg. 125-136, 2005.

Quantitative Study of Nucleic Acid Monolayers by Means of Pillar-Based Mass Sensors

3.1 Introduction

DNA based sensors play a very an important role both in molecular biology and in medical and pharmaceutical fields because they allow the investigation of the gene expression of cells giving information, for example, about cellular functions or genetic diseases [1-3]. Furthermore, they are also gaining importance as a base for DNA Directed Immobilization of Protein [4]. DNA detection is based on the hybridization of single strand oligonucleotides, called probe molecules, which are attached to a surface. Then, it appears clear that the characterization of density, quality and chemical composition is crucial for enhancing the performances of this kind of biochips. Nevertheless, in spite of the huge technological relevance, it can be recognized a lack of a complete understanding, that is essentially due to the complex nature of the interaction of the DNA chain with itself, with other DNA molecules and with the substrate.

A common strategy to tailor interfaces is to bind covalently alkanethiol derivatives of single strand DNA oligomers to a gold coated substrate. This process is a molecular self-assembly technique which uses the high affinity of gold with sulfur atoms.

The main studies about the kinetics, the equilibrium of adsorption and the hybridization were obtained by means of indirect techniques like X-ray photoemission spectroscopy and surface plasmon resonance [5], [6].

However, the question about how the film structure affects the hybridization process is not properly addressed in literature. While it is commonly accepted that the hybridization efficiency in “extended” self assembled monolayers of ssDNA decreases with the molecular density of the probes on the surface [6], the same agreement has not been reached when the monolayers are confined in nanometric structures. Using nanografting (a nanolithographic technique performed in liquid environment with an AFM tip [7]) it is possible to fabricate ssDNA micro- and nanostructures with well defined height and lateral size [8]. The hybridization causes an increase of height and a reduction of compressibility that can be monitored by AFM microscopy. In those systems, ssDNA

hybridization takes place even at high density [9]. Since there is an independent evidence that a nanografted monolayer patch is better ordered than a spontaneously adsorbed monolayer made with the same molecules [10], we are led to the (indirect) conclusion that it is the intrinsic lack of order (instead of the density) that is responsible for the lack of hybridization of maximum density SAMs.

In order to provide further experimental data for this problem we designed a novel approach for characterizing self assembled monolayer of ssDNA. We used the top surface of a pillar as substrate for molecular assembling so that the adsorption and the hybridization added mass to the pillar can be directly measured by monitoring the change in frequency of the resonator.

3.2 Material and Methods

The experiment consists in different steps, following the “dip and dry” approach:

1. Bare Silicon Pillar measurement of resonance frequency
2. Gold deposition
3. Measurement of frequency variation for calibration
4. Water dipping
5. Measurement of frequency variation
6. DNA functionalization
7. Measurement of frequency variation
8. Hybridization
9. Measurement of frequency variation

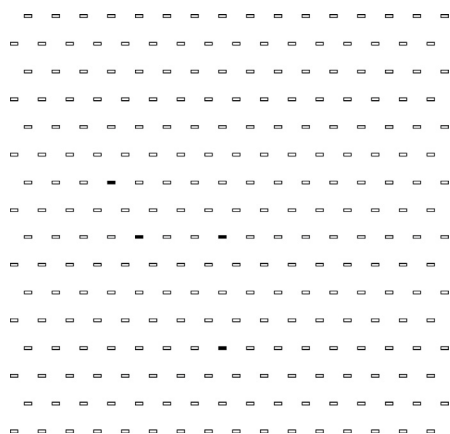


Figure 1. Layout of a device. The pillar colored with black was monitored in the experiment.

In this study we used the super hydrophobic configuration. The device is made of a regular hexagonal lattice of silicon pillars coated with a Teflon layer. This pattern makes a drop of liquid to float on the top of pillars and not to wet the bottom layer and the lateral walls. This has the big advantage to avoid molecular adsorption on the lateral faces. The matrix is made by 16 x 16 pillars. However, our setup limits the number of pillars that can be monitored in a reasonable time. Since we can measure a single pillar at the time, and a measure takes 15 minutes we decided to monitor four pillars. In Figure 1 we colored with black the

measured pillars. The range of resonance frequencies is from 4.5 MHz to 6 MHz. The Q factor is around 15000 in vacuum and the responsivity is around 30 Hz/fg. For gold coating we deposited first a layer of titanium (5 nm) and then a layer of gold (15 nm). The rate of deposition was kept low, 0.2 nm/sec, for increasing the uniformity of the metal layer. The mass added is 3.74 pg.

The preparation of ssDNA monolayer was done following the two-step protocol suggested by Tarlov and co-workers [5]. We prepared solutions with two different concentrations of DNA (1 μ M and 0.1 μ M). Drops of a specific solution are put on the pillar matrix of several chips for different incubation time (from 1 to 30 minutes). Subsequently these substrates were incubated for 1h in 1mM solutions of 6-mercapto-1-hexanol (MCH). MCH prevents unspecific interaction between ssDNA and gold assisting the vertical arrangement of DNA molecules. For hybridization a drop of solution with the complementary sequence at concentration of 1 μ M is used. The incubation time is 1 hour.

All oligonucleotides were purchased from Sigma-Genosys and where used without further purification. The sequences used in the study are:

DNA-Target	5'-TAG CCG ATT ACC AAG CCA AGC CAA GCC AAG TAG CCG ATTA-3'
DNA-Probe	HS-(CH ₂) ₆ -5'-TAAT CGG CTA CTT GGC TT G GCT TGG CTT GGT AAT CGG CTA-3'

The sequence is designed in order that self-dimerization and hairpin formation are avoided. For this reason the concentration of G or C base, which produce more stable base pair than AT, is limited to 50%. Higher concentration would increase the number of potential self-binding sites.

All the reagents were purchased from Sigma-Aldrich. The DNA solutions were prepared in TE buffer (1M NaCl, 10 mM Tris, 1mM EDTA, and pH 7.4) using MilliQ water (resistivity > 18 MΩ/cm). The solution of MCH was prepared in MilliQ water. Functionalization and hybridization reaction was performed in TE buffer

After the functionalization and hybridization steps, the samples are successively rinsed in TE buffer, 10 mM Phosphate Buffered Saline (PBS) with Tween 20 - 0.05% and MilliQ water in order to remove the aspecific DNA adsorption and residual salt from the devices.

3.3 Results

The first experiment consisted of two chips which were incubated with a 1 μM DNA solution for 1 minute and 30 minutes respectively. We observed that the resulting SAM properties were equivalent. They have the same coverage and the same hybridization efficiency, respectively $2.1 \cdot 10^{13} \text{ mol/cm}^2$ and 40 %. The relative frequency shifts of two selected pillars are shown in Figure 2.

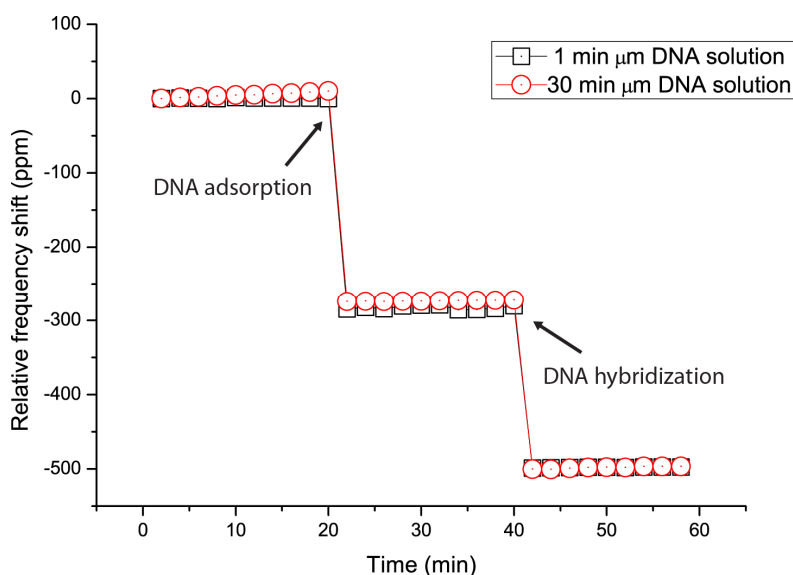


Figure 2. Relative Frequency shift. (1 μM DNA solution).

We are not able to monitor any kinetics because the saturation is reached in less than 1 minute. Indeed, the dip and dry process does not allow incubation time much shorter than 1 minute. This result is very interesting because it is in contrast with the values reported in previous works where

a maximum coverage was estimated to be $1.2 \cdot 10^{13} \text{ mol/cm}^2$ with hybridization rate around 10%. In order to understand better this discrepancy (especially on the hybridization efficiency), another experiment with lower concentration (100 nM) was performed always at 1, 3, 5, 10 and 30 minutes incubation time. In these conditions, samples behave differently, as it is shown in Figure 3, where the shifts for 1 and 30 minutes are shown for comparison.

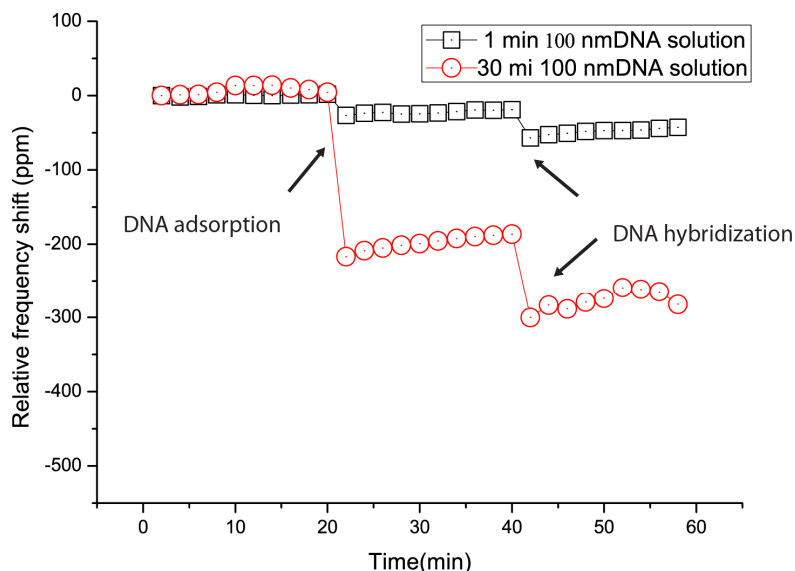


Figure 3. Relative Frequency shift. ($0.1 \mu\text{M}$ DNA solution).

After 1 minute a low density DNA SAM was produced. The coverage is $1.6 \cdot 10^{12} \text{ mol/cm}^2$. At this density the SAM is completely hybridized and presents extra contribution due to aspecific adsorption which is not removed by the rinsing. Instead, after 30 minutes a high density SAM ($1.4 \cdot 10^{13} \text{ mol/cm}^2$) with a hybridization rate of 46% is formed. The rest of the data is summarized in the following table:

Incubation Time (min)	Density (10^{12} mol/cm^2)	Hybrid. Rate (%)	Norm. Hybrid. Rate (%)
1	1.60	140	100
3	4.82	112	98
5	5.91	84	73
10	8.06	75	67
30	14.0	46	41

The error on the measured frequency is around 50 Hz which gives an uncertainty in density of $1 \cdot 10^{12} \text{ mol/cm}^2$. However from the first data is possible to extrapolate the value of the aspecific adsorption assuming a hybridization of 100%. This value can be used to renormalize the other data by subtracting the fixed amount of the unspecific adsorbed mass, around 3 fg, which we suppose to be the same for all experiments. The normalized values are given in the Figure 4.

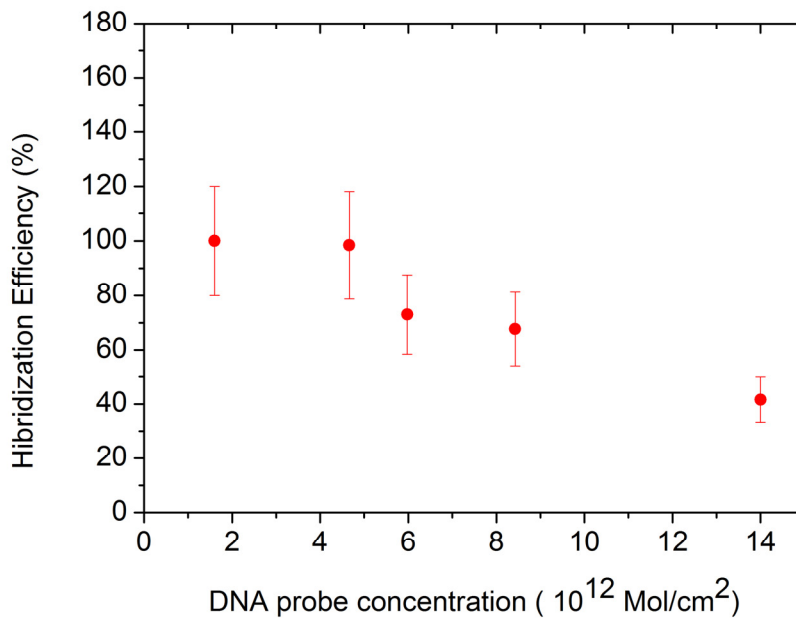


Figure 4. Hybridization efficiency vs. DNA probe concentration.

3.4 Discussion

The adsorption and hybridization kinetics [11] are often described using a Langmuir isotherm model where the variation in time of the fractional coverage is given by:

$$\frac{d\theta}{dt} = c \cdot k_a(1 - \theta) - k_d\theta$$

where the velocity of adsorption is proportional to the concentration of adsorbing molecules c , to the rate of adsorption k_a and to unfilled adsorption site. The velocity of desorption is proportional to the rate of desorption k_d and to coverage. The solution of the differential equation gives:

$$\theta(t) = \theta_{eq}(1 - e^{-kt})$$

where θ_{eq} is the coverage at equilibrium, k is the rate of layer formation and t is the adsorption time.

$$\theta_{eq} = \frac{c}{c + \frac{k_d}{k_a}}$$

$$k = c \cdot k_a + k_d$$

However this model is a first order approximation and neglects some physical considerations. Georgiadis et al. developed a model by including the dependence of adsorption by the molecular flux which is regulated by the diffusive mass transport through the solution [12]. This model, called adsorption/desorption/diffusion (ADD) takes into account the fact that near the interface liquid – substrate the molecular concentration is not constant but it is depleted by adsorption. They suggested implementing the Langmuir adsorption /desorption model with a time-dependent flux using Fick's law for mass transport.

$$\frac{d\theta}{dt} = J(t)(1 - \theta) - k_d\theta$$

$$J(t) = -D \left. \frac{\partial c(x, t)}{\partial x} \right|_{\lim_{x \rightarrow 0}}$$

Here, $c \cdot k_a$ is substituted by the time dependent flux of molecules onto the substrate, D is the diffusion constant. The functional dependence of concentration is actually obtained recursively by data interpolation. Figure 5 shows a comparison among different model of HS-C6-ssDNA adsorption kinetics

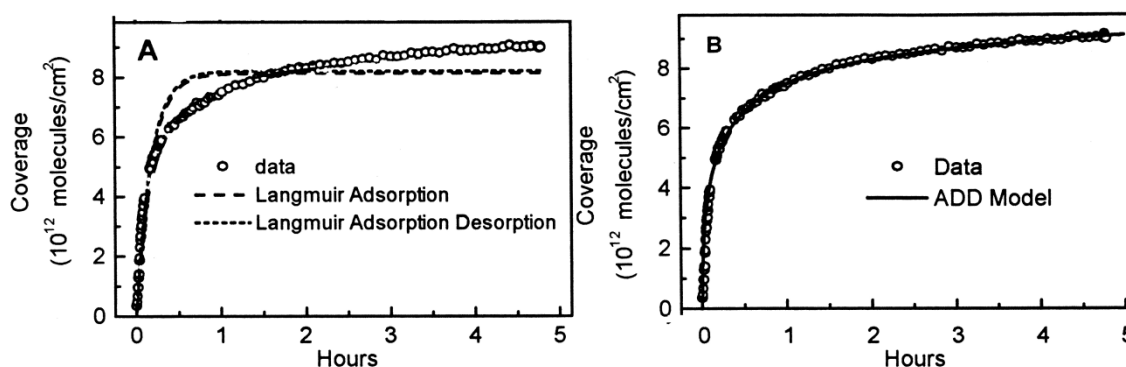


Figure 5. A comparison among different model of HS-C6-ssDNA adsorption kinetics (readapted from [12])

Figure 5 shows that the standard Langmuir isotherm (with and without the desorption correction) is too fast and is not able to fit adequately the experimental data giving wrong rate constant and equilibrium coverage. But, the ADD model fits extremely well the data proving that the assumption that the absorption, after the initial stage, is limited by the diffusion of the adsorbed molecules in solution is correct. However, the time dependence of the diffusion-limited concentration at the surface is extremely difficult to model. An alternative approach of the slowdown of the absorption rate is the so called diffusion limited adsorption Langmuir. The time dependent coverage is given by:

$$\theta = \theta_{eq}(1 - e^{-R\sqrt{t}})$$

where R is the growth rate parameter which depends on the concentration and on the diffusion constant of the molecules in solution. Behind this equation there is the well known result of the Brownian motion theory where the root mean square displacement after time t is $\sqrt{2Dt}$.

In our experiments the kinetics is much faster than the one reported in previous work. The origin of this disagreement is due to geometry of the substrate. In fact, as it has just described, the kinetics is limited by the diffusion of molecules, especially in the low concentration regime, typical of biomolecular experiments. The pillar detection offers a different geometry respect to other experimental approaches. Indeed, the advantage of pillars is that they allow the measurements of the adsorbed molecular mass on few micron squared surface, while, in order to apply other surface sensitive techniques, such as SPR or XPS, large areas of the order of 1mm squared are needed. From the diffusion point of view the latter can be treated as infinite planes, while on micropillars a 3-d diffusion behavior can play a major role. In Figure 6 it is sketched the two different regimes.

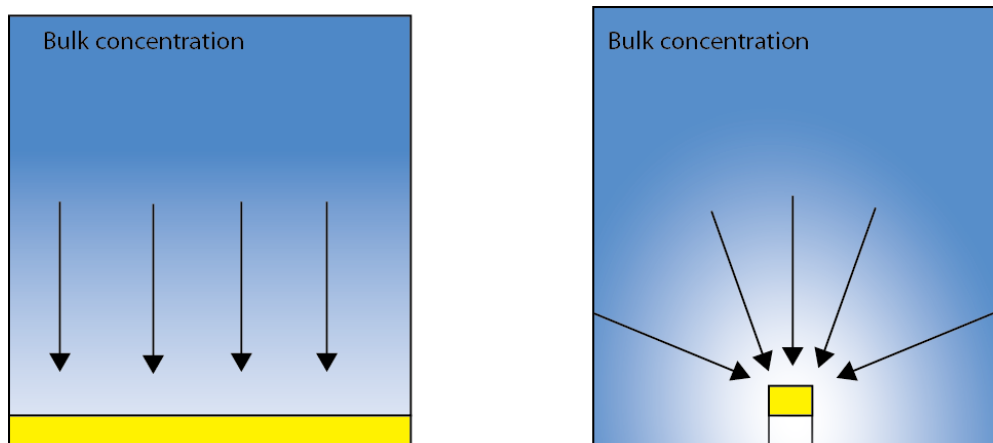


Figure 6. Different diffusion geometries. The color gradient represents the concentration variation near the surface and the arrows the diffusion paths of the molecules.

On average in flat substrate the number of molecules which can reach the substrate will be proportional to the vertical column above the absorption site. Instead in the pillar geometry, also molecules coming from different directions can reach the adsorption site because they are not trapped by near sites since the thiol-gold offers a high sticking coefficient and a low desorption rate. The overall result is the increased flux and also the kinetics it is faster.

The saturation coverage for this concentration is $2.1 \cdot 10^{13} \text{ mol/cm}^2$ and it is already reached for the smaller exposure time experimentally available. In order to prove this model in Figure 7 different fit models are performed:

1. Green curve. A Langmuir adsorption-desorption
2. Blue curve. A Langmuir adsorption-desorption without the last point
3. Black curve. Diffusion limited adsorption Langmuir
4. Red curve. A modified Langmuir

The last model is described by the following equation [13]:

$$\theta(t) = \theta_{eq} \left(1 - e^{-kt^n} \right)$$

The time dependency is modified by raising it to a power that is given by the fit. In the case $n=0.5$ the diffusion limited adsorption Langmuir is recovered.

A standard Langmuir curve does not fit the 100 nM data very well and if we neglect the last point, which is the most critical value, we obtain a very good fit (as we expected) but the saturation value is too low $9.5 \cdot 10^{12} \text{ mol/cm}^2$. Also a diffusion limited adsorption Langmuir curve fits the data well but provides a saturation value $9.5 \cdot 10^{14}$ that is sterically forbidden. On the contrary, the last model gives an excellent fit and it is meaningful from a physical point of view.

The saturation value is $1.83 \cdot 10^{13} \text{ mol/cm}^2$ much less than that one obtained using $1 \mu\text{M}$ concentration as expected from the standard Langmuir model, when the concentration is comparable to the equilibrium constant. This proves that desorption cannot be neglected in low concentration regimes in contrast with high concentration regimes previously reported [14]. The second and even more interesting result is that the exponential of the time dependence is 0.73 which is less than 1 (Langmuir model) but greater than 0.5 (diffusion limited adsorption Langmuir). This suggests that the kinetics is still influenced by diffusion/depletion but not as effectively as in the case of adsorption on extended surface. However, in order to strengthen this interpretation, it is necessary to develop a model to interpret the k parameter in terms of physical quantities like the concentration, diffusion constant or the binding energy of gold-sulfur, and in terms of the specific geometry of the system.

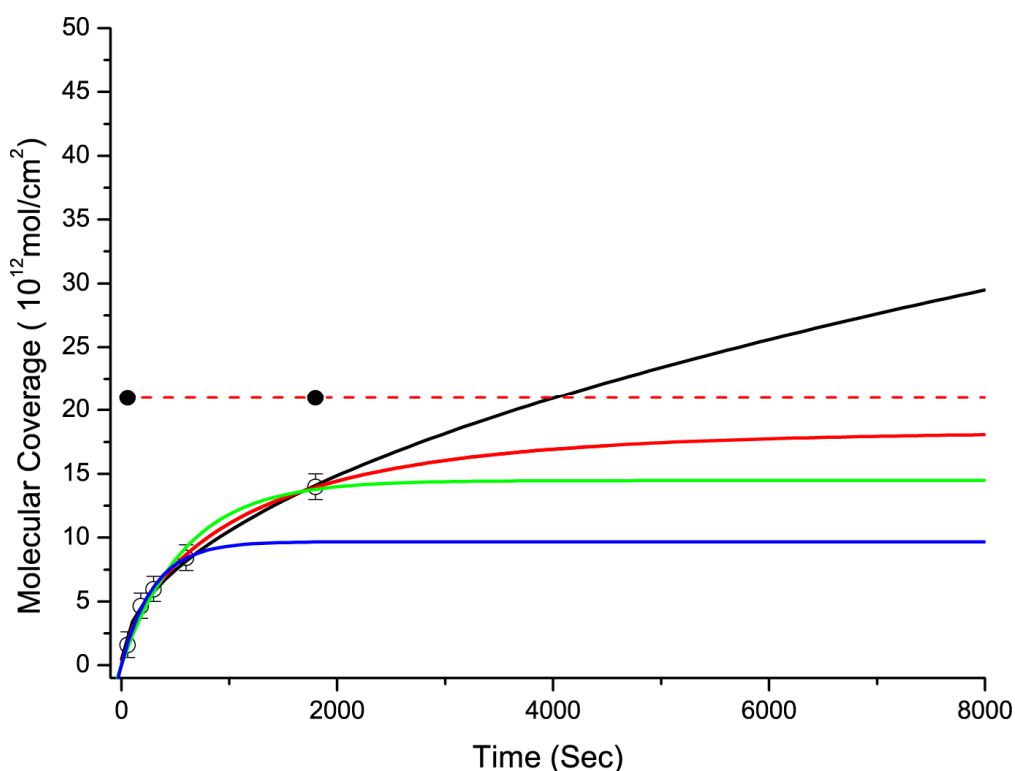


Figure 8. Comparison of the different curves given by the fit. The full black circles are the value of the $1 \mu\text{M}$ experiment.

The second result that has to be discussed is the increase of the hybridization efficiency. As it was mentioned in the introduction of this chapter, the quality of the SAM (i.e. the order) can be more important than density. High hybridization at high density can be an indirect proof that the “accelerated” diffusive adsorption results in more ordered SAM. In a virtually infinite surface, the molecules impinge on the surface at a lower rate and can non-specifically adsorb, laying down on the surface rather than standing up. If, as in the case of a small surface, the molecules impinge at a higher rate until the surface is nearly saturated the molecules do not have time to lie down and the SAM results more ordered. The same argument holds for the nanografting case. Here alkanethiol SAM is replaced locally by a ssDNA SAM by the mechanical action of an AFM tip. The SAM formation is very local (few nm^2 at the time) and the surface portion experience a quasi infinite concentration.

3.5 Pillars as DNA Sensors

This technology can be used not only for studying the DNA film properties but also for developing new DNA sensors. A test to demonstrate the specific recognition of DNA molecules was performed. Two sample with a concentration of $6 \cdot 10^{12} \text{ mol/cm}^2$ were fabricated. One is incubated for 1 hours with the complementary strand whereas the second with a non complementary sequence. The Figure 9 shows clearly that the non complementary sequence do not stay attached

to the substrate. From the result of the previous paragraph we expect that a concentration down to 10 nM can be detected in reasonable time, with less than 100 μl of analyte. In the experiments presented in this chapter we use typically drops with a radius of 3 mm that corresponds to a volume

of 50 μl . In micro array technology the area of the spot is $10^4 \mu\text{m}^2$ and

there are almost 10^7 - 10^8 probe molecules. A single pillar has active area of $20 \mu\text{m}^2$ and 10^5 - 10^6

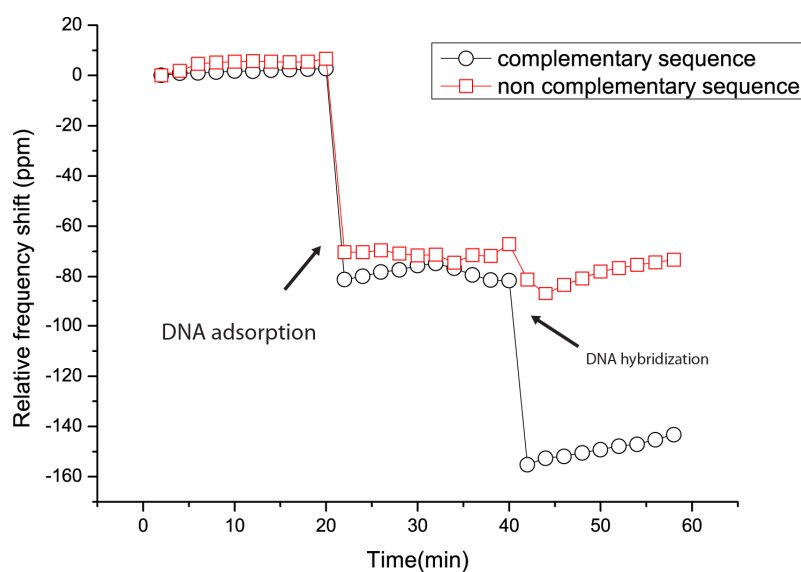


Figure 9. Graph shows the specific recognition of DNA molecules.

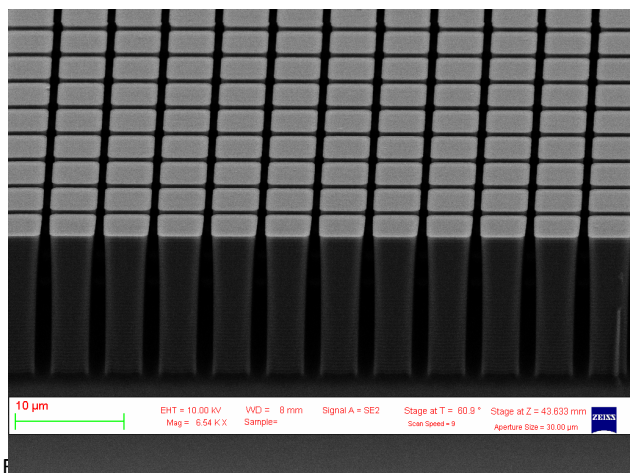


Figure 10. SEM image of a dense matrix of pillars.

amplification which may lead to biased results.

However at the present, the lack of parallel detection makes this device not competitive with the standard biochip technology. In fact, from one hand it is possible fabricate a sensor with thousands (even millions) of pillars (see Figure 10, actually with spot density much larger than the one of DNA array) but the detection would take days. We are presently thinking to introduce technology using a coherent fiber optics bundle that would do away the most of the listed difficulties. Another possibility would be to use a non optical detection, for example, the transduction scheme based on dielectric forces recently proposed by Unterreithmeier et al. [15].

3.6 References

- [1] P. S. Mischel, T. F. Cloughesy, e S. F. Nelson, "DNA-microarray analysis of brain cancer: molecular classification for therapy," *Nat Rev Neurosci*, vol. 5, n°. 10, pagg. 782-792, Ott. 2004.
- [2] V. Ambros, "The functions of animal microRNAs," *Nature*, vol. 431, n°. 7006, pagg. 350-355, 2004.
- [3] O. Barad et al., "MicroRNA expression detected by oligonucleotide microarrays: System establishment and expression profiling in human tissues," *Genome Research*, vol. 14, n°. 12, pagg. 2486 -2494, Dic. 2004.
- [4] C. Niemeyer, L. Boldt, B. Ceyhan, e D. Blohm, "DNA-directed immobilization: Efficient, reversible, and site-selective surface binding of proteins by means of covalent DNA-streptavidin conjugates," *Analytical Biochemistry*, vol. 268, n°. 1, pagg. 54-63, 1999.
- [5] T. M. Herne e M. J. Tarlov, "Characterization of DNA Probes Immobilized on Gold Surfaces," *Journal of the American Chemical Society*, vol. 119, n°. 38, pagg. 8916-8920, 1997.

molecules. Comparing these numbers, it is clear that the pillar detection has larger sensitivity. Moreover, the devices in this study were designed for the characterization of micron-sized DNA SAM and not for DNA sensors. Therefore, the geometry of the resonator can be further improved and reduced increasing the sensitivity that would give the great advantage to allow analysis of the gene expression profile in a small amount of sample without

- [6] A. W. Peterson, R. J. Heaton, e R. M. Georgiadis, "The effect of surface probe density on DNA hybridization," *Nucleic Acids Research*, vol. 29, n°. 24, pagg. 5163 -5168, Dic. 2001.
- [7] S. Xu e G. Liu, "Nanometer-Scale Fabrication by Simultaneous Nanoshaving and Molecular Self-Assembly," *Langmuir*, vol. 13, n°. 2, pagg. 127-129, Gen. 1997.
- [8] M. Liu, N. A. Amro, C. S. Chow, e G. Liu, "Production of Nanostructures of DNA on Surfaces," *Nano Letters*, vol. 2, n°. 8, pagg. 863-867, 2002.
- [9] E. Mirmomtaz et al., "Quantitative Study of the Effect of Coverage on the Hybridization Efficiency of Surface-Bound DNA Nanostructures," *Nano Letters*, vol. 8, n°. 12, pagg. 4134-4139, Dic. 2008.
- [10] Denis Scaini, "Electrical characterization of organic monolayers at the nanoscale: a differential scanning conductive tip AFM investigation," Doctoral Thesis, Università degli studi di Trieste, 2008.
- [11] F. Schreiber, "Structure and growth of self-assembling monolayers," *Progress in Surface Science*, vol. 65, n°. 5, pagg. 151-256, 2000.
- [12] R. Georgiadis, K. P. Peterlinz, e A. W. Peterson, "Quantitative Measurements and Modeling of Kinetics in Nucleic Acid Monolayer Films Using SPR Spectroscopy," *Journal of the American Chemical Society*, vol. 122, n°. 13, pagg. 3166-3173, Apr. 2000.
- [13] J. R. Rahn e R. B. Hallock, "Antibody Binding to Antigen-Coated Substrates Studied with Surface Plasmon Oscillations," *Langmuir*, vol. 11, n°. 2, pagg. 650-654, Feb. 1995.
- [14] A. Steel, R. Levicky, T. Herne, e M. Tarlov, "Immobilization of Nucleic Acids at Solid Surfaces: Effect of Oligonucleotide Length on Layer Assembly," *Biophysical Journal*, vol. 79, n°. 2, pagg. 975-981, Ago. 2000.
- [15] Q. P. Unterreithmeier, E. M. Weig, e J. P. Kotthaus, "Universal transduction scheme for nanomechanical systems based on dielectric forces," *Nature*, vol. 458, n°. 7241, pagg. 1001-1004, Apr. 2009.

Future Developments

In the previous chapters we have illustrated the potentiality and some interesting applications of the mechanical sensors based on a pillar geometry. This approach, however, gives the possibility to explore new concepts due to its intrinsic versatility and to the relative easiness of the integration with other techniques.

In this chapter we will introduce two new applications that we recently started to develop but are still in progress. The first is to develop a protein nanoarray based on our technique. The second is the combination of pillar oscillators and nanografting, an AFM-based nanolithography.

4.1 Application of Pillar Oscillators to Protein Nanoarray Development

The development of protein arrays is currently of great interest for biomedical diagnostics and life science applications [1]. Specific proteins can be a marker either of the presence or of the incubation of very serious diseases like cancers or degenerative disorders [2-4]. Tools that may be able to provide an early detection of a small amount of proteins will offer the possibility to start the treatment of the disease earlier with clear benefit for the patients. The simpler approach based on genomics (i.e. DNA analysis) is suitable for genetic diseases, however many factors, genetic, proteics and also epigenetic control the transcription in real life of the code written in the genome. RNA detection represents a step forward, since it provides the genes which are actually transcribed and also their relative amount [5], [6]. However RNA itself can be deactivated, and even when proteins are affectively synthesized, their malignant or positive function is determined by conformational changes [7], [8]. Only a direct detection of the protein involved in a disease, and, ideally, their structure, can provide us with a real signature of what is happening in a body. While DNA is present identically everywhere in a body, any given protein can be confined in particular portions of a tissue and only tiny amounts can be found in easily accessible organic samples, such as skin or blood [6]. The pillars platform offers a technological answer to the need of detection of small quantities of molecules.

In order to prove the capability of the pillar platform to detect small amount of proteins we explored the possibility to functionalize the pillar top surface using a technique which is known as DNA direct immobilization (DDI) introduced by Niemeyer in 1994 [9]. Following Niemeyer protocols, biomolecules are modified by a covalent attachment of an oligonucleotide chain and a surface is functionalized with SAMs with the complementary sequences. Through the high affinity of the Watson-Crick base pairing, the modified biomolecules are strongly bound to the substrate and in a single operation a DNA chip is transformed in a multiple protein, antigen or antibody nanoarray. Different kinds of detection strategies give subsequently the possibility to develop multiple biosensors. Recently Fouzia Bano and coworkers demonstrated the feasibility of this technique also for specific immobilization of proteins in nanometric patches and on their use for label-free detection of protein [10]. They monitored the binding of a specific antibody to the immobilized protein by measuring the variation of height on a very flat surface with an AFM. They reported, in particular, a high specificity of biomolecular recognition and the lack of nonspecific binding both in buffer and in human serum.

The measure of mass, given by the pillar approach, is alternative way to assess the protein recognition. However it is necessary to demonstrate that DDI is suitable for devices using pillars and proteins are compatible with the *dip and dry* scheme.

In a preliminary series of experiments, we first tested if DDI approach could functionalize the head of pillars with proteins without denaturizing them. So we prepared two sets of pillars, one functionalized with DNA-protein conjugates (streptavidin) and the other with DNA-protein conjugates + antibodies. In the second test the incubation with the antibodies was made immediately without drying the sample. The purpose of future experiments will be to understand the effects of drying and rewetting the proteins.

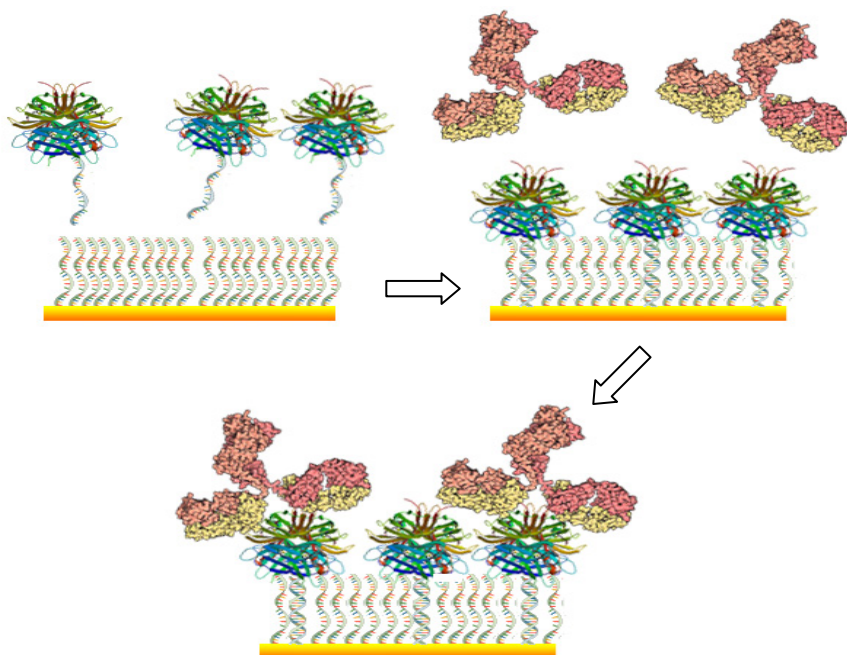


Figure 1. Representation of the DDI approach. A) ssDNA SAM with complementary DNA-protein conjugates. B) DNA-protein conjugates bound to DNA SAM with antibody. C) Mutual recognition of the protein and the antibody.

4.1.1 Materials

We used the same experimental approach used to determine the density of the SAM of DNA and its recombination efficiency. We prepared the samples following the protocol described by Bano et al. [10]. After the gold deposition and calibration steps, a DNA on the top of the pillars was prepared by putting a drop a solution of 100 nM of thiolated DNA (SH-(CH₂)₆-5'-TTCGGCTCATACTCTGACTGTA-3') in TE buffer for 30 minutes.

Then samples were incubated with drops of a solution with DNA-protein conjugate (500 nM) in PBS buffer (137 mM NaCl, 10 mM phosphate buffer, 2.7 mM KCL, purchased from Aldrich) for 1 hour. The protein used was the streptavidin (STV, mass = 52 KDa). After this step one set of pillars was rinsed (with PBS+tween20 and MilliQ water) and dried. The other one was rinsed and incubated with a drop of a solution with an antibody specific to the streptavidin (anti-STV-IgG, mass=100KDa) in PBS buffer at the concentration of 500 nm for one hour. After that it was washed and dried.

4.1.2 Results

The average shift induced by the adoption of the STV corresponds to a mass adsorption of about 35 fg ($\approx 4 \cdot 10^5$ molecules). The density is about $1.69 \cdot 10^{12}$ mol/cm² which provides the footprint of the area occupied by a single protein of about 60 nm² that is about 2.2 times larger than the footprint of a single STV molecule ($4.2 \times 4.2 \times 5.6$ nm³ i.e. 24 nm² in the most favorable case).

The average shift induced by the adoption of the STV + antibody corresponds to mass adsorption of about 42 fg. We can extrapolate the contribution of the antibody by subtracting the value obtained previously. This holds to the values of 7.5 fg which corresponds to $4.5 \cdot 10^4$ molecules. The density, $0.19 \cdot 10^{12}$ mol/cm², tells that the area occupied by an antibody is about 9 times larger than the one that is occupied by the protein and about 4.3 times larger than the footprint of a single IgG molecule ($14.5 \times 8.5 \times 4.0$ nm³ i.e. 124 nm² in the most favorable case). The incomplete coverage, suggested by these values can be due to the brevity of the incubation time (i.e. kinetic effects) or to an intrinsic steric effect. More experiments are necessary in order to clarify this aspect.

This preliminary set of experiments demonstrates that pillar detectors and DDI can be used for protein recognition. However there are some aspects that have to be developed and some properties that have to be demonstrated. We have to explore the effect of drying on protein tethered to a surface in order to reveal that the dip and dry is reliable with these molecules. Moreover, further studies are necessary to understand how far in term of sensitivity we can push the pillar approach for the recognition of proteins.

4.2 Nanografting

Atomic force microscopy (AFM) was invented for imaging surface with a very high vertical and lateral resolution. Few years later it was realized that AFM is also a very powerful tool for the modification of a surface, either of inorganic or organic nature [11]. Nanoindentation [12] and local anodic oxidation [13] are the main techniques applied to metallic, semiconducting and polymeric materials, while dip pen lithography [14] and nanografting [15] are mainly used for

organic films. Nanografting, and its simplified version, nanoshaving, are based on the local modification of a previously formed SAM. Nanoshaving is the mechanical removal of molecules induced by the tip. Starting with a SAM, it is possible to remove locally molecules in order to fabricate holes inside the SAM. The dimension of the holes varies from several microns to several nanometers. In 1997 Gang-yu Liu et al, by performing nanoshaving inside a solution with different molecules than those of the starting SAM, observed that the molecules in solution substituted the removed molecules thereby discovering nanografting. Therefore, nanografting is an AFM-based lithographic technique which permits to change the composition of a SAM over nanometric areas. The only limitation is that all molecules must have the same linker group with the substrate. Typically a gold flat substrate and thiolated molecules are used.

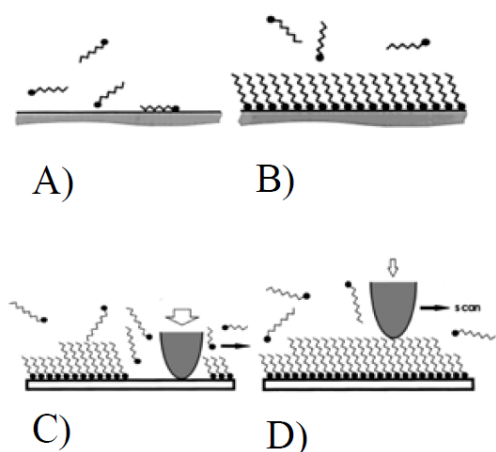


Figure 2. Schematic diagram of nanografting process:
 A) Gold surface exposed to a solution of alcohol and thiolated molecules.
 B) The molecules are adsorbed and self assemble
 C) At a force greater than the displacement threshold, the AFM tip displaces the adsorbates at the desired areas, and the thiol molecules in the contacting solution self-assemble onto the exposed gold sites.
 D) The nanopattern is imaged at a reduced imaging force.

We tried to combine nanografting with pillar sensing with a double motivation. From one hand pillars can characterize the nanografted patches in an absolute way which can hardly be done with standard techniques due to their low dimensions. On the other hand nanografting can provide a clever solution to the functionalization of different pillars with different molecules.

For this purpose there are two main technical problems: the flatness of the gold substrate and the positioning of the AFM tip on the pillar's top surface. Nanografting needs an ultra flat surface because the roughness of the surface must be lower by the one induced by the molecules so that the tip can "see" that the nanografting has occurred and where. In standard nanografting methods the gold substrate is prepared by evaporating gold on mica, bonding the top gold surface to a piece of rigid glass thereafter mechanically stripping the mica off. In this way an ultra flat gold surface is made (Ulman gold [16]). Unfortunately, this cannot be implemented for microstructured objects. E-beam evaporation of gold on silicon generates very rough surface even if a polished

silicon wafer is ultra flat because film formation is characterized by island growth. We solved this problem by evaporating first a layer of palladium (100 nm) and then a layer of gold (150 nm). In both evaporations the rate is kept very low (1 Å /sec). AFM analysis of the surface shows that the substrate is not quite like Ulman (best roughness 0.3 nm) gold but it good enough for nanografting (best roughness = 0.6 nm)

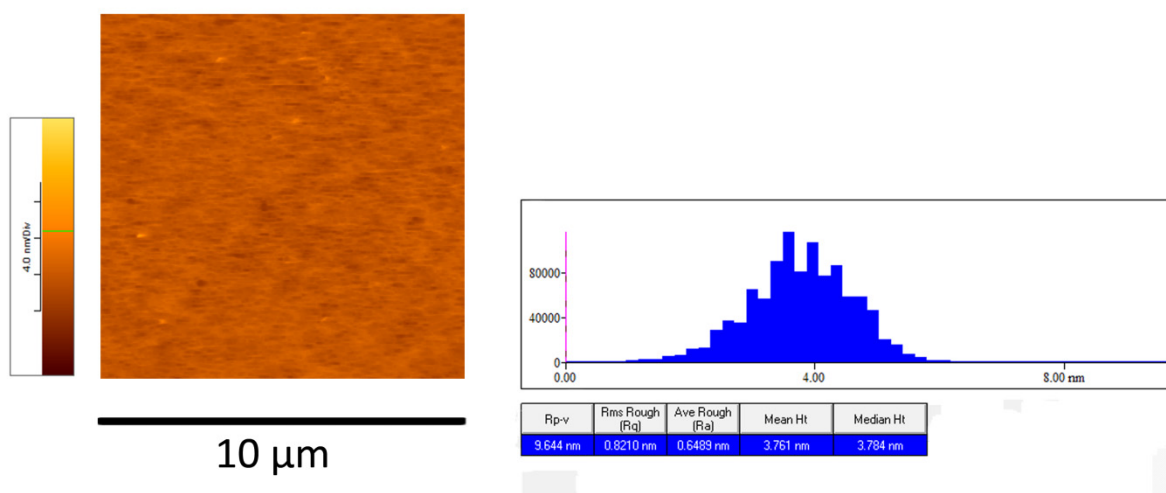


Figure 3. AFM image of the gold evaporated on silicon with a palladium as interfacial layer. The image shows an area of $10 \times 10 \mu\text{m}^2$. On the right the histogram of the topology shows average roughness of 6.5 Å.

As a test, we tried to nanograft ssDNA molecules inside a carpet of TOEG (Top Oligo Ethylene Glycol) molecules on a cantilever. We started with a cantilever in order to avoid in our first attempt the problem of the tip-pillar approach. We coated the sample with gold using the method described above. Then the coated cantilevers were functionalized by dipping over night the sample in a solution of TOEG in ethanol. Figure 4 shows that AFM and AFM 3D images of the end of a cantilever with $1 \times 1 \mu\text{m}^2$ and $0.5 \times 0.5 \mu\text{m}^2$ DNA-grafted patches.

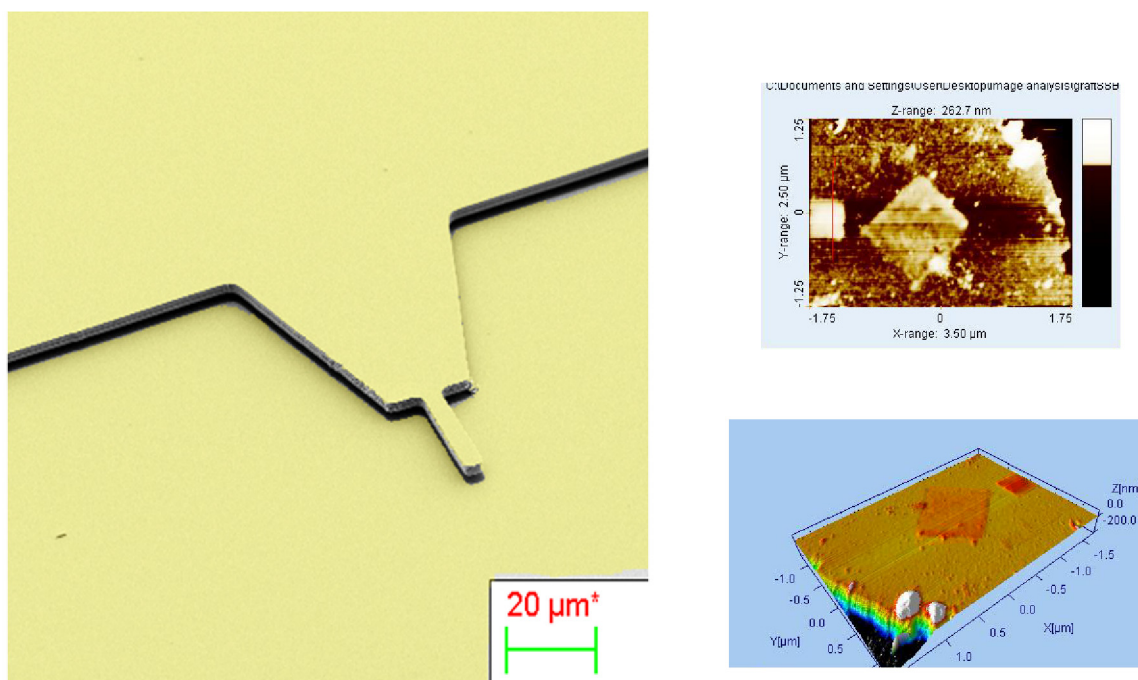


Figure 4. Left) SEM image of the cantilever device coated with gold. The image is colored to show the gold layer. Right) 2D and 3D images of a $1 \times 1 \mu\text{m}^2$ and $0.5 \times 0.5 \mu\text{m}^2$ DNA-grafted patches grafted near the end of the cantilever. The images show also the edge of the cantilever.

The problem of tip-pillar alignment is mainly due to mechanical limitations in the AFM hardware. First, the pillar area is smaller than the mechanical precision offered by commercial AFM during the tip-to-sample approach. Therefore the pillar top surface cannot be hit in a single attempt. Second, the pillar height exceeds the z range of most commercial AFM, therefore once landed with the tip on the substrate at the base of the pillar it is not possible to reach in a controlled way the top of the pillar. Any attempt to do that would break the AFM tip or the pillar. To address this issue a big triangle is fabricated near a pillar. In this way, since it is not difficult to land on a triangular mesa, it is much easier to approach laterally to the pillar surface without causing any damage. Figure 5 shows AFM images of a pillar top near the edge of the triangle. This image was made by using a very low scan speed and high gain.

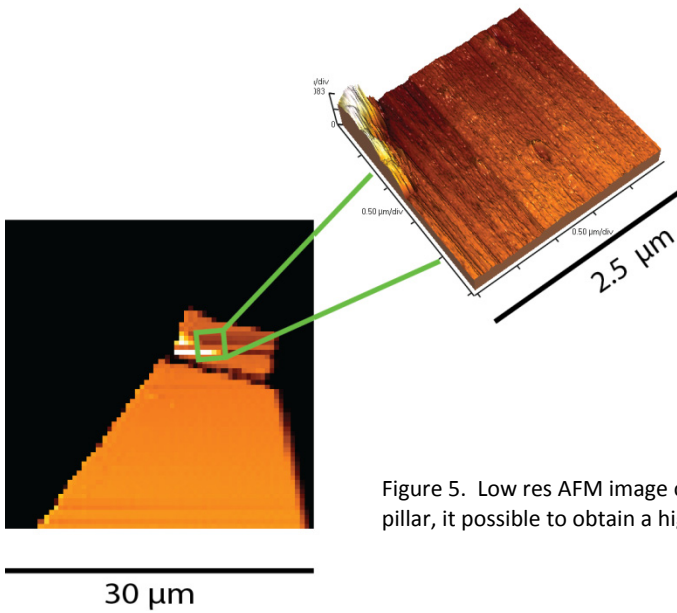


Figure 5. Low res AFM image of the pillar near the triangle. After the localization of the pillar, it is possible to obtain a high res AFM image of the pillar top surface (inset).

In this configuration the tip still touches laterally the borders of the pillars. To avoid this effect we drew some marker on the triangles. By means of a closed loop position control it is possible to move exactly the tip from the marker to the center of pillar head without crashing against the lateral wall.

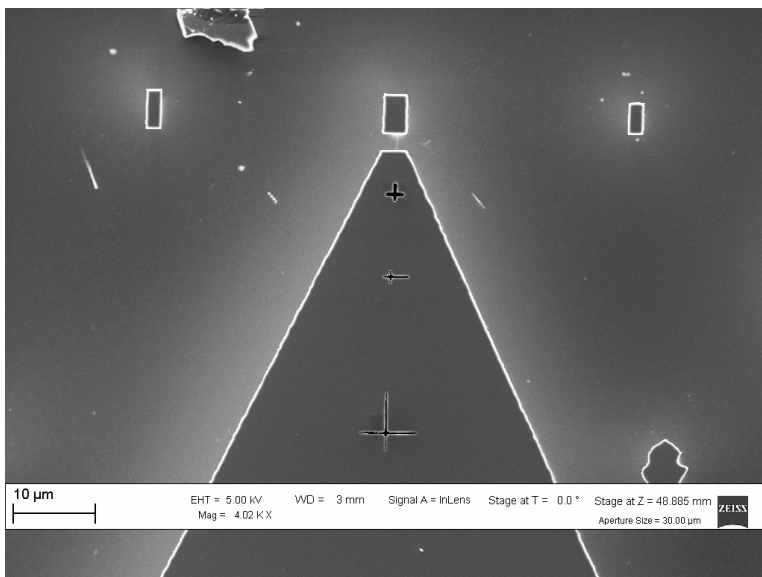


Figure 6. SEM image of a device with markers.

We believe that this design will allow to couple nanografting and pillar sensors. This new approach will give indications for some of the questions introduced in the third chapter. In particular, by quantifying the density of DNA nanografted patches we can understand better the roles of the order and of the density in hybridization efficiency of ssDNA molecules bound to a surface. Since there are at least three or four important issues connected to the correct measurement of DNA monolayer density, we believe that this problem shall deserve the attention of future investigators of this field. For instance, if the larger density of nanografted DNA patches will be confirmed by absolute measurements a very interesting question will be to explain why in a self-assembled monolayer of maximum density ($3 \cdot 10^{13}$ molecules per cm^2) the hybridization efficiency is limited to 10% [17] while in a nanografted patch of larger ($\times 1.5$) density the hybridization efficiency can reach more than 50% [18].

4.3 References

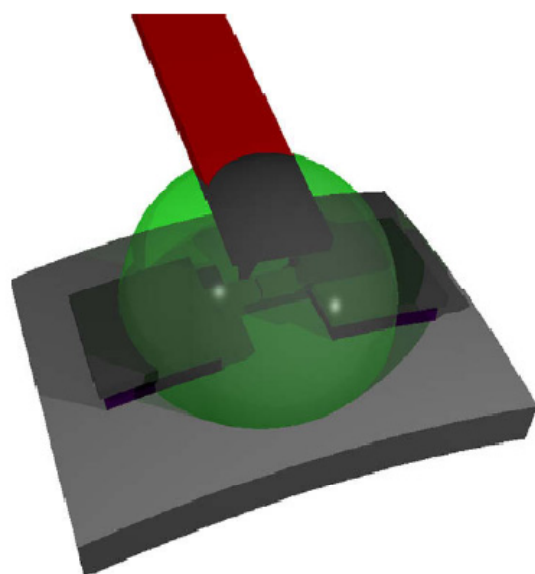
- [1] H. Zhu e M. Snyder, "Protein chip technology," *Current Opinion in Chemical Biology*, vol. 7, n°. 1, pagg. 55-63, Feb. 2003.
- [2] D. Slamon et al., "Studies of the HER-2/neu proto-oncogene in human breast and ovarian cancer," *Science*, vol. 244, n°. 4905, pagg. 707-712, 1989.
- [3] J. Hardy e D. J. Selkoe, "The Amyloid Hypothesis of Alzheimer's Disease: Progress and Problems on the Road to Therapeutics," *Science*, vol. 297, n°. 5580, pagg. 353-356, Lug. 2002.
- [4] D. J. Gelb, E. Oliver, e S. Gilman, "Diagnostic Criteria for Parkinson Disease," *Arch Neurol*, vol. 56, n°. 1, pagg. 33-39, Gen. 1999.
- [5] V. Ambros, "The functions of animal microRNAs," *Nature*, vol. 431, n°. 7006, pagg. 350-355, 2004.
- [6] J. Hesse et al., "RNA expression profiling at the single molecule level," *Genome Research*, vol. 16, n°. 8, pagg. 1041 -1045, 2006.
- [7] S. B. Prusiner, "Prions," *Proceedings of the National Academy of Sciences of the United States of America*, vol. 95, n°. 23, pagg. 13363 -13383, Nov. 1998.
- [8] S. B. Prusiner, "Novel Proteinaceous Infectious Particles Cause Scrapie," *Science*, vol. 216, n°. 4542, pagg. 136-144, Apr. 1982.
- [9] C. Niemeyer, L. Boldt, B. Ceyhan, e D. Blohm, "DNA-directed immobilization: Efficient, reversible, and site-selective surface binding of proteins by means of covalent DNA-streptavidin conjugates," *Analytical Biochemistry*, vol. 268, n°. 1, pagg. 54-63, 1999.
- [10] F. Bano et al., "Toward Multiprotein Nanoarrays Using Nanografting and DNA Directed Immobilization of Proteins," *Nano Letters*, vol. 9, n°. 7, pagg. 2614-2618, Lug. 2009.

- [11] L. G. Rosa e J. Liang, "Atomic force microscope nanolithography: dip-pen, nanoshaving, nanografting, tapping mode, electrochemical and thermal nanolithography," *Journal of Physics: Condensed Matter*, vol. 21, n°. 48, pag. 483001, 2009.
- [12] H. J. Mamin e D. Rugar, "Thermomechanical writing with an atomic force microscope tip," *Applied Physics Letters*, vol. 61, n°. 8, pag. 1003, 1992.
- [13] R. Held, T. Heinzel, P. Studerus, K. Ensslin, e M. Holland, "Semiconductor quantum point contact fabricated by lithography with an atomic force microscope," *Applied Physics Letters*, vol. 71, n°. 18, pag. 2689, 1997.
- [14] R. D. Piner, J. Zhu, F. Xu, S. Hong, e C. A. Mirkin, "'Dip-Pen' Nanolithography," *Science*, vol. 283, n°. 5402, pagg. 661-663, Gen. 1999.
- [15] S. Xu e G. Liu, "Nanometer-Scale Fabrication by Simultaneous Nanoshaving and Molecular Self-Assembly," *Langmuir*, vol. 13, n°. 2, pagg. 127-129, Gen. 1997.
- [16] A. Ulman, "Formation and Structure of Self-Assembled Monolayers," *Chemical Reviews*, vol. 96, n°. 4, pagg. 1533-1554, Gen. 1996.
- [17] A. W. Peterson, R. J. Heaton, e R. M. Georgiadis, "The effect of surface probe density on DNA hybridization," *Nucleic Acids Research*, vol. 29, n°. 24, pagg. 5163 -5168, Dic. 2001.
- [18] E. Mirmomtaz et al., "Quantitative Study of the Effect of Coverage on the Hybridization Efficiency of Surface-Bound DNA Nanostructures," *Nano Letters*, vol. 8, n°. 12, pagg. 4134-4139, Dic. 2008.

Chemical Functionalization of Atomically Flat Cantilever Surface

5.1 Introduction

Twin cantilever is an alternative approach in the field of mechanical oscillators recently introduced for symmetrical and asymmetrical system [1], [2]. Two or more mechanical resonators, (in the simplest case: cantilevers) are fabricated, close to each other but mechanically uncoupled. The dynamic behavior, in particular the resonance frequencies of each cantilever, is generally insensitive to the presence of neighbors. However, if any mechanical link is generated, as for instance by the sticking of one molecule to both resonators, they become coupled and their dynamic response is changed. The resonance frequency of the system is shifted, generally towards a higher frequency due to the increased stiffness, and the movement of one oscillator can induce a motion in a neighboring oscillator. So far only a finite element analysis of the device [1] and a proof of concept of the detection principle with carbon nanotube linkers has been provided [2] since a major technical difficulty still had to be tackled before detecting biologically relevant molecules: in order to link a molecule, such as a protein, in a twin cantilever device, two opposing surfaces have to be functionalized at a relative distance of less than 10 nm. However, thanks to the peculiar geometry of our devices, we can generate two atomically flat functionalized surfaces separated by a gap controllable with nanometric precision through the atomic matching between the two cleaved surfaces. A twin cantilever configuration can be fabricated by cleaving a bridge structure. The breaking generates two clean, atomically flat and extremely reactive surfaces [3]. When the cleavage is performed under ambient conditions, the two silicon surfaces oxidize instantaneously and become passivated with a thin layer of amorphous silicon oxide. If, instead, the sample is properly cleaved in a well controlled chemical environment the



local reactivity can be exploited for the formation of two locally functionalized surfaces which are intrinsically aligned.

5.2 Fabrication Procedure and Gap Tuning

We start from silicon on insulator (SOI) wafer composed of a 2.5 μm thick monocrystalline silicon layer with either $\langle 110 \rangle$ or $\langle 100 \rangle$ surface orientation, a 2 μm thick buried oxide layer and a 500 μm thick handle silicon wafer. We deposit, by electron beam evaporation, a protective 50 nm thick nickel layer on which the twin cantilever geometry is reproduced by standard optical lithography and subsequent wet etching of the Ni with a solution $\text{HNO}_3 : \text{CH}_3\text{COOH} : \text{H}_2\text{SO}_4$ in water. The remaining Ni structures are used as a mask for the etching of the silicon cantilever through an inductively coupled plasma reactive ion etching which allows the vertical walls to be defined through the whole thickness of the top silicon layer. Finally the oxide sacrificial layer is removed with a $\text{HF} : \text{NH}_4\text{F}$ wet etching and the sample is dried with a supercritical point dryer process, in order to avoid the stiction collapse of the suspended structure. At this stage the twin cantilevers are not yet formed and the structure has the form of a continuous bridge which is 500 μm

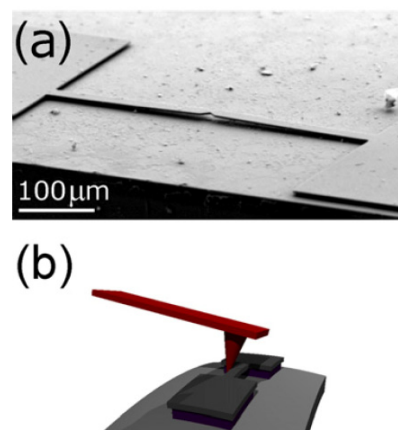


Figure 2. a) SEM image of a bridge prior the clearing. b) Schematic of the cleaving by mean of an AFM.

long, 20 μm wide and 2.5 μm thick and with a central region that is smoothly narrowed to a notch with a width of 10 μm (see the SEM image in Figure 2(a)). We then apply a lateral mechanical stress to the bridge at its weakest point, i.e. at the notch, with the help of a sharp tip such as that of an AFM (see the schematic illustration in Figure 2(b)). Since the bridge is monocrystalline, it cleaves along a crystallographic plane generating, in principle, two defect free, atomically flat surfaces. Since silicon cleaves along the $\langle 111 \rangle$ surface, one obtains a cleavage plane tilted at 55° with respect to the surface when starting with $\langle 100 \rangle$ wafers while vertical cleavage planes are obtained when starting with $\langle 110 \rangle$ wafers. If no residual stress is present in the topmost silicon layer, the two cleaved surfaces stay in contact with each other. In order to open the gap for molecular experimentation and to tune it with nanometric precision, we apply a bending moment

to the wafer, similar to break junction experiments [4], as described in [1]. In Figure 3, we report a series of SEM images, top view (a) and lateral view (b), of the gap at different bending values obtained by varying the bias applied to a piezo-actuator. These data are plotted as well in Figure 3(c), together with a linear fit that results in a gap tunability of 2.26 nm V^{-1} . The large offset of 42V needed to initially separate the two cantilevers originates from the residual compressive stress of the silicon top layer. From this measurement, the stress is estimated to be about 0.02%, in agreement with the SOI specification.

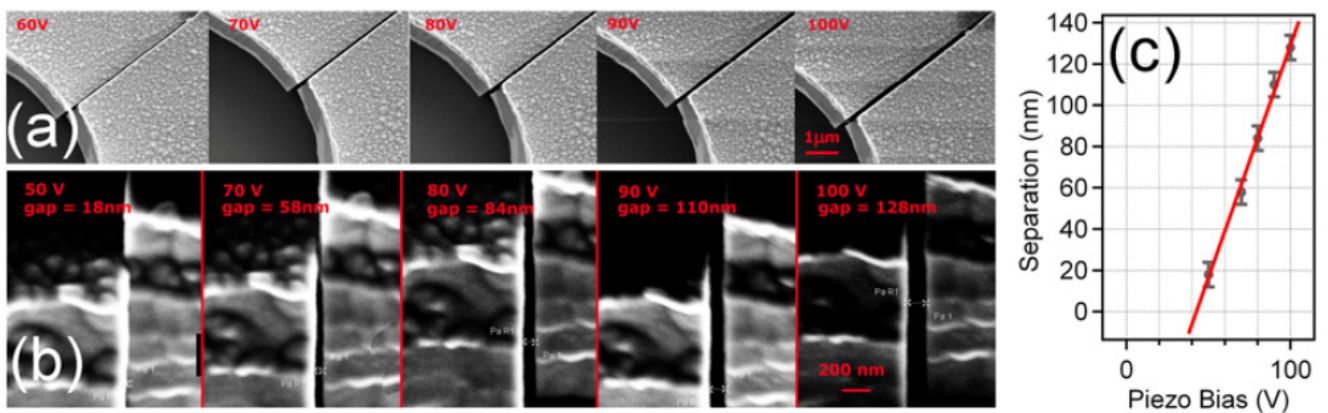


Figure 3. Sequence of SEM images of a twin cantilever gap at various voltages applied to the bending piezo-device. (a) top view—the images have been taken with 10° tilt in order to provide also a partial image of the side walls. (b) side view—images have taken with 70° tilt, which was the maximum allowed by our set-up. The gap can be tuned linearly from virtually zero to 128 nm, as indicated in the plot of the measured gap widths versus bending piezo-device bias (c). Substrate: $\langle 110 \rangle$ Si wafer leading to a vertical gap.

5.3 Chemical Functionalization

The fabrication process described above has a technologically extremely valuable peculiarity: the formation of the gap through the cleavage of the monocrystalline silicon exposes two ideally flat, clean and extremely reactive surfaces exactly matching each other. This ideal condition cannot be ensured by any other fabrication process such as those based on plasma etching or focused ion beam lithography, where edge roughness is typically in the range of several nanometers. In order to demonstrate the implementation of the mechanical assisted functionalization, we looked at surface functionalization reactions that could be effective on a clean, unreacted silicon surface, but that are hindered by the oxide layer that is present all over the remaining silicon surfaces,

thus exploiting the intrinsic alignment of the cleaved surfaces. Adsorption of simple unsaturated hydrocarbons on clean Si(100) surfaces has been extensively studied [5]. Two cycloaddition pathways are commonly accepted. In the [2 + 2] cycloaddition reaction the C=C double bond of a suitable organic molecule and a surface Si–Si dimer break to form a four member Si₂C₂ ring. In addition, molecules that contain at least two conjugated double bonds can instead link to silicon through a Diels-Adler [4 + 2] reaction. Cycloaddition reactions for compounds other than hydrocarbons have also been demonstrated. Ellison and Hamers, for instance, studied the adsorption of phenylisothiocyanate on a Si(001) surface and demonstrated that the reaction involves the formation of a Si₄NC ring [6]. In contrast to the large amount of data available for the (100) crystallographic plane of the silicon, fewer examples of cycloaddition processes are reported in the literature for Si(111) [7], [8]. The main differences lay in the nature of the silicon reconstructions present on the two clean, unreacted, surfaces: a symmetric one with the formation of surface Si–Si dimers in the case of Si(100)-(2 × 1) and a strongly asymmetric one with an adatom–rest atom pair in the case of Si(111)-(7 × 7). The Si–Si distance in the Si(100) dimers is 2.24 Å which better matches the C=C distance of 1.45 Å than the Si–Si distance of about 4.4 Å in Si(111). However, density functional calculations predict cycloaddition pathways for several unsaturated hydrocarbons in spite of this geometrical mismatch [9]. Finally it should be noted that all the experiments cited above had been performed on ultra high vacuum clean reconstructed surfaces and no data are available on freshly cleaved silicon surfaces.

In order to demonstrate the chemical functionalization upon cleaving of the twin cantilever we choose two different chemical compounds and two different cleaving strategies. As a first approach we used vinylferrocene (see Figure 4(a)). Vinylferrocene (VFC) is solid at room temperature and melts at 53 °C. The Fe atom trapped between the two aromatic rings can be easily monitored by several spectroscopic methods, whereas the vinylic double bond can be used to functionalize the

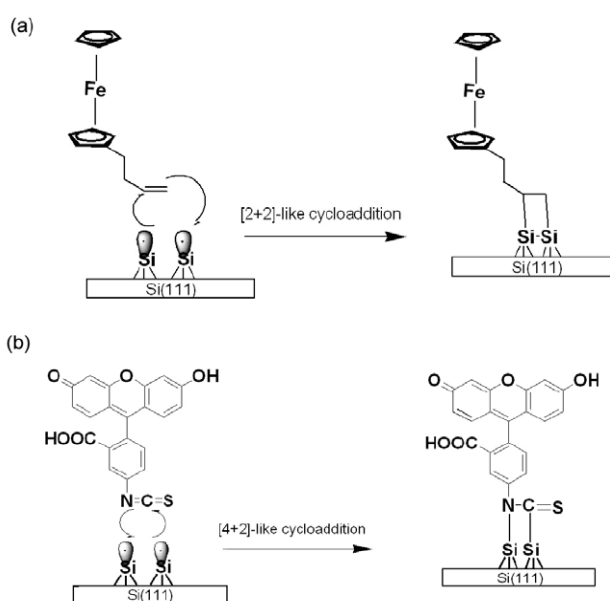


Figure 4. Reaction pathways on the unsaturated Si(111) surface that results from the cleavage with reactants such as vinylferrocene (a) and FITC (b).

silicon surface through a cycloaddition process. We mounted the sample in an atomic force microscope (AFM) equipped with a heating stage. We covered the bridge with solid VFC and we raised the temperature. Above the melting point the VFC changes its appearance into a transparent reddish liquid, allowing the silicon bridge to be viewed with the AFM optical microscope and the AFM tip to be aligned to the notch in the bridge. Upon cleaving, the two opposite Si(111) flat surfaces are immediately exposed to pure VFC. After a few minutes the sample is thoroughly rinsed in dichloromethane in order to remove all non-specifically adsorbed VFC. The quality of the functionalization was studied by energy dispersive x-ray (EDX) spectroscopy in a scanning electron microscope (SEM). The two cantilevers are first positioned in a way to allow an easy access to the functionalized surface, as displayed in Figure 5(a) for a device obtained from a $\langle 100 \rangle$ silicon layer and in Figure 5(b) for a device obtained from a $\langle 110 \rangle$ silicon layer. The cleavage planes are tilted with respect to the device surface by 55° , as shown in detail in Figure 5(c), and perpendicular, respectively. For each sample we collected one spectrum on the cleaved area and one on the top surface as indicated by the highlighted areas in figures 5(a) and (b). Two representative spectra taken with a beam electron energy of 10 keV and accumulation time of 10 min are shown in figures 5(d) and (e) for $\langle 100 \rangle$ and $\langle 110 \rangle$ surfaces respectively.

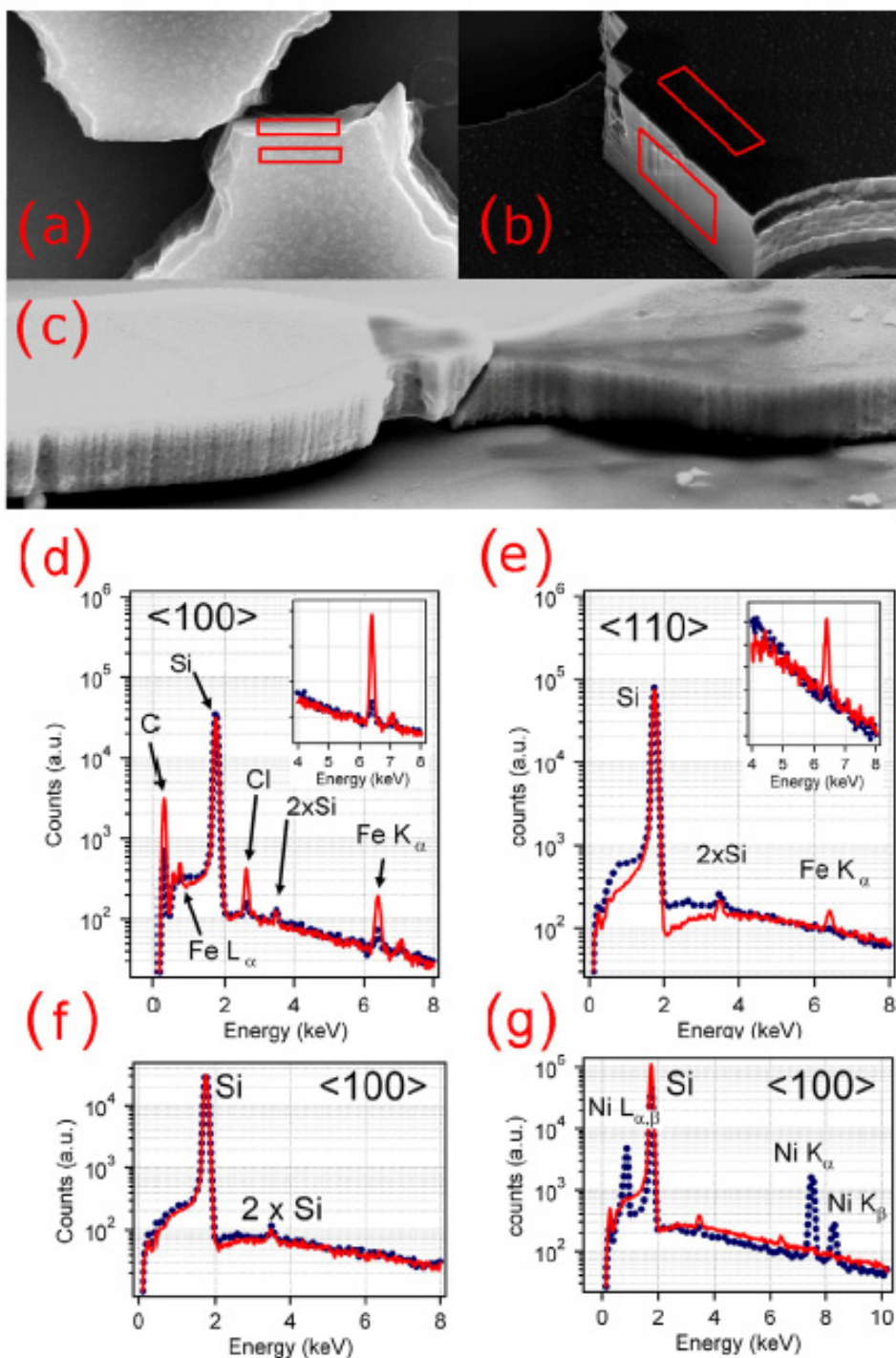


Figure 5. SEM images of twin cantilever structures from a $\langle 100 \rangle$ (a) and from a $\langle 110 \rangle$ Si wafer (b) resulting in an inclined, and a vertical gap, respectively, which are investigated in their chemical composition by EDX after removal of the opposite cantilever (see highlighted areas). (c) SEM lateral view of a $\langle 100 \rangle$ twin cantilever structure, showing the cleave occurring at 55° with respect to the surface. (d) EDX spectra for sample (a), (e) EDX spectra for sample (b): continuous lines refer to the reactive gap area obtained by the cleaving procedure and exposed to vinylferrocene, dotted lines refer to the unreactive native oxide. Insets highlight the ferrocene peak region. Further proof for the specificity of the procedure is the absence of functionalization in the gap obtained by cleaving in air prior to exposure to vinylferrocene (f) as well as a sample contaminated by Ni stemming from the fabrication process. The Ni signal does not show up on the cleaved surface (g).

In both spectra, the continuous line is related to the cleaved area and the dotted line is related to the top surface.

In spite of the very low surface sensitivity of the technique, we are able to observe a significant contribution of the VFC in the cleaved areas, while the VFC signal is negligible on the oxidized top surface of the cantilevers. Indeed, since EDX spectroscopy x-ray originates from a micron-thick region, while the functionalization layer is about 1 nm thick, the bulk Si peak is expected to be several orders of magnitude more intense than the VFC peak which is in agreement with our experimental observations. In the case of $\langle 100 \rangle$ surface, thanks to the particularly favorable surface orientation, the VFC peak is more intense than in the case of $\langle 110 \rangle$ surface and the Fe $L\alpha$ signal as well as the C $K\alpha$ signal are detected. Cl contamination from the rinsing procedure with dichloromethane is also present. An expansion of the Fe signal from figures 5(d) and (e), respectively, is displayed in the insets. In the case of the $\langle 110 \rangle$ sample, the VFC signal on the oxidized area is below the spectrum noise. In the case of $\langle 100 \rangle$ sample, the VFC signal is equal to 1/10 th of the full signal observed, which we attributed to electrons that scatter inside the silicon cantilever and eventually reach the cleaved side of the cantilever, producing the residual VFC signal. To exclude any non-specific VFC adhesion to the cantilever surface we cleaved the silicon bridge first in air, then we exposed it to VFC with the same procedure described above, and finally thoroughly rinsed it in dichloromethane. The spectra are displayed in figures 5(f) and (g). No trace of VFC has been detected either in the cleaved area or on the cantilever surface. The three extra peaks in figure 5(f) correspond to residual Ni on the cantilever surfaces due to the masking procedure in the fabrication process. As expected, Ni is observed only on the cantilever surface, but not on the cleaved area, which proves that the proposed procedure does not contaminate the cleaved areas. In a second approach we used fluorescein isothiocyanate (FITC), a common dye used in fluorescent microscopy (see figure 4(b)). FITC is soluble in water and other polar solvents, which are in the majority also good oxidizing agents, and therefore compete with FITC for the reaction with the freshly cleaved silicon surface. Therefore we dissolved the FITC in dimethyl sulfoxide (0.13 M), directly in a sealed chamber in which the sample and the cleaving mechanism were prealigned, in order to reduce the oxygen contamination of the solution and subsequent oxidation of the cleaved surfaces. After cleaving, the samples were rinsed in abundant methanol and water in order to remove all the FITC that was non-specifically absorbed on the surface. The samples were investigated by fluorescence optical microscopy, using a xenon lamp as a light source and a set of filters for fluorescein luminescence.

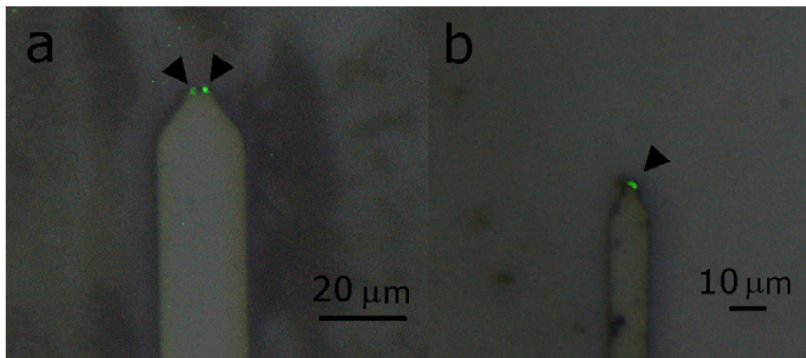


Figure 6. Overlay of bright field optical images of cantilevers from a $\langle 100 \rangle$ (a) and from a $\langle 110 \rangle$ Si wafer (b) with optical fluorescent images tuned on excitation and detection of fluorescein molecules. The opposite cantilevers have been mechanically removed to facilitate the imaging. The cantilevers were cleaved in a dimethylsulfoxide solution containing FITC, and then thoroughly rinsed in water. We observe FITC exclusively on the cleaved region of the cantilever (black arrows).

In order to facilitate the imaging, one of the two opposite cantilevers has been removed on purpose. In figures 6(a) and (b) we display two representative images of the obtained results for cantilevers fabricated from $\langle 100 \rangle$ and $\langle 110 \rangle$ wafer respectively. The images are the superimposition of bright field images of the sample, obtained without filters, and fluorescence images. For clarity, the fluorescence signals are indicated by arrows. We observed a fluorescence signal only in correspondence of the cleaved surfaces, while the rest of the cantilevers and the substrate surfaces do not show any fluorescence, indicating the absence of non-specific absorption. The fluorescence signal appears quite spotty, especially for the cantilever displayed in figure 6(a), rather than uniformly distributed along the cleaved area. This can be ascribed to the non-optimized concentration of the FITC solution. The size of the cleaved areas, on the other hand, is comparable with the optical resolution of the fluorescence microscopy, thus hindering a more detailed optimization of the parameters.

5.4 Cleaved Surface Analysis

The surface quality of the two facing surfaces generating by the cleavage process is, in principle, much better than any other surface produced through a technological process, such as those based on plasma etching or focused ion beam lithography where edge roughness is typically in the range of several nanometers. We investigated in detail the formation of the gap and the quality of the surface involved. In order to establish the actual absence of atomic steps on a cleaved surface, scanning probe microscopes offer the ideal resolution; unfortunately, in our case, the surfaces of

interest are vertical with respect to the optical surface of the sample and therefore they are not accessible to this kind of analysis. Therefore we fabricated by ICP and electron beam lithography several pillar structures of various size on a $\langle 111 \rangle$ silicon wafer and then we cleaved them close to the substrate in order to investigate the surfaces by AFM and SEM and then compare the information obtained using the two techniques. In Fig. 7a we show an SEM image of a cleaved surface showing several cleavage steps. In Fig. 7b we show an AFM image of the area highlighted by the square in Fig. 7a. In Fig. 7c we display the height profile obtained along the line drawn in Fig. 7b. Several steps ranging from 0.8 nm to 2.7 nm are observed, most of which can be clearly visualized also on the SEM image. We can conclude that SEM analysis can be used to assess the quality of cleaved surface down to atomic scale.

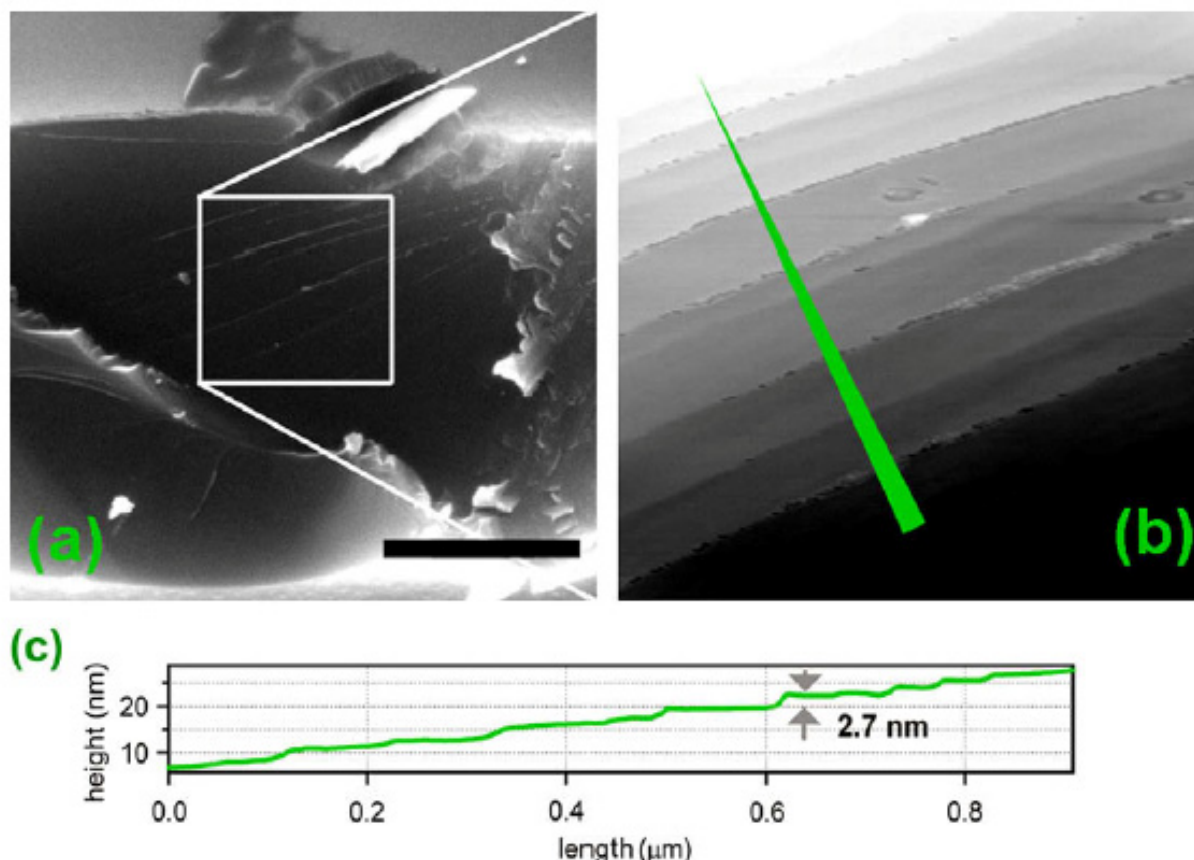


Figure 7. Comparison of SEM and AFM images of cleavage defects. (a) SEM image of a pillar $2 \times 4 \mu\text{m}^2$ mechanically cleaved along the (111). Some steps are clearly resolved and otherwise flat area. Scale bar $1 \mu\text{m}$. (b) AFM zoom on the $1 \times 1 \mu\text{m}^2$ area highlighted by the square in panel (a). Several flat terraces are observed. (c) Height profile along the green arrow in panel (b). All the steps are smaller than 3 nm.

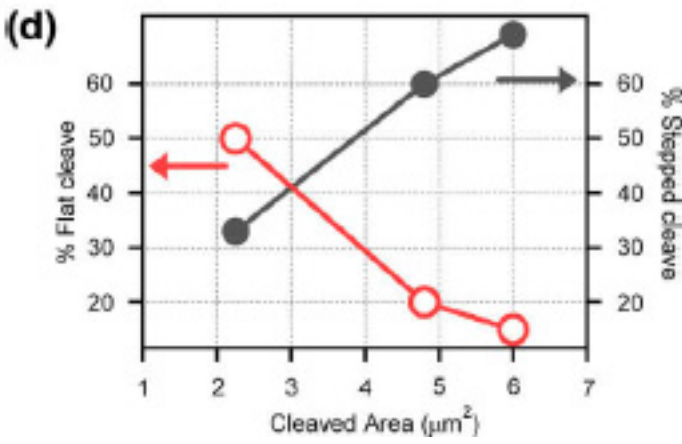
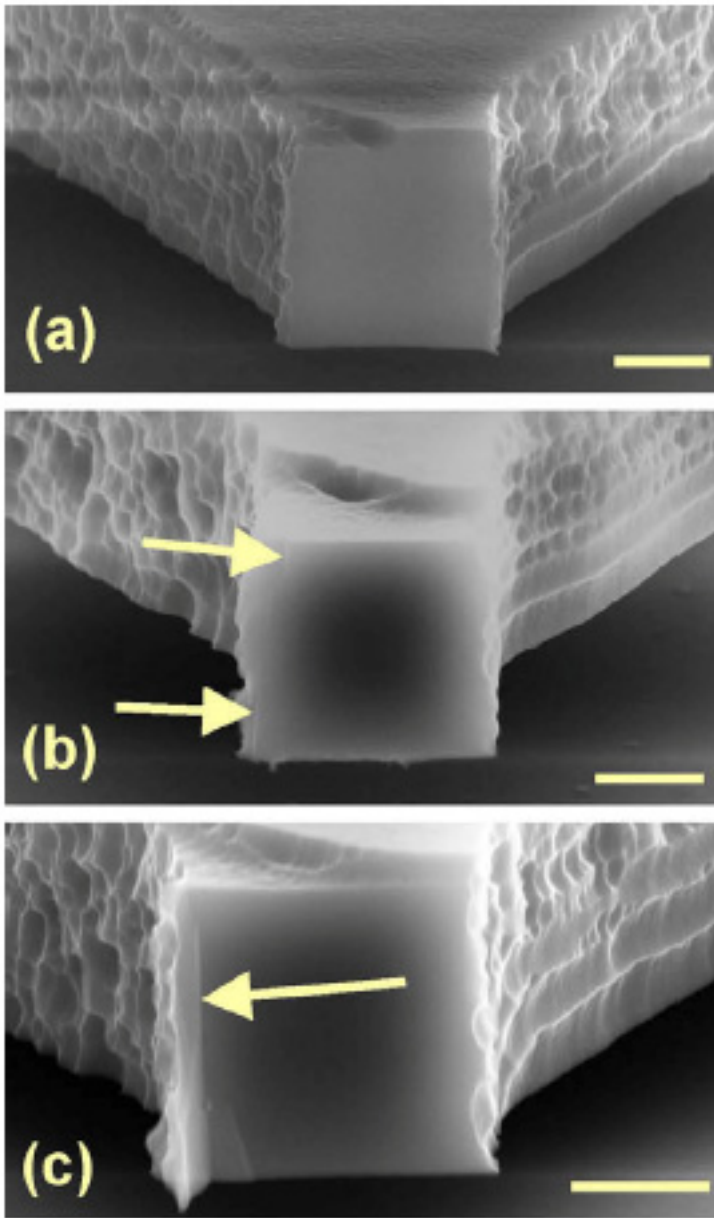


Figure 8. SEM images of cleaved cantilevers with section $2.2 \times 2.2 \mu\text{m}^2$ showing different surface quality. All scale bars are $1 \mu\text{m}$. (a) Defect free surface. (b) Surface with a shallow cleavage step indicated by the arrows. (c) Surface with a micrometer sized protrusion indicated by an arrow. (d) Plot of the percentage of defect free (open circles) and damaged (solid circles) cleavage as a function of cleavage area.

We fabricated some hundreds of bridges with three different notch size: $2.2 \times 3.0 \mu\text{m}^2$; $2.2 \times 2.2 \mu\text{m}^2$ and $1.5 \times 1.5 \mu\text{m}^2$. We then cleaved the bridges with the procedure described in the fabrication section. We removed one of the resulting cantilevers in order to facilitate the subsequent SEM imaging. We obtained three different typologies of surfaces illustrated in Fig. 8. In Fig. 8a we show a $2.2 \times 2.2 \mu\text{m}^2$ cleavage surface in which no defects are visible. In Fig. 8b we show an example of a surface with a bunch of steps indicated by the arrows. Finally in Fig. 8c we show a surface with a defected cleavage in which one side of the surface presents a large protrusion, indicated by the arrow. The latter geometry hinders the mutual movements of the two faces and represents a failure of a twin cantilever structure. It is worth to stress here the amazing difference between the surface roughness of the ICP etched walls and the cleaved surfaces. Fig. 8d displays the statistical analysis for the defect free surfaces (open symbols – red line) and the failed surfaces (full symbols – black line) plotted versus the surface area. At a $2.2 \times 2.2 \mu\text{m}^2$, 50% of the surfaces are free of defects, and following the trend sketched in Fig. 8d, a further reduction of the surface area would provide a majority of defect-free surfaces, opening the way for a possible engineering of this fabrication process. Finally it is worth to stress here that so far in literature the defect free cleavage procedures refer to solids whose area was in the few nm^2 range.

5.5 Spectroscopic Studies of the Mechanical Induced Functionalization

A deep characterization of the functionalization process that occurs during the cleaving in a reactive environment it is necessary in order to provide the evidence that our process results in an effective covalent bonding of the functional molecules with the silicon substrate. To this purpose we used a scanning electron microscope (SEM) (ZEISS Supra 40) equipped with energy dispersive X-ray spectroscopy (EDX) (EDAX) and synchrotron radiation photoemission spectroscopy performed at the BACH beamline at Elettra the Italian synchrotron radiation facility in Trieste [10].

In order to understand the chemical process that occurs at the silicon surface during the cleaving process, photoemission spectroscopy with energy resolution better than 100 meV is the best choice, for its surface sensitivity and its powerful discrimination between different chemical bond that can be energetically separated by only few hundreds of meV. On the other hand ultrasound assisted cleavage occurs only for micron-sized structures and a spatially resolved technique should be used, which excludes other spectroscopy such as infrared-based techniques. Unfortunately the same experimental apparatus seldom offers both high energy and spatial resolution. We chose to

sacrifice spatial resolution in favor of energy resolution for what concerns the photoemission experiment and to obtain spatially resolved information by means of SEM-EDX analysis.

The sample was designed in order to offer the maximum cleaved area to oxidized area ratio, therefore pillars structures with high density were fabricated, which resulted in a 1:4 ratio, as shown in fig 9 a and b. Silicon pillars were defined on a single crystal silicon (111) wafer by electron beam lithography and etched with inductively couple plasma (ICP) etching. A SEM image of a silicon pillar array is displayed in fig 9a. A detailed description of the fabrication procedure has been given the chapter 2. After pillar etching, Au was evaporated in the pillar area before cleaving in order to get a higher spectroscopic contrast. However, for geometrical reasons gold did not cover entirely the sample. The wafer were immersed in a sealed vial containing the reactive

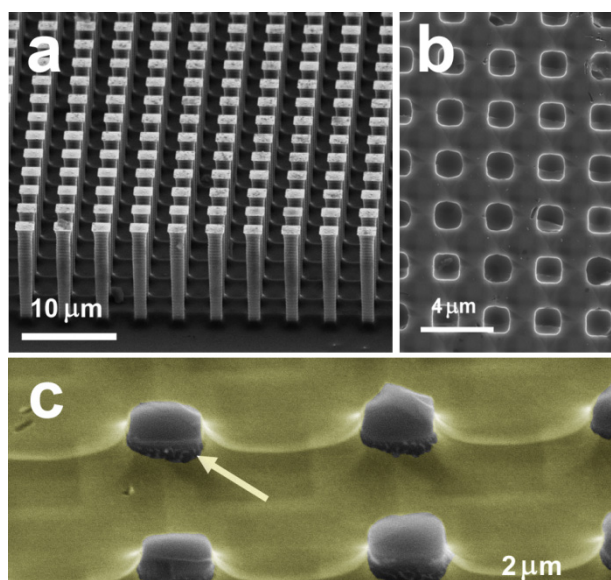


Figure 9.

(a) SEM image – 60o tilted view of an array of pillars before ultrasound cleavage. (b) SEM image - Top view of an array of pillars after cleaving. (c) SEM image – 60o tilted view of the same sample in (b). The gold covered areas are in false color (online version). Here at the base of the pillars, the portion of surface that is not cleaved nor covered by gold can be observed as a darker area as pointed by an arrow for an exemplificative pillar. Even though the tilt is not necessarily the same as in the photoemission experiment the relative contribution of cleaved silicon and oxidized silicon can be qualitatively estimated.

medium, which in the experiment described in this letter was 1H,1H,2H,2H-perfluorodecyl acrylate (PFA) (97%, Sigma Aldrich 474487). The vial was then flushed with pure nitrogen for one hour to remove any trace of moisture and oxygen that can react and passivate the silicon surface faster than PFA. Finally the sealed vial was immersed in commercial ultrasonic bath for 5 minute. The ultrasound creates small gas bubbles that explode causing the cleavage of the pillars at their base, along a $\langle 111 \rangle$ crystallographic plane, while keeping the vial sealed and the reactive medium clean. The treatment was effective on average on one sample over three. In the successful cases all the pillars were cleaved as shown in fig 9b, while in the negative cases a further exposure to ultrasounds, even for prolonged time was ineffective. We believe that this will depend strongly on the size and shape of

the wafer chip on which pillars are fabricated. Different chips may couple in different ways to the ultrasound resulting in dramatic change of the efficiency. However further investigations are

necessary to clarify this point. After cleavage, samples were rinsed in abundant methanol, immediately introduced in the experimental chamber of the BACH beamline and kept under ultra high vacuum condition until the beginning of the experiment.

As a result, after cleaving, the sample surface consisted of three main typologies: i. Clean, freshly cleaved, to-be-functionalized, <111> silicon surface. ii. Evaporated gold surface, (shown in false colors online in figure 9c on) on which organic molecules could physisorb unspecifically. iii. Silicon oxidized surface, as left from the ICP etching process, with carbon residues originated by the etching process. The latter region is indicated by an arrow in fig 9c and is situated at the base of the pillars. The patterned surface covered an area of $400 \times 400 \mu\text{m}^2$ and was determined by the maximum writing field of the EBL used. Two angular configurations were explored. At normal emission the photoemission is more bulk sensitive, and Si 2p spectrum was dominated by the silicon under the oxidized areas. At grazing emission the photoemission is more surface sensitive and bulk contribution from below the oxide was strongly reduced, however the geometric ratio was slightly worsened because of the non planar topography of the sample and contribution from the carbon contaminated and oxidized surface indicated by the arrow in fig 9c becomes more important.

Photoemission spectra were collected by illuminating the sample with photons at 250 eV and 340 eV, to maximize the photoemission cross-section for Si 2p and C 1s respectively. The photon beam was focused to a nominal beam waist of about $300 \times 20 \mu\text{m}^2$; however the photoemission signal generated by the beam tails extended over a much larger area. The gold evaporated on the pillar area was used both for finding the pillar position and to measure the photon energy using the Au 4f photoemission peaks.

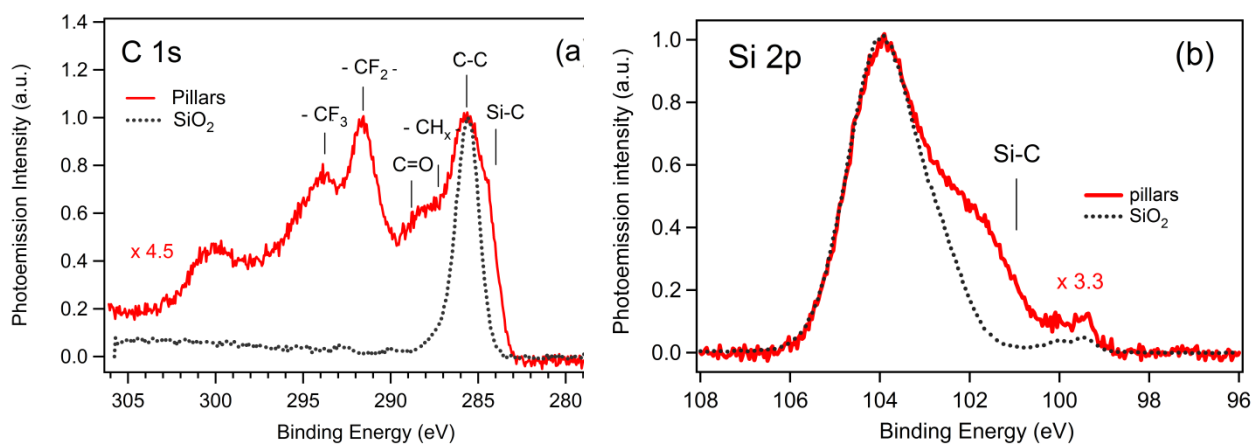


Figure 10.

(a) C 1s photoemission spectra collected in normal emission in the pillar area (red continuous curve – color online) and on the oxidized silicon area (black dotted curve). (b) Si 2p photoemission spectra collected in normal emission in the pillar area (red continuous curve – color online) and on the oxidized silicon area (black dotted curve). The maximum intensity has been normalized to 1 in both spectra.

In Figure 10 we display the photoemission spectra collected from the region with the cleaved pillar (red continuous lines) and from the silicon oxidized region close to the pillar region but far enough to avoid photoemission signal from the cleaved pillars and from the gold covered area (grey dotted lines). A linear background is subtracted from each spectrum and maxima are normalized to 1 for a better visual comparison. Figure 10a shows the photoemission spectra from the C 1s core level. These spectra have been acquired in the grazing emission geometry, which offers a higher surface sensitivity. The identification of the different bonding environment for PFA is in very good agreement with what published in literature [11]. We first observe that a clear signature originating from the PFA molecule [12] is present only in the pillar region. The ratio of the intensities of the CF_3 (one atom per molecule), CF_2 (7 atom per molecule) and C=O (one atom per molecule) which should be 1:7:1 for randomly oriented or physisorbed molecules [11], is instead about 5:20:1 and indicates that PFA molecules are intact and are anchored to the surface on the acrylic side and disposed vertically with respect of the surface with the CF_3 group in the outermost position. None of these peaks are observed on the silicon oxidized surface, meaning that physisorbed molecules have been efficiently removed by rinsing. The strong peak at a binding energy (BE) of 285.5 eV is observed on both areas, 4.5 times stronger on the silicon oxide area. We attribute this peak to amorphous carbon (C-C bond) left by the BOSCH process used to etch the pillar structures. The difference in intensity reflects the different portion of surface covered by this

amorphous layer, which corresponds to the full area on the silicon oxide and to roughly one fourth on the cleaved area, and the illumination geometry which is particularly sensitive to the non gold coated pillar sides. At lower BE we observed on the cleaved region a shoulder at about 283.5 eV. The presence of this shoulder is a general signature of the chemical reaction which occurs between carbon and silicon leading to the formation of a C-Si covalent bond. This reaction has been well characterized both in the case of organic molecules [13] and of carbon cluster [14] on clean silicon surface.

Figure 10b shows the photoemission spectra from the Si 2p core level, acquired in normal emission geometry, as the more bulk sensitivity allowed us to investigate the silicon-carbon interface buried under the PFA layer. The main peak at high BE present on both spectra originates from the silicon oxide, which terminates the non-cleaved areas. As expected, the intensity is larger on the non-patterned area by a factor 3.3. A small component from the bulk silicon is also visible around 99 eV BE in both spectra, with the typical spin-orbit splitting of 0.6 eV. Only the spectrum acquired in the region of the cleaved pillar shows a third feature, a shoulder at about 101 eV, that can be attributed to the formation of covalent Si-C bonds at the silicon surface as already observed for organic molecule and carbon clusters reacting on silicon surfaces [13], [14]. C 1s and the Si 2p spectra acquired in the cleaved area consistently indicate the formation of a C-Si at the pillar surface, and since the absence of thermal treatment rules out the possibility of a two step process (such as physisorption and subsequent thermal bonding formation), we conclude that the surfaces were functionalized through a 2+2 cycloaddition process.

In order to prove that the functionalization process occurred selectively on the silicon cleaved areas we further investigate the samples with a SEM microscope equipped with chemical analysis. The images thus acquired are displayed in Figure 1. In Figure 11a we show a secondary electron SEM image that provides a topographic description of the sample. The black areas are the cleaved regions: they do not show secondary electron signal because they are atomically flat and scatter electrons to a relatively low extent. In Figures 11b and 11c we show two images of the same region acquired at the X-ray energy corresponding to the K emission line of the fluorine and the M emission line of Au, respectively. The remarkable contrast observed together with the correspondence with the topographic image confirms the hypothesis that the cycloaddition process occurs only on the cleaved areas. In Figure 11d we display two X-ray spectra acquired in the middle of a cleaved area (red-light line) and on the adjacent region covered by gold (black-dark

line). On the cleaved area we observe significant contribution from carbon, oxygen and fluorine, and a large contribution from silicon, which is not surprising since EDX, contrary to photoemission spectroscopy, probes the sample at several microns in depth. All the peaks are present also on the gold area with different intensity except for the F peak that is absent. This finally proves that the functionalization happens only in the cleaved areas.

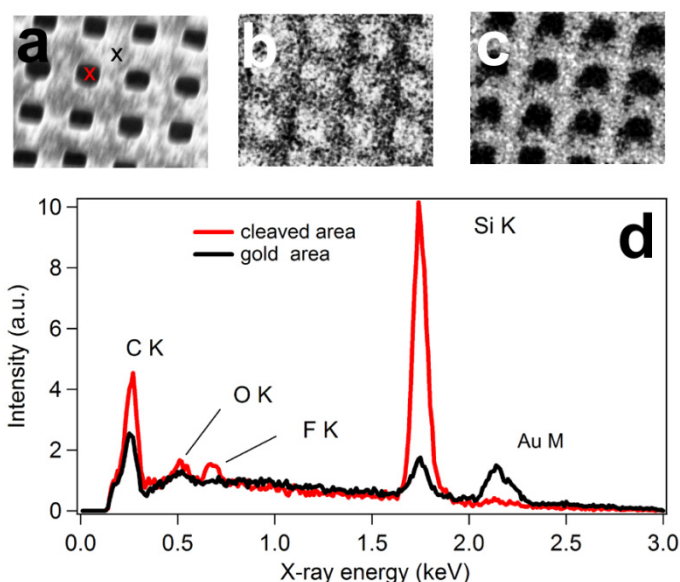


Figure 11

Energy dispersive X-ray analysis of the cleaved pillars. (a) Secondary electron image. Red cross and black cross indicate the location from where the spectra displayed in (d) were acquired. (b) F k lines image. (c) Au M lines image. The three images area acquired simultaneously form the same region. (d) X-ray emission spectra acquired from a point well inside a cleaved area (red line – color online) and on the nearest gold covered area (black line).

5.6 References

- [1] M. Lazzarino et al., "Twin cantilevers with a nanogap for single molecule experimentation," *Microelectronic Engineering*, vol. 83, n°. 4, pagg. 1309-1311, Apr. .
- [2] A. Qazi et al., "Asymmetrical twin cantilevers for single molecule detection," *Applied Physics Letters*, vol. 90, n°. 17, pag. 173118, 2007.
- [3] L. Yang, Y. Lua, M. V. Lee, e M. R. Linford, "Chemomechanical functionalization and patterning of silicon," *Accounts of Chemical Research*, vol. 38, n°. 12, pagg. 933-942, Dic. 2005.
- [4] J. Moreland e J. W. Ekin, "Electron tunneling into superconducting filaments using mechanically adjustable barriers," *Applied Physics Letters*, vol. 47, n°. 2, pag. 175, 1985.

- [5] R. J. Hamers et al., "Cycloaddition chemistry of organic molecules with semiconductor surfaces," *Accounts of Chemical Research*, vol. 33, n° 9, pagg. 617-624, Set. 2000.
- [6] M. D. Ellison e R. J. Hamers, "Adsorption of Phenyl Isothiocyanate on Si(001): A 1,2-Dipolar Surface Addition Reaction," *The Journal of Physical Chemistry B*, vol. 103, n° 30, pagg. 6243-6251, Lug. 1999.
- [7] F. Tao e G. Q. Xu, "Attachment Chemistry of Organic Molecules on Si(111)-7 × 7," *Accounts of Chemical Research*, vol. 37, n° 11, pagg. 882-893, Nov. 2004.
- [8] T. Leftwich e A. Teplyakov, "Chemical manipulation of multifunctional hydrocarbons on silicon surfaces," *Surface Science Reports*, vol. 63, n° 1, pagg. 1-71, 2008.
- [9] X. Lu, X. Wang, Q. Yuan, e Q. Zhang, "Diradical Mechanisms for the Cycloaddition Reactions of 1,3-Butadiene, Benzene, Thiophene, Ethylene, and Acetylene on a Si(111)-7×7 Surface," *Journal of the American Chemical Society*, vol. 125, n° 26, pagg. 7923-7929, Lug. 2003.
- [10] M. Zangrando, M. Zacchigna, M. Finazzi, D. Cocco, R. Rochow, e F. Parmigiani, "Polarized high-brilliance and high-resolution soft x-ray source at ELETTRA: The performance of beamline BACH," *Review of Scientific Instruments*, vol. 75, n° 1, pag. 31, 2004.
- [11] M. Gupta e K. K. Gleason, "Initiated Chemical Vapor Deposition of Poly(1H,1H,2H,2H-perfluorodecyl Acrylate) Thin Films," *Langmuir*, vol. 22, n° 24, pagg. 10047-10052, Nov. 2006.
- [12] R. Winter et al., "Perfluorinated polymer surfaces comprising SF5-terminated long-chain perfluoroacrylate," *Journal of Fluorine Chemistry*, vol. 115, n° 2, pagg. 107-113, 2002.
- [13] R. Klauser, Y. Tai, Y. L. Chan, e T. J. Chuang, "Surface Chemistry of Azomethane Adsorbed on Si(111)-7 × 7 Surface Studied by SR-Photoemission, HREELS, and STM," *The Journal of Physical Chemistry B*, vol. 107, n° 6, pagg. 1387-1394, Feb. 2003.
- [14] E. Magnano et al., "Thermally induced changes in cluster-assembled carbon nanocluster films observed via photoelectron spectroscopy," *Applied Surface Science*, vol. 212, pagg. 879-884, Mag. 2003.

Conclusions

This thesis has presented two novel concepts of MEMS/NEMS devices and their applications in biology. The development of a novel class of mechanical resonators, tapered pillars, as very sensitive mass sensor and a new approach for chemical functionalization of atomically flat cantilever surface are introduced and described in details.

The pillar geometry allows localizing the mass adsorption exactly at the end of the beam in a relative large area. Respect to most of the mechanical resonating devices, the variation of frequency by the mass adsorption is given simply by the harmonic resonator scheme and further models and approximations are not required because the intrinsic high accuracy of localization. The interpretation of the experimental results is more accurate and reliable. In the thesis, all single aspects of this approach were developed. We gave an overview of the design and the fabrication of the devices. We described the experimental set-up used for the characterization (measuring the resonance frequency) of the devices, by means of optical deflection, and gave the detail of the experimental optimization of the chemical and biological procedures. We followed the *dip and dry* approach which provides the possibility to couple the detection in vacuum and the functionalization in liquid environment. The super hydrophobicity of micro patterned surface allowed enhancing the functionalization phase reducing further the aspecific adsorption. In fact, a complete dipping of a device is not required but it is possible to wet only the top of the pillars.

We presented a study about the DNA kinetics of adsorption and hybridization rate. We started this experiment evaluating the hybridization efficiency of SAM of ssDNA but we discovered that the kinetics of adsorption on pillars is much faster than the one reported in previous works for the extended surface. In general, the kinetics of adsorption is influenced by diffusion of molecules near the surface. The main effect is the reduction of local concentration of molecules which causes the slowing down in the adsorption of the surface. Due to the particular geometry of pillars, the effect of diffusion is reduced. While in a flat substrate the number of molecules which can reach the substrate will be proportional to the vertical column above the absorption site, in the case of pillar geometry, also molecules coming from different directions can reach the adsorption site. The overall flux of molecules is increased and the kinetics is faster. One of the most important consequences is that this accelerated adsorption requires less concentration of DNA for preparing

a SAM with a specific density respect to an extended surface. We also observed that at maximum surface density, the hybridization efficiency is around 40 % which is four times higher than the one reported for standard SAM.

Then, we gave an overview of the preliminary results of two novel applications of pillar approach: the development of a protein chip technology based on pillars and the combination of pillar and nanografting, an AFM based nanolithography. These two applications will expand the potential of developing biosensor based on pillar approach. In this direction a technological step is still necessary. It has to be developed a completely electronics detection of the pillar motion for many reasons, for example, to reduce the dimension and the costs of the overall instrumentation. Above all, a large scale parallelization of device can be implemented. The final goal is to realize a device which allows a multi feature, real time and quantitative protein detection.

For the second application of the MEMS technology we gave an overview of the twin cantilever approach and demonstrated the intrinsically aligned chemo-mechanical functionalization of two silicon surfaces separated by a distance tunable with nanometric precision using two different chemical approaches on cantilevers cut in two different silicon crystallographic orientations. We characterized the high selectivity of the process with different spectroscopy techniques: fluorescence, dispersive X-ray spectroscopy (EDAX) and synchrotron radiation photoemission spectroscopy. Moreover we reported an analysis of the cleaved surface which showed that almost of 50% of the surfaces were defect free. We believe that this method constitutes a significant step forward in the fabrication of highly sensitive micro and nanoelectromechanical systems for biological sensing. In fact, as in pillar approach, the special control of the functionalization is a fundamental requirement for developing reliable biosensors.

Acknowledgment

I would like to thank my supervisor Prof. Giacinto Scoles for giving me the chance to know the world of biophysics and for his guidance and encouragement. He taught me not only how to handle the research, but he also helped me to do a step further in my personal growth.

I would like to thank my second supervisor Dr. Marco Lazzarino for giving me the opportunity to be a part of his group, for his support during the course of the PhD and for being always available for help and for giving valuable suggestions.

I would like to acknowledge the SISSA, in particular SBP sector, for supporting me during my PhD period.

I am very grateful to all the people of TASC laboratory. In particular, to my colleagues Damiano, Elisa, Hossein, and Valeria and to the past and present members of Lilit Group, I spent both work and fun time with. A special thanks to Alessandro P. (Pozy), Alessandro C. (Carpenter) and Mauro (Prash). Many thanks go to the TASC technicians who helped me a lot: Stefano B., Stefano V., and Aleš, Federico and Paolino of the mechanical workshop. I am also very thankful to the administrative staff.

I am grateful to Dr. Loredana Casalis for helpful discussions but above all for giving me the opportunity to work in her lab where I found the precious collaboration of other members, Matteo, Fouzia, Barbara, Pietro and Denis, who made possible many results of my thesis with their help.

A special thanks to my parents and my family, who always advised and supported me in every possible way.

My wife, Francesca, deserves a very special acknowledgment. I want to thank her for patience, support, confidence in me and especially for her love.

MM

Appendix A

Elasticity

The classical theory of elasticity describes materials that are deformed by a force and that recover the original shape when the force is removed. Actually, almost all materials possess this property in certain condition, in particular when the applied forces are low. In this case the displacement x due to the force is proportional to the force itself. The relation which describes elastic material is known as Hooke's law.

$$F = -kx$$

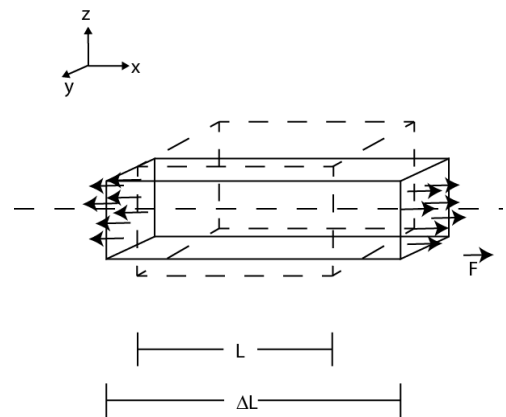
where k is parameter which is called elastic constant.

Suppose we take a rectangular block of material (see fig 1) of length L , width w , and height h and we pull the ends with a force F the length increases by an amount of ΔL . Since ΔL is proportional to L it is more general to consider the ration between ΔL and L . The force, for a given amount of stretch, is proportional to the cross-sectional area A of the block. These considerations allow rewriting the Hooke's law in a form which is independent from the geometry of the block:

$$\frac{F}{S} = E \frac{\Delta L}{L}$$

The parameter E is a property only of the nature of the material and is known as Young's modulus. The force per unit area is called the *stress*, and the stretch per unit length is called the *strain*. Moreover, when a block of material is stretched in one direction it *contracts* at right angles to the stretch. The contraction in width is proportional to the width w and also to $\Delta L/L$. The sideways contraction is in the same proportion for both width and height:

$$\frac{\Delta w}{w} = \frac{\Delta h}{h} = -\sigma \frac{\Delta L}{L}$$



The constant σ is another property of the material called Poisson's ratio. It is number between 0 and 0.5 which is value of perfectly incompressible material.

Combining the two previous equations is possible do define the bulk modulus K in term of E and σ :

$$K = \frac{E}{3(1 - 2\sigma)}$$

The bulk modulus K is the coefficient of proportionality between a uniform hydrostatic pressure and the volume strain. In table 1, the values of the elastic parameters of selected materials are listed.

Material	Young Modulus (GPa)	Poisson's Ratio	Density (g/cc)
Silicon	185	0.28	2.3
Silicon dioxide	70	0.17	2.2
Silicon nitride	250	0.27	3.3
Silicon carbide	450	0.14	3.1

The Bent Beam

If a beam is bent into some curve the material on the inside of the curve is compressed and the material on the outside is stretched. There also a surface that is neither compressed nor stretched, the neutral surface. The material below the neutral surface has a compressional strain which is proportional to the distance y from the neutral surface; and the material above is stretched, also in proportion to its distance from the neutral surface. So the longitudinal stretch ΔL is proportional to the height y . The constant of proportionality is just L over the radius of curvature of the bar.

$$\frac{\Delta L}{L} = \frac{y}{R}$$

In a small strip at y , the stress is proportional to y .

$$\frac{\Delta F}{\Delta A} = E \frac{y}{R}$$

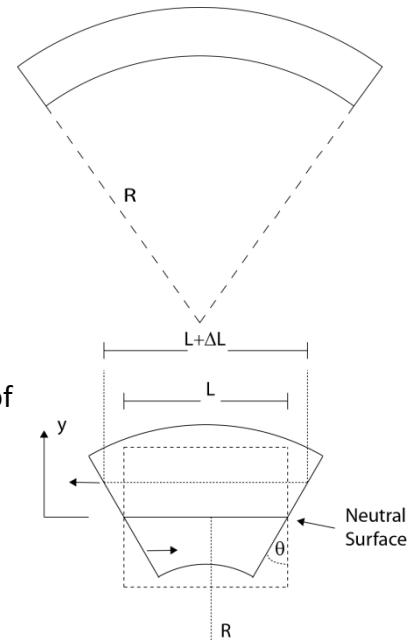
The total bending moment is compute by integration

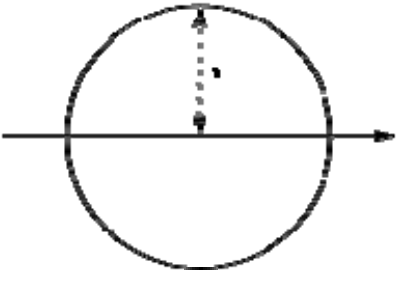
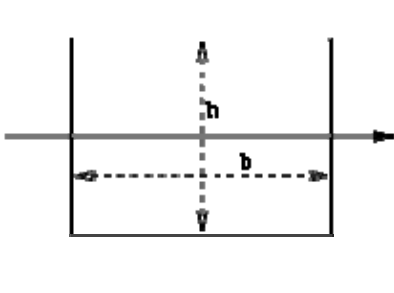
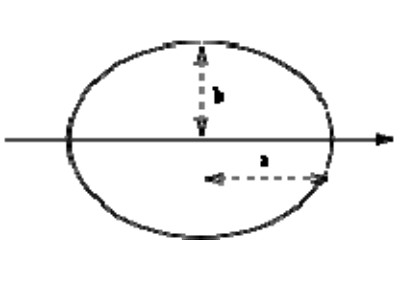
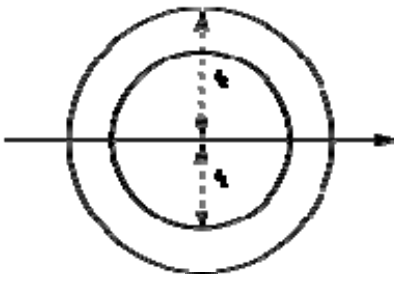
$$M = \int y dF = \frac{E}{R} \int y^2 dA$$

The last integral is called the “area moment of inertia”. It is generally indicated with letter I . In table 2, the relations between I and the geometrical parameters are given for typical cross section.

The total bending moment is given by

$$M = \frac{EI}{R}$$



	$I = \frac{\pi r^3}{4}$		$I = \frac{wh^3}{12}$
	$I = \frac{\pi ab^3}{4}$		$I = \frac{\pi(r_2^4 - r_1^4)}{4}$

The last equation is very useful and allows computing the shape of a cantilever if a force is applied to the free end.

The deflection z of the beam at the distance x from the fixed end is described by the curve $z(x)$. The curvature of $z(x)$ is given by the general formula:

$$\frac{1}{R} = \frac{d^2z/dx^2}{\sqrt{(1 + (dz/dx)^2)^3}}$$

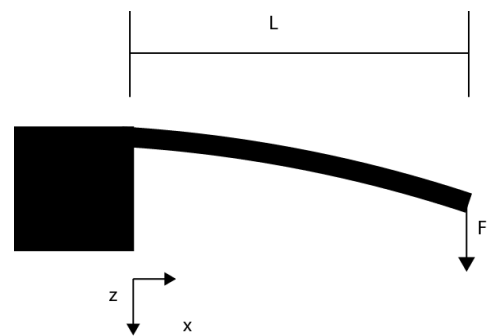
In the limit of small deflection, the term $(dz/dx)^2$ can be neglected and we can get a simpler equation:

$$\frac{1}{R} = \frac{d^2z}{dx^2}$$

The bending moment due to the force at x is $M(x) = F \cdot (L - x)$

Putting together the previous equation we get to the following differential equation.

$$F \cdot (L - x) = \frac{EI}{R} = EI \frac{d^2z}{dx^2}$$



That can be directly integrated with boundary condition $z(0) = 0$ and $dz/dx|_{x=0} = 0$

$$z(x) = \frac{F}{EI} \left(\frac{Lx^2}{2} - \frac{x^3}{6} \right)$$

The displacement at the end is

$$z(L) = \frac{L^3}{3EI} F$$

It is worth to stress that the displacement is linearly proportional to the applied force like in a spring and, by analogy, we can introduce the spring constant of a cantilever

$$k = \frac{3EI}{L^3}$$

In order to describe the dynamical behavior of the cantilever if a periodical force $F(t)$ is applied as first approximation a lumped model can be introduced. The cantilever is approximated with a mass to the end of a spring. All dissipation contributions are included in a pseudo-force which is proportional to the velocity. Putting together all this terms we have the following equation:

$$m\ddot{x} + m\gamma\dot{x} + kx = F(t)$$

that is the well-known equation for a forced oscillator with damping. If we define the natural angular frequency as $\omega_0 = \sqrt{k/m}$ and suppose that the driven force is $F(t) = F_0 \cos(\omega t)$ the solutions are:

$$x(t) = \frac{F}{m} \frac{1}{\sqrt{(\omega_0^2 - \omega^2)^2 + (\gamma\omega)^2}} \cos(\omega t + \theta)$$

$$\tan \theta = -\frac{\gamma\omega}{\omega_0^2 - \omega^2}$$

The amplitude has a maximum when the driving frequency is equal to $\omega_r = \omega_0 \sqrt{\left(1 - \frac{1}{2Q^2}\right)}$ where new parameter, Q factor, is introduced $Q = \omega_0/\gamma$. In order to describe a real systems the mass of the cantilever must be substituted with a reduced mass or an effective mass which is indeed proportional to the actual mass.

Euler–Bernoulli beam theory is more rigorous and generic which provides a means of calculating the load-carrying and deflection characteristics of beams. It covers the case for small deflections of a beam which is subjected to lateral loads only. It is thus a special case of Timoshenko beam theory which accounts for shear deformation and is applicable for thick beams. These analytical models allow calculating the effective mass and the frequencies of higher modes.